UNIVERSITÉ DE GENÈVE
GROUPE DE PHYSIQUE APPLIQUÉE

FACULTÉ DES SCIENCES
Professeur Jean-Pierre Wolf

All-optical methods and devices for real-time aerosol detection

THÈSE

présenté à la Faculté des Sciences de l'Université de Genève
pour obtenir le grade de Docteur ès sciences, mention physique

par

Denis Kiselev

de

Klimovsk (Fédération de Russie)

Thèse $N°$ 4432

Acknowledgements

I would first like to thank my research adviser, *Prof. Jean-Pierre Wolf*, for allowing me to lead this project, for helping me at its every stage and for giving me this unique opportunity of implementing my technical knowledge in research. I am very thankful to *Dr. Luigi Bonacina* who took part in this project from the beginning to the end.

I am really grateful to all Jean-Pierrre's group members, *Jerome Extermann, Jerome Kasparian, Andrey Stepanov, Andrii Rogov, Stefano Henin, Massimo Petrarca, Cecile Joulaud, Thibaud Magouroux, Svetlana Afonina, Michel Moret, Nelson Helaine, Ariana Rondi, Pierre Bejot, Stefan Weber, Yannick Petit, Francois Courvoisier,* for their support during these four years of PhD thesis. They were always by my side for interesting and fruitful discussions and for giving some advice.

Many people from other departments supported me during this work and helped me to succeed my project. *Matthias Kuhn, Claudio Barreiro, Bruno Sanguinetti, Olivier Guinnard, Rafael Houlmann, Clara Osorio, Nicolas Gisin, Hugo Zbinden, Felix Bussiere, Rob Thew, Mikael Afzelius* are just few of them.

I would like to address special thanks to the GAP secretaries, *Isabel, Laurence and Nathalie* for supporting my chaotic way of treating my invoices and helping me in solving administrative problems.

A particular acknowledgment must be done to the people of the mechanical workshop of the Physics Department, *Roland, Andrean, Regis, Luis, Miguel, Megan, Nicolas, David, Joao*. This project would have stayed on the paper without their high quality work.

Finally, I would like to dedicate this work to *my parents* who have been always behind me.

Summary

The airborne particles or atmospheric aerosols are fundamental component of the air we breath. Their concentration, physical, and chemical properties, allergenicity, and simply their presence affect our health and economy. Moreover, the aerosols play a role in the regulation of climate processes. For these reasons, their influence on many aspects of human life and activity represents a huge field of scientific studies. Until now, however, one of the limiting factors in aerosol science is the lack of real-time detectors with a high discrimination power. At the same time, a similar need is shared by meteorological and health institutions, who need such devices to be able to prevent or anticipate the aerosol related diseases like allergies.

In the first part of this PhD work, I investigated some new methods and developed new devices for the real-time and highly specific aerosol particle detection. All these methods are based on the light-matter interactions induced by coherent (lasers) and non-coherent (UV lamps) light sources. The main goal of this work is to demonstrate accurate and reliable single airborne particle identification by light scattering and fluorescence. I will show that the correlation of these two physical processes allows distinguishing nearly identical aerosols like different pollen species. A detailed description of a new robust transportable detector of single airborne particles that I realized will be presented. It will be followed by the calibration tests on individual artificial microparticles and then the first discrimination tests on single pollen grains with linear and non-linear spectrally resolved fluorescence.

The second part of this document will illustrate new developments in the ultrashort laser pulse manipulation. In particularly, it will focus on a new light shaping device and its characterization for the phase and amplitude modulation of laser pulse spectral components. This apparatus is based on the microelectromechanical systems (MEMS), has been developed in collaboration with the Prof. de Rooij's group at EPFL. The experiments in a very broad spectrum of wavelengths will demonstrate the devices capabilities. Based on this technology, new advanced methods of discrimination can be developed in the future and being integrated in real-time aerosol detectors.

This PhD work covers quite different research fields, as a consequence, few words are required to understand my personal contribution to these activities. I personally performed the part dedicated to the aerosol detection including conception, design, simulation, and tests. Concerning MEMS shaper, I performed the development and realized its electronics, participated with other colleagues in the IR and UV experiments, and directly performed the amplitude shaping of high harmonics in the XUV region in collaboration with the Prof. Woerner's group at ETH Zurich.

Résumé

Les microparticules en suspension gazeuse ou les aérosols font partie intégrante de l'air que nous respirons. Leur concentration, propriétés physiques et chimiques, allergénicité ou, simplement leur présence affectent beaucoup la santé publique et l'économie. Un nombre important de groupes de recherche travaille intensivement afin d'évaluer le rôle que jouent les aérosols dans de différents aspects de notre vie. Un des obstacles majeurs pour ces études a été et reste toujours la détection rapide et fiable des espèces similaires de particules présentes dans l'atmosphère.

Au cours de ce travail, je vais mener une étude approfondie des méthodes de détection optique d'aérosols. En me basant sur l'expérience d'autres groupes de recherche, un nouveau type de détecteur a été élaboré. Celui-ci utilisera la lumière diffusée par des microparticules uniques et la fluorescence résolue spectralement et excitée par une lampe à gaz Xénon. Mes expériences auront pour but d'identifier et de discriminer les particules de différents types d'aérosols.

L'appareil qui sera présenté a pour particularité d'être robuste et transportable, ce qui permettra dans le futur de l'utiliser directement sur les sites où la concentration des aérosols doit être mesurée. Ce travail de thèse présentera aussi en détails les aspects techniques du développement mené.

Une étude supplémentaire sera effectuée sur l'interaction de microparticules uniques avec un laser femtoseconde très intense (jusqu'à 10^{12} W/cm^2). Elle aura pour objectif d'évaluer la réponse en fluorescence multi-photons des aérosols pour l'appliquer à la discrimination entre divers échantillons. Cette interaction non-linéaire ouvrira l'accès à d'autres algorithmes dont le développement des aspects techniques sera donné dans la deuxième partie de ce document.

Ces méthodes avancées exploitent la dynamique ultra-rapide des molécules, avec l'échelle du temps de centaines fs jusqu'à quelques ps, et nécessitent des instruments optiques capables de modifier la phase et l'amplitude des composantes spectrales d'impulsions laser dans le domaine de lumière infrarouge (IR), visible (VIS) et proche ultraviolette (UV). Un de ces appareils a été développé au sein de notre groupe en collaboration avec le groupe de Prof. de Rooij de l'EPFL. Il emploie les matrices unidimensionnelles de micro-miroirs basé sur la technologie MEMS (Microelectromechanical systems).

Utilisées dans la géométrie d'un façonneur temporel d'impulsions, ces matrices permettent de modifier la phase et l'amplitude de composantes spectrales. Cette technique est de grande utilité pour les expériences de discrimination de molécules similaires en exploitant des différences subtiles de leur dynamique vibrationnelle. En effet, ces méthodes avancées, impliquant des lasers femtosecondes pourraient

un jour devenir une base solide d'identification des espèces d'aérosols en temps réel.

Malgré les efforts fournis, les expériences utilisant à la fois le détecteur d'aérosols et le façonneur d'impulsions n'ont pas pu être mené, suite à des problèmes techniques de synchronisation des tirs laser avec la détection de microparticules. Par conséquent, le champ d'application des matrices de micro-miroirs a été élargi en façonnant l'amplitude des impulsions ultra-brèves dans le domaine de l'ultraviolet extrême (longueurs d'onde jusqu'à 40 nm). Ce travail a été effectué en collaboration avec le groupe de Prof. H.J. Woerner à l'EPFZ. Cette application a ouvert pour la première fois la possibilité d'agir sur l'amplitude de composantes spectrales d'impulsions attosecondes.

J'ai entiérement effectué le travail sur le détecteur d'aérosols et les expériences avec la lampe Xe et le laser femtoseconde. J'ai aussi mené le développement de l'électronique de pilotage pour les matrices MEMS et j'ai participé avec mes collègues aux premiers essais dans l'IR, VIS et proche UV. J'ai personnellement effectué les expériences de façonnage dans le XUV.

Contents

List of Figures

List of Tables

Introduction

Outdoor and indoor air contains a large variety of particles with different sizes, chemical, and physical properties. These airborne particles (or aerosols) play an important role for health [1], economy [2] and environment [3]. They are also involved in many climate processes on our Planet, which are still not well understood [4, 5].

Pollens and spores have one of the largest impact on human health because some of them are responsible for allergies [6]. According to statistical analysis, 20% of population in Europe is affected by pollen allergies, e.g. over 2.5% of the population in all European countries is sensitive to the ragweed (*Ambrosia*) pollen [7]. In addition, 23.7% of ragweed-sensitive patients across Europe also present asthma symptoms.

Bioterrorism has also became an important safety issue our days [8]. The artificial pathogenic aerosols is now officially included in the weapon arsenals of many countries [9]. Real-time aerosol detection and identification is a rapidly growing research field. In order to efficiently protect populations, aerosol detection devices have to be very fast and very selective to discriminate harmful from harmless particles and minimize false alarm rates.

Detection techniques like polymerase chain reaction (PCR) [10, 11], antibiotic resistance determination [12] or matrices of biochemical microsensors [13] have a very high selectivity but are rather slow or need to treat samples in a liquid solution that limits their applications [10]. On the other hand, optical techniques provide information in real-time but they still lack in specificity. Some elastic scattering based [14, 15] techniques as well as elastic scattering and fluorescence detection approaches [16, 17, 18, 19] have demonstrated the most promising results in the field. The most advanced experiments address individual aerosol particles, whose fluorescence is spectrally analysed.

Optical techniques are also attractive as they can provide information remotely. Light detection and ranging (Lidar) allows mapping aerosols in 3D over several kilometres [20, 21, 22]. So far, Lidar detection of aerosols with biological origins

(or bioaerosols) has been demonstrated either using elastic scattering [23, 24] or UV-LIF (laser induced fluorescence) [25, 26]. However, the distinction between bio- and nonbio-aerosols was either impossible (elastic scattering only) or unsatisfactory for LIF-Lidars (interference with pollens and organic particles like traffic-related soot or PAHs).

The first part of this PhD work will present concepts, design, and first experiments of a newly developed real-time single particle detector. This part was entirely performed by the author of this PhD work. The device uses the classical methods of the elastic scattering and spectrally resolved fluorescence detection to identify the aerosols. Despite the fact that this measurement technique was already studied [27], a large technological effort was undertaken to increase the selectivity and reduce the physical size and the cost of the device. It will be illustrated that the developed system enables the detection and discrimination among some biological particles. Still, the selectivity of the method is not sufficient to identify a large variety of nearly identical biological and non-biological particles.

To overcome these limitations, new methods using the fluorescence excited by ultrashort laser pulses have appeared and an increase in optical selectivity has been demonstrated by addressing specific molecular dynamical features. Recent experiments using coherent control [28] and multiphoton ultrafast spectroscopy have shown the ability to discriminate between molecular species that have similar one-photon absorption and emission spectra [29, 30].

Multi-Photon Excited Fluorescence (MPEF) [31, 32] and pulse shaping techniques will probably allow achieving even higher selectivity in the future by the selective enhancement of the fluorescence of one molecule versus another. One of such MPEF experiments on the single aerosol particles, performed by the author, will be demonstrated. Some more advanced techniques like Optimal Dynamic Discrimination (ODD) [33, 34, 35] of similar molecular agents provide the basis for generating optimal signals for detection in the future.

In the aerosol detection context, these techniques can permit one day to elaborate an open-loop method for rapid particle identification. However, there is still a long way to go, and some additional developments are necessary to manipulate spectral amplitude and phase of ultrafast laser pulses, in particular in the deep UV range, the most interesting when dealing with biomolecules. The temporal pulse shaping techniques [36] employ dedicated optical devices, called pulse shapers. A development and the first experiments of such a device based on micro-mechanical electronic systems (MEMS) will be presented in the second part of this PhD work [37, 38, 39]. The author contributed to these experiments and elaborated some technical aspects, including the electronics.

Because of the difficult synchronization with amplified femtosecond laser system (described in Sect. 3.3), the coupling between the MEMS pulse shaper and the aerosol detection device could not be achieved within my PhD term, but it remains one of the highest priority of the Biophotonics group.

On the other hand, the MEMS device could be adapted in a different research context of high scientific challenge. In the last section of the manuscript, in fact, I will describe an experiment I personally performed at ETH Zurich showing extreme ultra violet (XUV) pulse shaping for the first time. This study opens new ways of preparing and manipulating the ultimate attosecond (10^{-17} s) laser pulses with wavelengths as short as 40 nm. Based on this study, many experiments like XUV shaping for probing electron dynamics will become soon accessible.

Part I

Aerosol detection

Chapter 1

Aerosol detector: Concept and design

Until now there is no universal method for real-time monitoring and identification of aerosols. Existing approaches are either fast and with low discrimination power (for example optical counters) or specific but time-consuming (biochemical analysis). This research work participates to the effort of developing new methods featuring the positive characteristics of both approaches. The idea was developing a device ready for in-field experiments and at the same time ready for coupling with other techniques or detection methods. Moreover, along this work, we also considered prototype oriented criteria, like the technical complexity required for its realization and the final cost.
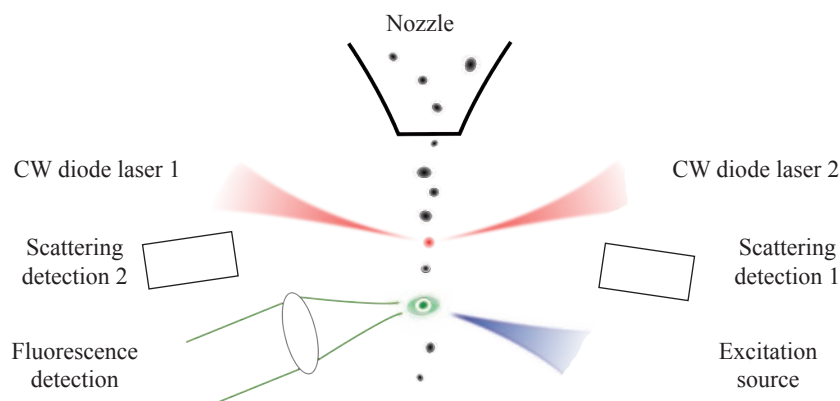
Figure 1.1: Principle of the experiment.

After the detailed study of existing optical detectors and identification methods of aerosols [40, 41, 42, 43, 44, 45, 46, 47], the approach of the group of prof.

Richard K. Chang at Yale University was chosen as starting point of the development. The basic scheme is shown in Figure 1.1. The main idea is to generate a thin flow of air containing aerosols with concentration low enough to have statistically only one particle at a time in the measurement volume. To do this, it is important to design and construct an appropriate injection nozzle. The presence of an aerosol at the outlet of the nozzle is detected by simultaneous light scattering of two intersected continuous wavelength (CW) lasers of different wavelength. The same scattered light is also used to evaluate particle size. When a coincidence of scattering signals is detected, an excitation light source (laser or flash lamp) fires on the particle. The fluorescence spectrum emitted upon excitation by the particle is a characteristic signature of the aerosol molecular composition. Once the spectrum is acquired and the size is measured, one can use these informations and compare them to libraries [27] to identify the group at which this aerosol belongs.

The main stages of the experiment are the following:

- aerosol flow generation (injection nozzle);

- light scattering (CW lasers and scattering detection);

- fluorescence (excitation source and fluorescence detection).

However, linear fluorescence is generally not specific enough as it results from a superposition of many spectra from different molecules [48]. Most of these molecules are present in all living organisms and often in similar proportions. As a consequence, size and fluorescence might not be sufficient to fully identify the particle, but they provide already more information in real-time than a simple optical counter or sizer. Another advantage of our approach, is that all measurements are done on the fly and within a single shot of the excitation source. This permits to integrate the detector to some other experiments, like LIBS [49, 50], or to elaborate more advanced techniques on the same basis.

The proposed method suffers, however, from two main drawbacks. The first, technological, related to the need of a UV laser to excite the fluorescence (higher cost as compared to optical counters and sizers). The second, more fundamental, related to its yet insufficient discrimination power.

Concerning the first point, some alternative approaches were proposed [51, 43] employing light emitting devices (LED) as a UV source. Nowadays these studies have not demonstrated that LEDs can completely replace UV lasers. Moreover, LEDs are still not available at wavelengths below $355\,\mathrm{nm}$ with sufficient pulse energy. Some promising results were also obtained with dual-laser wavelength excitation [31, 46, 44]. Although improving specificity, these methods remain rather complicated and expensive.

To address these open issues, two different ways were explored during this PhD work. The first was to find an alternative to the expensive UV excitation laser. This would lead to a cost-effective detector prototype that would be interesting for the aerosol detection industry. The second way was to explore the possibility of using a femtosecond laser with very high peak intensity to induce multi-photon excited (or non-linear) fluorescence (MPEF). This approach will benefit of simultaneous addressing of two- and three-photon absorption bands, in order to increase the specificity of the detection. Further gain in discrimination can be obtained via non-linear and coherent spectroscopy. Our technical developments towards this goal will be described in Section 4.3.

In the following, we provide an in-depth description of the different components of our device.

1.1 Injection nozzle

1.1.1 Types of nozzles

The injection nozzle is one of the principal parts of the aerosol detector. It is intended to create a thin laminar flow of air containing particles. Depending on the final application and the requested flow thickness, different nozzle concepts could be used. There are four mainly used geometries in aerosol science, inspired by aerospace engine technology (Fig. 1.2):

    a) cone geometry, single inlet;

    b) bell geometry, single inlet;

    c) spike geometry, single inlet;

    d) sheath nozzle, two inlets.

The conical nozzle is the easiest to fabricate but it has poor outlet flow quality. In the bell nozzle, the internal surface has an approximately parabolic shape. It is more difficult to produce but has higher outlet flow quality. The spike geometry has the thinnest outlet flow but the manufacturing process is usually very complicated and this type of nozzle is very expensive. The sheath nozzle is a combination of two bell geometries. It produces a thin and long laminar flow, it has better quality than simple bell nozzle, and it is still less expensive than spike geometry [52].

1.1.2 Selected geometry: sheath nozzle

In our development, the design of nozzle was inspired by the geometry proposed by Prof.R.K. Chang and his colleagues [53]. This design is a sheath nozzle manufactured in two parts by electro-erosion. To avoid manufacturing difficulties, the
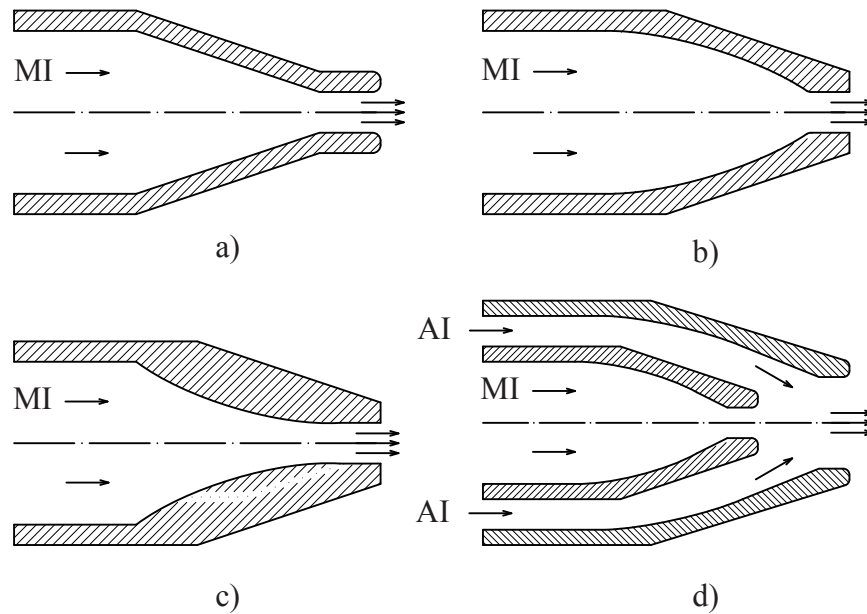
Figure 1.2: Basic nozzle geometries : a) conical; b) bell-shape; c) spike; d) sheath flow. MI - main inlet; AI - auxiliary inlet.

design was split in several mechanical components, each of them manufactured in the mechanical workshop of University of Geneva by standard mechanical processes. Different materials and surface treatments were tested:

a) polished aluminium;

b) polished brass;

c) brass coated with thin nickel layer.

The tests, which will be described in Section 2.1, revealed that the best combination was a nickeled brass nozzle because it is easy to machine like aluminium, but less fragile, and has a very high surface quality (peak-to-valley surface roughness R_z less than 0.1 μm). Individual parts were machined with a specially designed tool (reproducing internal shape) and assembled with help of liquid nitrogen cooling. The final assembly has the same geometry of Prof. Chang's version but is much less expensive in production (Fig. 1.3).
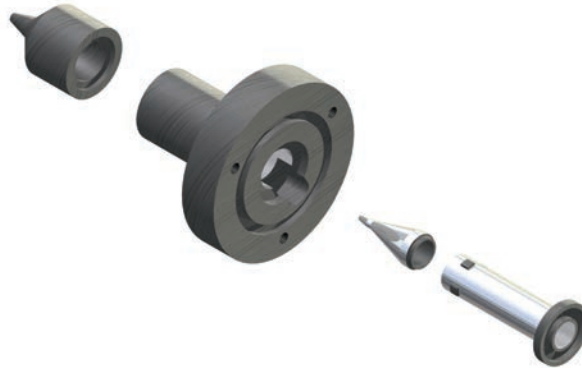
Figure 1.3: Nozzle 3D CAD model.

1.2   Geometry of the measurement chamber

1.2.1   Definition

The measurement chamber is a hermetic volume in which all measurements on
a single aerosol particle are done. It has ports for air flow and nozzle connections,
and also several optical windows for scattering and fluorescence excitation and
detection. During this work, the geometry has evolved from in-plane to 3D element
disposition, in particular to avoid parasitic scattering on the detectors. The optimal
optical disposition retrieved during the testing phase is described below.

1.2.2   Main elements

The measurement chamber (Fig. 1.4) comprises of the following elements:

- nozzle port with alignment mechanism;

- outlet port for connecting a pump;

- four optical windows (two pairs of opposed windows) for two crossed CW
  lasers;

- one optical window for fluorescence detection;

- two optical windows (one pair of opposed windows) for the excitation laser;

- one optional optical window to inspect the inside volume.

1.2.3   Nozzle port

To have the possibility to align the nozzle and manipulate the aerosol flux po-
sition, it was necessary to develop a custom hermetic mechanism built around a
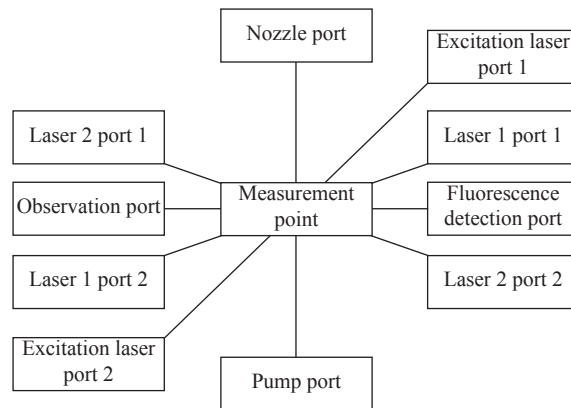
Figure 1.4: Principal scheme of the measurement chamber.

flexible vacuum bellow. After having tested different types, a bellow 170SFA050-060 from Trinos Vacuum was chosen. Two custom made flanges were welded on both ends of the hose. The hermetic junction were made with rubber O-rings.

The whole mechanism is driven by three adjustment screws. Each screw rotates the moving block around the line passing through the two other screws. This mechanism, shown on Figure 1.5, is certainly not the most intuitive to use, but it has the advantage to be simple, efficient and rugged.
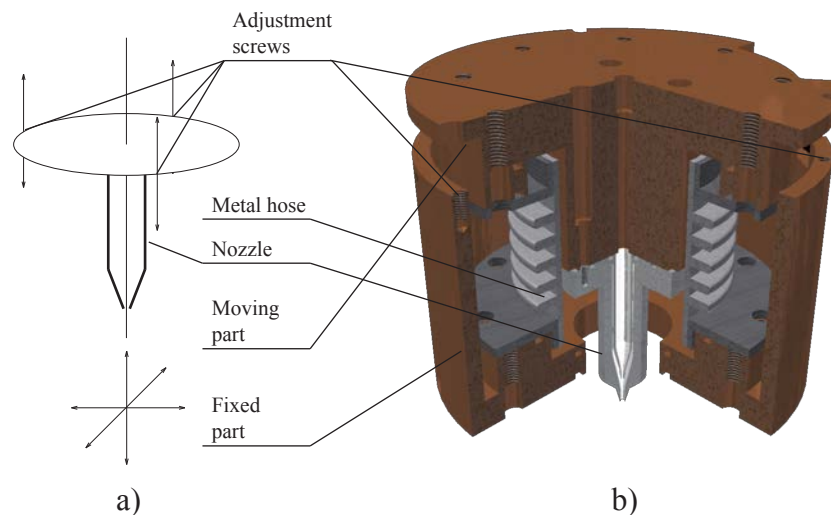
Figure 1.5: Nozzle alignment mechanism: a) principal scheme; b) 3D CAD model.

1.2.4 CW lasers

Two CW lasers of different wavelengths are used to induce optical scattering by individual aerosol particles. Both lasers are intersected on the aerosol flow close to the nozzle outlet. To reduce the detection volume and, at the same time, cover the aerosol flow in the horizontal plane, the spot of each laser has an elliptical shape.

The CW lasers' wavelengths were chosen as spectrally separated as possible in order to provide an additional size information from the Mie scattering pattern 6. The wavelengths should also be in the sensitivity region of the light detectors (in this case photomultipliers) and not overlap with the spectral region of interest (fluorescence response of aerosols). According to these criteria, two commercial diode laser modules were chosen at 658 nm and 780 nm (Laser Comp.). The characteristics of these lasers are given in Table 1.1.

Table 1.1: CW lasers' characteristics

Model	Wavelength	Output power	Output beam
FP-66/20AAF-SD5	658 nm	20 mW	circular collimated
FP-78/20AAF-SD5	780 nm	20 mW	circular collimated

To better localize an aerosol particle with intersected lasers, the angle between these lasers should be close or equal to $90°$ as it reduces geometrically the detection zone.

1.2.5 Optical chamber configuration

The measurement chamber was organized to provide easy access and adjustment mechanisms for all components, and to allow integrating new components for further experiments. The scheme of the measurement chamber is shown on Figure 1.6.

The elements are positioned as following:

- two CW lasers are placed in the horizontal plane $1 - 2$ mm lower than the nozzle outlet;

- the angle between the two lasers is about $100°$;

- both laser beams are blocked by beam dumps inside the chamber;

- each detector (detector 1, 2) is placed in front of the corresponding laser and tilted in the vertical plane by around $20°$. Its field of view is therefore
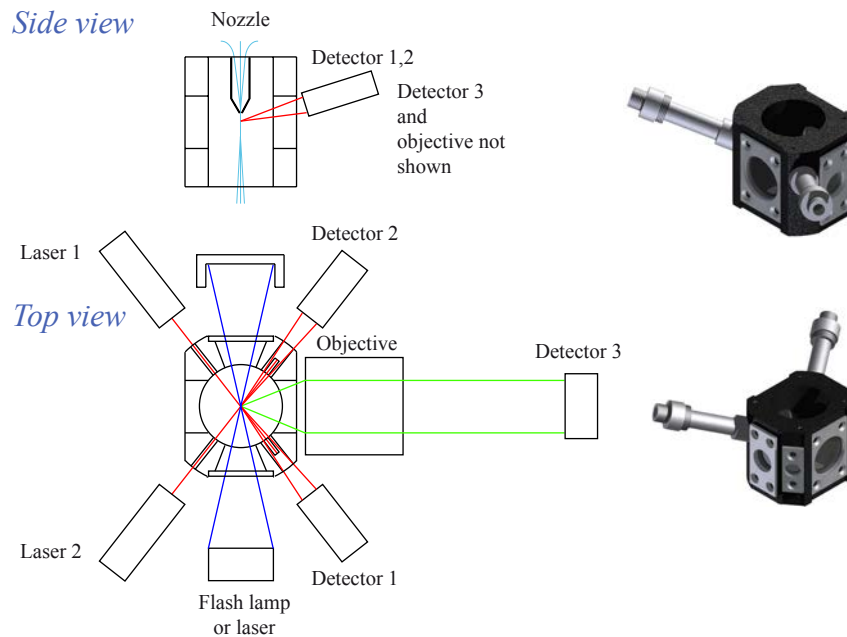
Figure 1.6: Measurement chamber.

directed on the intersection of the CW lasers but tilted out from the laser axis;

- the light source for fluorescence excitation is focused on the CW laser intersection and injected in the horizontal plane;

- fluorescence collection is done through the dedicated window.

1.3 Scattering detection

Light scattered from an individual particle is used to detect the presence of the particle and to determine its size. It is based on the well known Mie theory that gives a general solution for the whole range of aerosol sizes (see Annexe 6). In this work, particular interest was focused on large spherical particles (typical diameter $5 - 50$ µm). The two CW lasers are employed to illuminate the aerosols. The scattered light is captured by two independent detectors, each one having a narrow band filter centred at the wavelength of the corresponding laser.

Each CW laser is focused by a couple of spherical-cylindrical lens on the stream of aerosols. The geometry of the measurement is shown in Figure 1.7. The detector is placed at $19°$ from the beam axis. This angle was selected for achieving the best signal to noise ratio, i.e. the ratio between the light intensity scattered from an aerosol and the background light scattered from the chamber. The noise mostly

comes from the optical window of the measurement chamber, so being closer to the beam axis means that a larger undesirable amount of light will reach the detector. At the same time, the scattering efficiency decreases as the angle between detector axis and the laser beam increases.
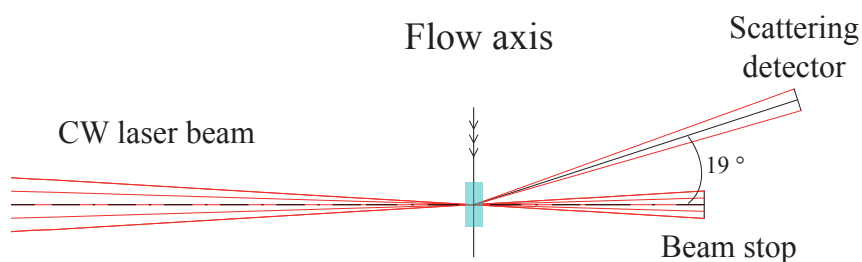
Figure 1.7: Detection geometry for one scattering wavelength.

The detector that was chosen for light collection was a photomultiplier H6780-20 from Hamamatsu Photonics. The characteristics of this module are given in Table 1.2.

Table 1.2: H6780-20 characteristics

Parameter	Value
Spectral response	$300 - 900$ nm
Gain	$10^2 - 2 \cdot 10^6$
Output type	current (max. 100 µA)
Cathode radiant sensitivity	80 mA/W
Detector effective area	$\varnothing 8$ mm
Response time	0.78 ns, load 50 Ω

This detector provides high sensitivity, large dynamic range, and fast response that makes it ideal for scattering light measurements with suitable electronics. It is able to capture the scattering light from aerosols with transition time through the beam as short as 1 µs. Different gain settings make possible to detect particles from 0.5 µm to 50 µm.

1.4 Excitation sources

In the following we described the two approaches followed during this work, the former based on flash lamp excitation, the latter on a femtosecond laser. The common experimental scheme is presented in Figure 1.8.
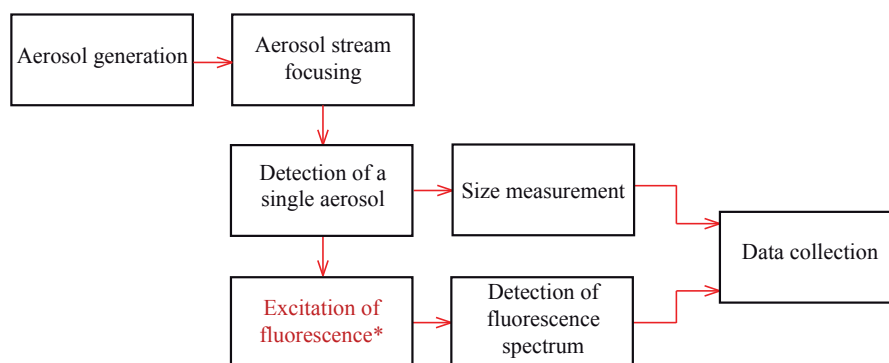
Figure 1.8: Experiment sequence. * - Xe flash lamp or femtosecond laser.

1.4.1 Flash lamp

The following section describes all the aspects connected to the ultraviolet lamp for exciting aerosol fluorescence. This application requires a few microjoules in the UV range ($200 - 300$ nm) and does not need to be continuous emission [45]. Our estimate is based on the previous works from Chang's group who studied the fluorescence of a large variety of microscopic aerosols with a UV Nd:YAG laser. Such a laser provides $10 - 50$ µJ at 266 nm and has narrow bandwidth that makes it ideal for the spectroscopic studies of single aerosol particles. However, the cost of YAG lasers remains high with respect to Xenon flash lamps. Clearly, cost-effectiveness is not the limiting issue for lab-based experiments, but it becomes such for development of a competitive commercial product. Other advantage of flash lamps over UV lasers is their large emission band ($180 - 2000$ nm). This allows to address a larger absorption band, and to intensify and to diversify fluorescence response because higher number of types of fluorescent species will interact with incoming photons.

Flash lamps are intense sources of incoherent light produced by electrical discharge in a noble gas. Most often they are simply made of a hermetic tube with gas and an electrode at both ends. A high voltage pulse between the electrodes generates an electric arc. As current density inside the arc is extremely high (thousands of A/cm^2), the ionized electrons acquire a high amount of kinetic energy. The recombination of these electrons produces a high amount of spectral line characteristic for the chosen noble gas. The continuous background spectrum is due to Blackbody radiation. This PhD work will be mainly dedicated to spectroscopic study of biological particles, in particularly, pollens, which have an efficient absorption in the $200 - 300$ nm wavelength range [54].

Another parameter to take into account is the peak power of the flash $P = \frac{E}{\tau}$ defined by ratio of the energy in one flash E and the flash duration τ. The value of peak power will becomes important for an experiment where the sample cannot be irradiated for a long period. In the case of aerosol detection, a particle irradiated on the fly crosses the spot of the lamp, absorbs UV photons and emits fluorescence during its passage through the spot. To be able to collect the fluorescence coming from the particle, this emission should be concentrated in a defined microscopic region (defined by the objective field of view), and not spread by the particle trajectory. Thus, an intense and short flash pulse should be preferred.

The last parameter to consider is the arc size. It becomes especially important because the sample size is small and most of the flash lamp radiation should be focused on it. Indeed, if the flash arc is long, it becomes difficult to collect its light and focus it onto the sample. Most often a short focal lens is used to obtain a small spot of the lamp. The degradation of the lamp spot due to the arc size can be of course compensated by a higher flash power, so even if the sample has a small size (microscopic particle for example), the light intensity will be sufficient to excite a detectable fluorescence response. Unfortunately, for the on the fly aerosol spectroscopy it means that the probability of irradiating more than one particle increases with the lamp spot size. As a consequence, a compromise should be found between the peak power and the spot size.

Two flash lamps were selected for this work : PAX-1002-2 and FX-4401 from PerkinElmer Optoelectronics. The parameters are given in Tables 1.3 and 1.4 respectively.

Table 1.3: Xe flash lamp: PAX-1002-2 characteristics

Parameter	Value
Max. average input power	10 W
Pulse duration at max. power	1.5 µs at FWHM
Repetition rate at max. trigger voltage	133 Hz
Arc length	1.5 mm
Spectral range	$190 - 2000 +$ nm

Initially, a lamp PAX-10 series was chosen for the experiments. It has some advantages compared to other commercially available Xenon lamps : the flash arc is precisely aligned (± 0.1 mm) respective to the fixing screw positions. As a consequence, it can be even coupled into a optical fibre. It also has a small spot size when focused thank to the short arc length. Together with its high power (10 watt) and compact size, it makes this model a very attractive choice.

Table 1.4: Xe flash lamp: FX-4401 characteristics

Parameter	Value
Max. average input power	60 W
Pulse duration at max. power	1 µs at FWHM
Repetition rate at max. trigger voltage	240 Hz
Arc length	1.5 mm
Spectral range	$190 - 2000 +$ nm

When one works with a flash lamp, he faces two main problems: lamp light collection and spectral filtering. A proper collection is needed to bring as much light as possible on the sample. Spectral filtering is even more important for spectroscopy experiments because the excitation spectrum should not overlap the fluorescence spectrum to maintain a reasonable signal-to-noise ratio.

In the case of PAX-10 lamp, three filtering methods were evaluated using either:

- spectral filters;

- a transmission diffraction grating and conjugated slit;

- a combination of both methods together.

Numerical simulation and ray tracing were made to examine the collection efficiency of each approach. Only standard commercial optical components were used in these simulations. The result is shown in Figure 1.9. The ray tracing is done at 266 nm wavelength.

Each of the schemes presented can be split in three stages: light collection, filter based on a diffraction grating and spectral filter set. In general, parabolic or elliptical reflectors have the largest collection efficiency ($E_{ff} = \frac{\Theta_{col}}{\Theta_{tot}}$). Very often a parabolic reflector is built into the lamp design by the manufacturers to collect back light. The main problem of parabolic reflectors is that the arc length is finite, so the output beam is not perfectly collimated. This will decrease the efficiency of the filtering stages, especially of those based on diffraction grating. So the solution in this case is to use an elliptical reflector together with a short second focus length. To adapt the beam to the design, a defocusing lens was conjugated with the second focus of the reflector. Built on standard optical components, this scheme gives 50% of collection efficiency. Among other collection methods, aspherical lens and off-axis mirror have the highest result (25%), while short focal length spherical lens has 20 % of collection efficiency only.
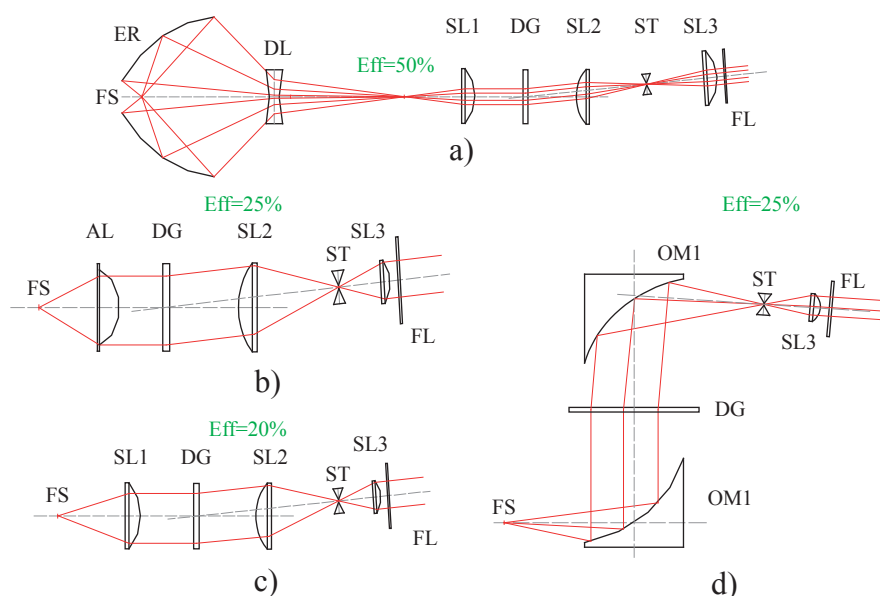
Figure 1.9: Different techniques of the flash lamp collection and
filtering with a diffraction grating: a) elliptical reflec-
tor scheme; b) aspherical lens scheme; c) spherical lens
scheme; d) off-axis parabolic mirrors scheme. Compo-
nents: FS - flash spot; EL - elliptical reflector; DL - di-
verging lens; SL1, SL2, SL3 - spherical lenses; DG -
diffraction grating; ST - slit; FL - filter set; AL - as-
pherical lens; OM1, OM2 - off-axis mirrors. Ray tracing
performed with Code V software

As described before, the Xe flash lamp FX-4401 has about six times higher input
electric power than PAX-10. It has also much higher pulse energy with the same
arc size. The disadvantages of this lamp in comparison to the PAX-10 are a more
complicated mechanical design, need of high power supply (more than 100 W),
and need of passive heat dissipation of the flash head.

By changing the flash source, the output power increased significantly, and the
diffraction grating filtering stage was no longer usable as the damage threshold of
the transmission grating was exceeded. The use of spectral filters directly on the
lamp output was neither possible for the same raison. To reduce the flash pulse
energy without loss in the spectral band of interest, we employed coated dielec-
tric mirrors initially designed for 266 nm (Nd:YAG laser). An optimal solution
appeared to be the mirror model Y4-1025-45 from CVI Melles Griot. This mirror
features a high reflection for $240 - 290$ nm unpolarized light at $45°$ incidence.
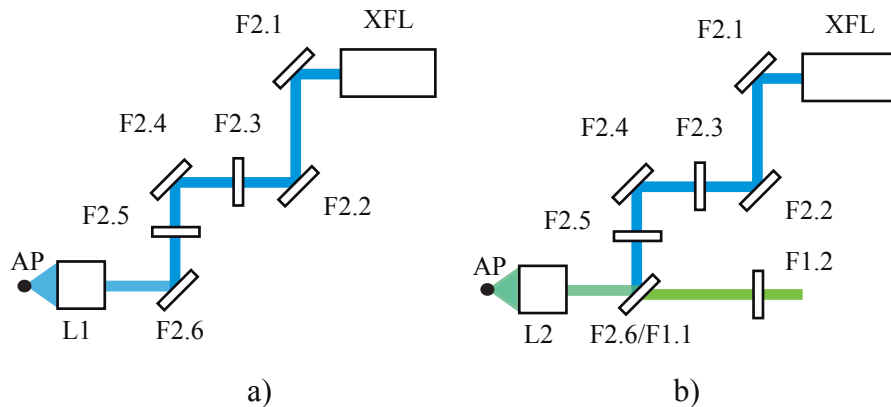
Figure 1.10: FX-4401 lamp filter schemes: a) separated excitation and detection; b) conjugated excitation and detection; L1 - focusing lens; F2.1, F2.2, F2.4, F2.6 - narrow band mirrors Y4-1025-45; F2.3, F2.5 - filters FF01-300/SP-25; L2 - focusing lens or objective; F2.6/F1.1 - dichroic mirror FF310-Di01-25x36, F1.2 - detection filter set, AP - aerosol particle

Figure 1.10 shows two different schemes of fluorescence excitation on an aerosol particle. The scheme in a) represents a separated detection and excitation light paths, which potentially will have the signal-to-noise ratio required for spectroscopic studies. The scheme in b) benefits of the fact that the same focusing lens or objective (L2) can be used to send UV light on samples and collect fluorescent response. It permits to have one more available window of the measurement chamber compared to a), which might be useful for further couplings with other detection techniques like LIBS [49, 50].

1.4.2   Femtosecond laser for multi-photon experiments

The experiment with a femtosecond laser (Annexe 8) aims at evaluating the discrimination power of multi-photon excited fluorescence (MPEF) for single aerosol detection. Given the non-linear dependence of the process under study with respect to excitation intensity, this approach can only work with short (fs) lasers. For a comparison, the relatively low excitation cross sections of endogenous fluorophores for two- or three-photon absorption can be found in Refs. [55, 56]. They range from $\sigma_2 \sim 10^{-50}$ cm^{4}s and $\sigma_3 \sim 10^{-80}$ cm^{6}s^2, and are at least 35 orders of magnitudes less probable than the corresponding one-photon transitions.

Among different types of femtosecond lasers (oscillators, cavity-dumped systems, amplified systems), one that corresponds well to the defined purpose is the amplified laser chain. The shortcoming of a relatively low repetition rate (1 kHz) is largely compensated by its high peak power (GW).

It is also important that sample absorption bands match the 2nd and 3rd harmonic wavelengths of the laser fundamental frequency to obtain efficient MPEF response. In general, femtosecond laser central wavelength depends on the active medium material and on the cavity adjustment. The most common is a Titanium-doped sapphire crystal (Ti:Sa). Its fluorescence emission is centred at 800 nm. Three-photon excitation with such laser corresponds to a 266 nm one-photon (linear) fluorescence excitation. This wavelength is commonly used for aerosol spectroscopy [45, 57] and justifies well with choice of Ti:Sa based system.

Two-photon excitation corresponds to a 400 nm fluorescence excitation. This wavelength is also interesting, as it falls into the absorption band of flavins [58] contained in living cells. Their contribution to the fluorescence response of bioaerosol particles might vary if excited with only 266 nm or 266 nm and 400 nm together. It was indeed already demonstrated recently that a new degree of discrimination is added when a same aerosol is excited once with 266 nm and once with 354 nm [44].

To be able to use such amplified system delivering pulses on-demand, few major obstacles must be overtaken. First, the pump laser of the regen cavity of the amplifier is a high power frequency doubled Nd:YAG or Nd:YLF laser, which generally can not run in on-demand trigger mode because of intra-cavity thermal stability. In our work, it was an Evolution-30 from Coherent Corp. This laser delivers 30 W of average power and can run at $50 - 10000$ Hz repetition rate. When using the external triggering option, the user must provide a stable clock signal in this range of frequencies to avoid activating the internal protection.

A problem related to the not uniform synchronization needed for our experiment, is the thermal stability of the Ti:Sapphire amplifier cavity. Indeed, chirped pulse amplifiers involve important amounts of power, and to avoid any heat related issue, they are optimized for certain frequency ranges. In the on-demand trigger mode, the amplifier cavity does not work efficiently because pumping is asynchronous. As a consequence, the temperature stability of in-cavity components might be compromised. Generally, laser manufacturers propose only on-demand activation of the second Pockels cell (PC2) because it ensures constant cavity pumping, but the laser cannot fire pulses arbitrarily, and no synchronization on external random events is achievable.

A pragmatic solution for a proof-of-principal test was found in collaboration with Coherent Corp. It consists in maintaining a fix mean repetition rate, but each time that a particle is detected the repetition rate is reset, so the laser fires exactly on the aerosol particle. However, caution should be taken that a minimum delay is respected between the last pulse and the reset event. In the case of Evolution-30, this time was fixed to 500 µs. Figure 1.11a illustrates how the system works in
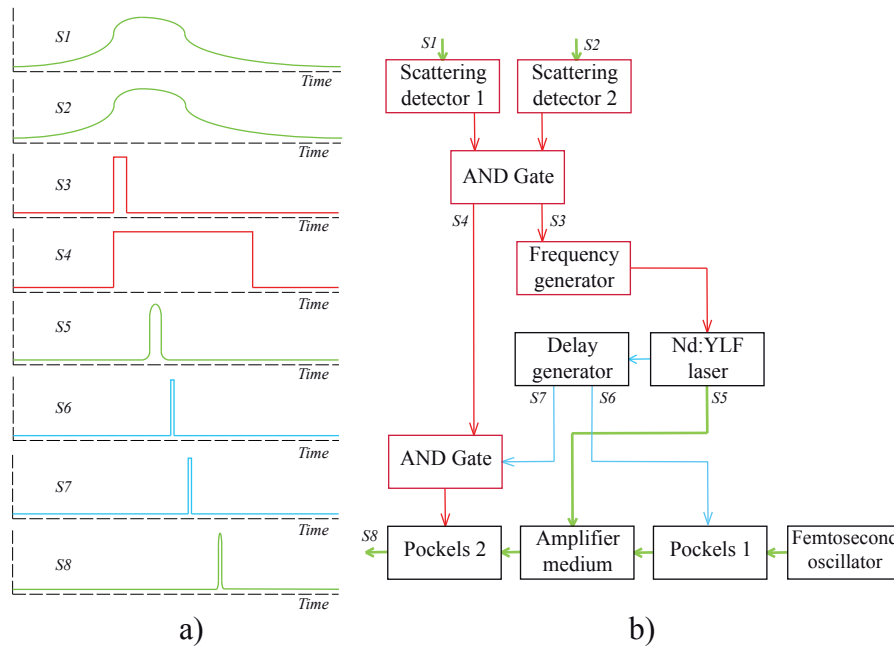
Figure 1.11: a) Timing diagram. Optical signals: S1, S2 - scattering light, S5 - pump laser, S8 - femtosecond laser (in green); detector signals: S3 - trigger signal/coincidence detected, S4 - gate for the Pockels 2 (in red); laser system signals: S6, S7 - Pockels 1,2 triggers. b) Structure scheme

triggered mode. Figure 1.11b shows the structure and additional components to achieve on-demand shooting.

When the coincidence (AND gate) of two scattering signals (S1, S2) is detected, the frequency generator enters into the reset condition. The generator then synchronizes the pump laser and both Pockels cells. An additional AND gate connected to the Pockels cell 2 blocks all laser shots that are not related to a detection event.

1.5 Spectrometer design

1.5.1 Introduction

The spectrometer block is the device stage defined for detecting spectrally resolved fluorescence of single aerosol particles. From previous works, two main possibilities arise to achieve this goal [45, 59]: one is to use an intensified CCD camera and the second is to use a photomultiplier module array. The first method has the advantage of very high spectral resolution (less than $1 \ \mathrm{nm/pixel}$), but the acquisition rate is relatively slow (in general less than $50 \ \mathrm{Hz}$). Moreover, inten-

sified CCD cameras are expensive, which is also contradictory to the initial aims of the project. The second method employs a 32-channel photomultiplier leading to lower resolution but the data acquisition can be done in parallel from all pixels, and the frame rate is only limited by the ratio acquisition accuracy / sampling rate. Given all these factors, it was decided to develop a customary designed spectrometer based on a multichannel (32) photomultiplier. More than this, existing reading electronics for such photomultipliers do not respond to all criteria of the project (being compact, easy coupling with the rest of control electronics). So the acquisition module needed to be entirely developed as well.

1.5.2 Light collection

The starting point of the spectrometer design was the selection of a light collection element. Previous experiments [45, 60, 61] used reflective objectives, parabolic and elliptical mirrors, and spherical and aspherical lenses for the fluorescence collection. Among all these optical components, reflectors and mirrors have the largest solid angle of collection. At the same time, using reflectors and mirrors can be restricted by the available space around the measurement volume. In the case of this work, the lay-out of components (CW lasers, scattering detectors) was such that it was impossible to place a reflector or a mirror in the chamber. Lenses suffer in general of chromatic aberrations, which can be in principle corrected in achromats (doublets of lenses) but then the commercially available focal lengths are limited. Moreover, it was already mentioned that the excitation light can be also injected through the collecting element, so the spectral transmission of the collector must cover both excitation and fluorescence spectrum. Same difficulty concerns conventional objectives, without taking into account that UV objectives are much expensive than other options listed here. From this point of view choosing a reflective objective was well justified.

1.5.3 Basic scheme

Designing a spectrometer means in general selecting an appropriate spectrally dispersive element and additional optics to achieve the needed resolution and fill well the detector surface.

Figure 1.12 shows a basic scheme of our collection and spectrum measurement system. As it can be seen from the design, a plane diffraction grating was chosen. The number of grooves is selected to match best the bandwidth of interest. Previous works [62] demonstrated that if exciting at 266 nm or close, the best detection range is between 300 nm and 600 nm. All detected spectra would fit into this range of wavelengths.

The focal length (75 mm) of the imaging lens (FL) was chosen to keep the whole block compact. The selection of grating is imposed by active size of the multichan-
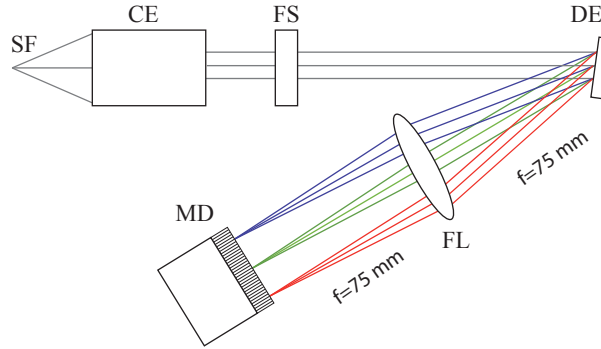
Figure 1.12: Basic scheme. Fluorescence collection and spectrometer : SF - source of fluorescence; CE - collecting element; FS - filter set; DE - diffracting element; FL - focusing lens; MD - multichannel detector.

nel detector (MD). The detector chosen for the experiment was the H7260-03 from Hamamatsu Corp, its main characteristics are shown in Table 1.5.

Table 1.5: H7260-03 characteristics

Parameter	Value
Spectral response	$185 - 650$ nm
Gain	$10^2 - 2 \cdot 10^6$
Output type	current (max. 100 μA)
Cathode radiant sensitivity	72 mA/W
Number of pixels	32
Pixel size	L0.8 mm x H7 mm
Pixel pitch	1 mm
Response time	0.6 ns, load 50 Ω

The whole effective length of the detector is around 32 mm and it should be filled out by the spectral range of interest ($300 - 600$ nm). From a simple geometrical calculation, it follows that the size of the image in the focal plane of the FL is:

$$H = F \cdot (tan(-\beta_{min} + \beta_{cen}) + tan(\beta_{max} - \beta_{cen})) \qquad (1.1)$$

where H - image size, [mm];
         F - focal distance, [mm];
         β_{min} - output angle for the lowest wavelength, [°];
         β_{cen} - output angle for the central wavelength, [°];
         β_{max} - output angle for the largest wavelength, [°].

If one evaluates this expression for typical groove densities (diffraction order $n = 1$, incidence angle $\alpha = 15°$) with the grating formula $sin(\alpha) + sin(\beta) = nG\lambda$ where G is the groove density, one obtains the results listed in Table 1.6.

Table 1.6: Image size in focal plane for different grating groove densities

G	α_{min}	α_{cen}	α_{max}	H
600 lines/mm	-0.3°	-5.5°	-10.7°	13.6 mm
1200 lines/mm	-10.7°	-21.5°	-33.1°	29.7 mm
1800 lines/mm	-21.5°	-39.5°	-65°	60.2 mm

For the given focal length of 75 mm and spectral range $300 - 600$ nm, a diffraction grating with 1200 lines/mm accommodates best the image of 29.7 mm in the focal plane.

1.6 Control electronics

1.6.1   Analogue front-end for scattering detection

The simulation of the radiant flux, described in Section 2.4, permitted to estimate the output signal of the selected detector (Model H6780-20). The detector has a current output proportional to the radiant flux received by the cathode [63]:

$$i = FS_c(\lambda)G \tag{1.2}$$

where F - radiant flux, W;

         $S_c(\lambda)$ - cathode radiant efficiency for a given wavelength, A/W;

         G - detector gain, n.a.

Figure 1.13 illustrates how the output current of detector varies with particle size and detector gain. The radiant flux will be estimated in sect. 2.4.

The final step in the scattering detection is now to measure the output current. Generally, it is simpler to measure electric voltage than current. So a current-to-voltage conversion was added to the circuit [64, 65]. Dump resistors, transimpedance amplifiers and current integration or charge amplifiers are the most common methods (Fig. 1.14).

The first method is the simplest one, it does not need active electrical parts, and the signal transfer function is expressed by:

$$U(\omega) = \frac{I(\omega)R}{1 + j\omega CR} \tag{1.3}$$
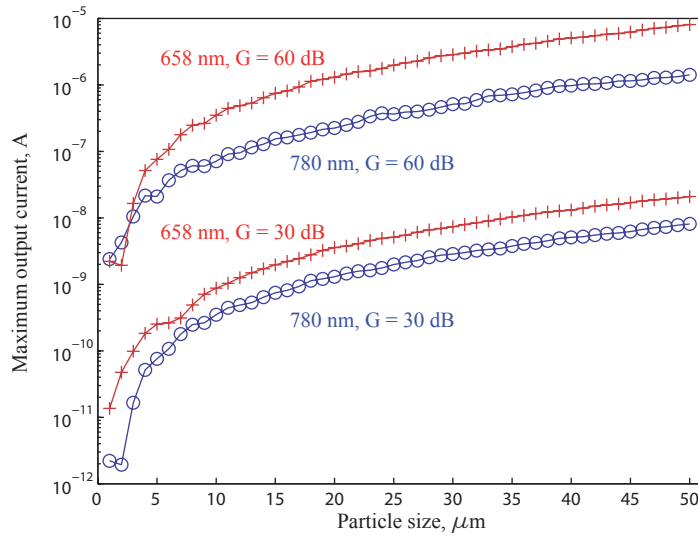
Figure 1.13: Simulation of the maximum output current of the selected multiplier: $658\,\mathrm{nm}$ (red line); $780\,\mathrm{nm}$ (blue line).
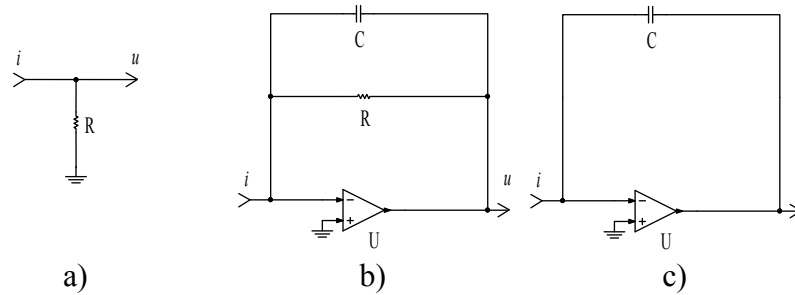
Figure 1.14: a) dump resistor; b) transimpedance amplifier; c) current integration (charge amplifier) : C - feedback capacitor; R - feedback/dump resistor; U - operational amplifier.

where $U(\omega)$ - output voltage, [V];
       $I(\omega)$ - input current, [A];
       R - resistance value, [Ω];
       C - total capacity seen by the signal, [A];
       ω - real frequency, [Hz].

The total capacity is a sum of the detector's output capacity, cable capacity and measurement instrument capacity. It normally ranges in $10 - 100\,\mathrm{pF}$ and significantly limits the bandwidth. For high R values (more than $1\,\mathrm{M}\Omega$), the response time becomes much larger than the transition time for a single particle through the laser beam. As consequence, the dump resistor conversion was unacceptable the

light scattering measurement.

The second method uses an operational amplifier with non-inverted input fixed on a virtual or true ground, and inverted input connected to the detectors output. A negative feedback circuit contains one resistor for gain setting and one capacitor for amplifier stabilization. The transfer function for DC current is simply : $u = -i \cdot R$ and the cut-off frequency is [66, 67]:

$$f_{-3dB} = \sqrt{\frac{GBW}{2\pi C_T R_F}} \quad (1.4)$$

where GBW - gain-bandwidth product of the selected amplifier, Hz;
C_T - total capacitance on the inverting input; includes output detector capacitance, cable capacitance, amplifier input capacitance, F;
R_F - feedback resistance, Ω.

One can notice that the cut-off frequency is proportional to the square route of the total input capacitance, which differentiates it from the case of a simple dump resistor. This technique of current-to-voltage conversion is commonly used for high speed detectors and/or for very high gain applications. As its name indicates, this circuit serves to convert a high impedance source to a low impedance source, or in other words a weak current source to a strong one. This method is ideally suited for the light scattering measurements thanks to this combination of high gain high cut-off frequency.

The last method is a current integration amplifier or also called charge amplifier [68]. It employs a feedback capacitor C to stock incoming electrical charge, which is converted into voltage. In the time domain, this dependence can be expressed as:

$$u(t) = \frac{1}{C} \int_0^{T_{int}} i(t)\mathrm{d}t \quad (1.5)$$

where T_{int} is the integration time, s.

In the frequency domain, its transfer function is:

$$U(\omega) = \frac{I(\omega)}{j\omega C} \left(cos(2\pi T_{int}\omega) + 1\right) \quad (1.6)$$

As it can be seen from this equation that the bandwidth is limited by the input resistance and integration time. The first is generally not an issue thank to many high speed operational amplifiers on the market. The second parameter T_{int} is more important and determining the performance. Any integration amplifier contains an additional circuit to reset the charging capacitor built on two switches: one

connects and disconnects the input; the second one connects the capacitor to the ground. The fast switching process is very noisy, and decreases the whole integrator signal-to-noise value.

Finally, a simple example can be taken to see the differences in transfer functions for the three described methods. Figure 1.15 shows their performances for 60 dB gain with standard high speed operational amplifiers (OPA847 and IVC102).
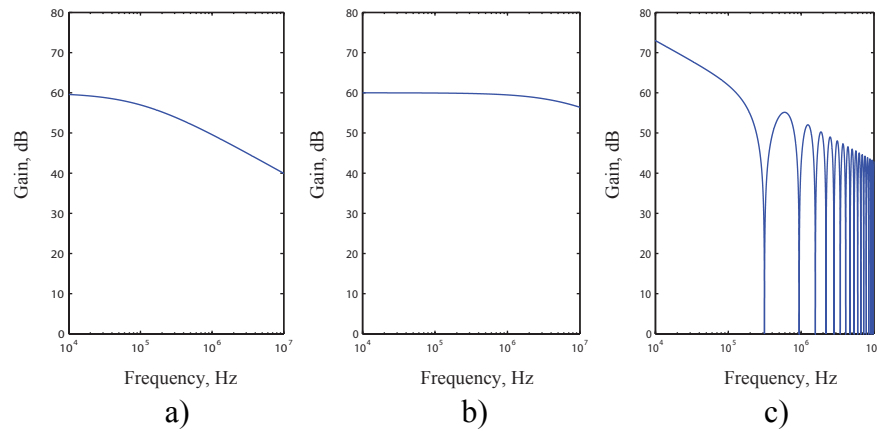
Figure 1.15: Example to obtain the same gain $G = 60$ dB : a) $R = 1$ MΩ, $C_{in} = 10$ pF ; b) $R = 1$ MΩ, $C_{in} = 10$ pF, $C = 2$ pF, GBW $= 3.9$ GHz with OPA847; c) $C_{in} = 10$ pF, $C = 10$ pF, $T_{int} = 10$ μs with IVC102.

After this detailed analysis of the current-to-voltage conversion techniques, it was decided to use the transimpedance circuit. It connects the photomultiplier detector to an analogue to digital converter (ADC) as shown in Figure 1.16. The gain of the detector and conversion circuit must match the voltage range admitted by the selected ADC. Table 1.7 summarises all electrical components discussed before.

1.6.2   Analogue front-end for spectrum detection

It was already described in details how one can convert and acquire the signal of a current output photomultiplier in the scattering detection section. The particularity of fluorescence detection is that the duration of fluorescence signal is rather short (few ns for the case of this work). So from the detection point of view, the signal is fast, and any limitation of bandwidth will decrease its amplitude. It follows that methods with dump resistor and tranimpedance amplifier will not be fast and sensitive enough. The integration amplifier has the huge advantage of collecting
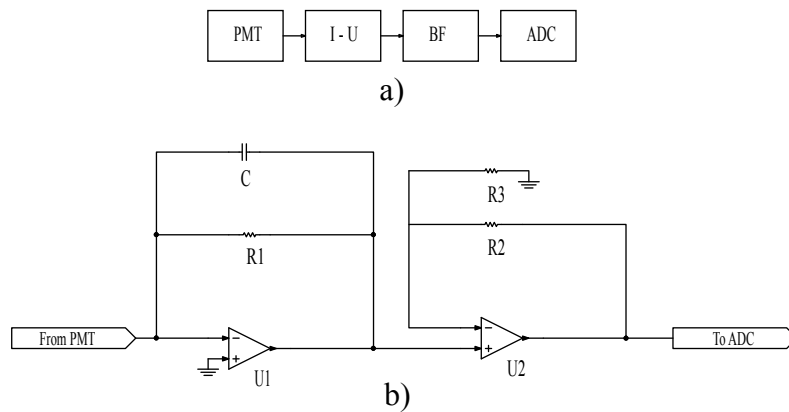
Figure 1.16: a) Basic scheme of the electronic front-end: PMT - photomultiplier; I-U - current to voltage conversion; BF - buffer amplifier; ADC - analogue to digital converter; R_1, R_2, R_3 - gain setting resistors; U_1, U_2 - operational amplifiers

Table 1.7: Electrical components of the scattering detection electronics

Stage	Main component	Description
Transimpedance amplifier	LMP7715	Low noise CMOS operational amplifier; stage gain 10^5 V/A
Buffer amplifier	ADA4899	Low noise high speed operational amplifier; stage gain 10 V/V
Analogue to digital converter	AD7985	16-Bit, 2.5 MSPS PulSAR ADC; input range $0 - 4.096$ V; resolution 125 µV

all incoming electric charge from the detector even if generated during a few ns. Figure 1.17 shows the basic scheme that was employed for each of the 32 pixels of the detector. The acquisition is done in parallel.
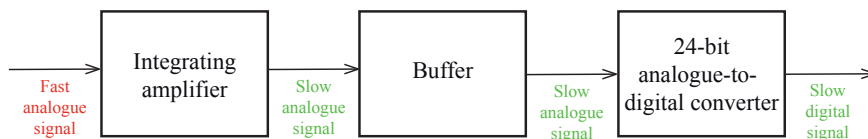
Figure 1.17: Analogue front-end scheme for each pixel of the H7260-03 detector.

1.6.3 Control electronics: hardware

The system (Fig. 1.18) is built around three field programmable gate arrays (FPGA) [69]: two Spartan-3AN with 256k logic gates (PL1) and one Spartan-3AN with 780k logic gates (PL2) from Xilinx Corp. The whole electronics is physically split in four separate cards. The fist one contains chip PL2 and communication devices to a host computer (CHC) by USB and Ethernet interfaces. The second one acquires the signal from detectors PM1 (TIA+AD1), generates a trigger signal by use of a fast voltage comparator (VOC), adjusts the gain of PM1, and communicates with PL2. The third card contains the analogue front-end for PM2 with integrating amplifiers (ITA) and precise analogue-to-digital converters (AD2). The last card has a high voltage supply (HIV) controlling the gain of PM2.
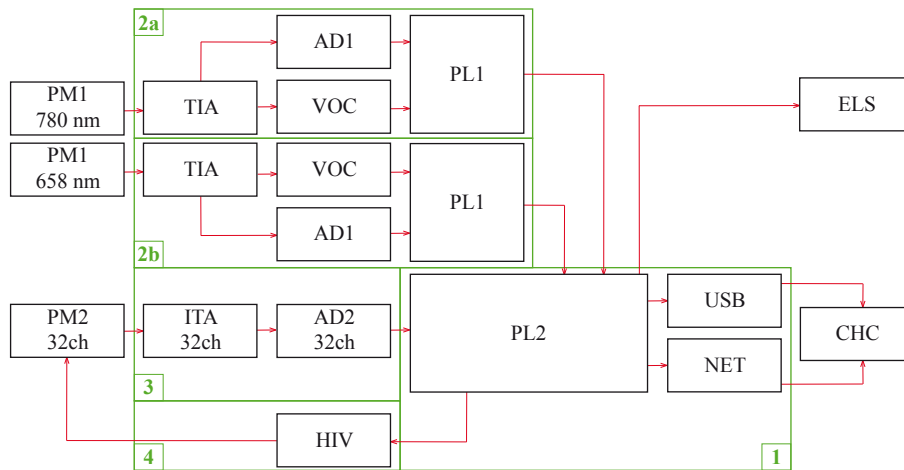
Figure 1.18: Control electronics structure: PM1 - H6780 detector; PM2 - H7260 detector; TIA - transimpedance amplifier; ITA - integrating amplifier (32 channels); AD1 - 16-bit single channel 2.5 MSPS analogue-to-digital converter; AD2 - 24-bit 32 channel 128 kSPS analogue-to-digital converter; PL1 - programmable logic Spartan-3AN 256k; PL2 - programmable logic Spartan-3AN 780k; HIV - high voltage source; EST - excitation light source; CHC - control host computer.

1.6.4 Control electronics: software

The software level is represented by the internal structures of PL1 (Fig. 1.19) and PL2 (Fig. 1.20). These structures were written and programmed on very high density logic (VHDL) language [70] with ISE Design Suite from Xilinx Corp. It can be represented as blocks with inputs/outputs built on basic logical elements to execute a well defined function.

The chip PL1 is programmed to detect and acquire short spikes above noise level from PM1 detectors. Only signals that have a duration ≥ 1 µs are validated and digitized. This condition was established from the fact that a single aerosol particle would need at least this time to cross the CW lasers' spots at FHWM. All shorter pulses are eliminated. The trigger signal and acquired data vector are then sent to the chip PL2.
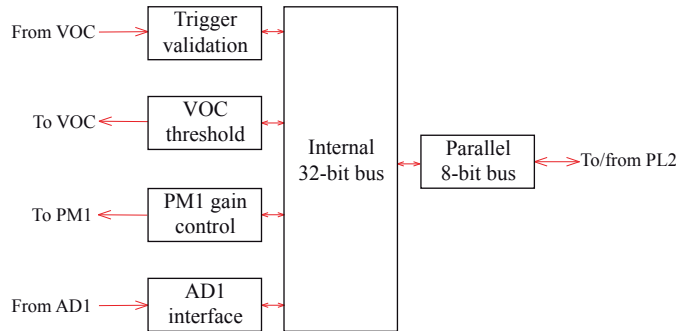
Figure 1.19: PL1 internal structure.

The programmable logic PL2 receives triggers and data from PL1a,b and verifies coincidence condition. Once again, coincidences must last for more than 1 µs to be accepted. After that, the time machine block is enabled. It synchronizes gate signals of integrating amplifiers, excitation light source (Xenon flash lamp or femtosecond laser), and sends the collected data to a host computer.
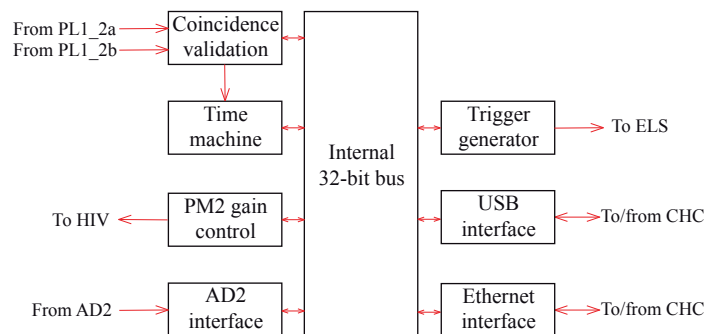
Figure 1.20: PL2 internal structure.

The designed system is capable of treating 1000 events per second but this number is reduced to 10 events per second due to the bandwidth of the used USB or Ethernet interfaces. The transferred data include two traces of scattering light (64 points of 16-bit resolution) and on trace of spectrum (32 point of 24-bit resolution).

1.7 Final design

Nozzle   Scattering detection PMT   Detector   Power supply

Reflective objective   Chamber

a)   b)
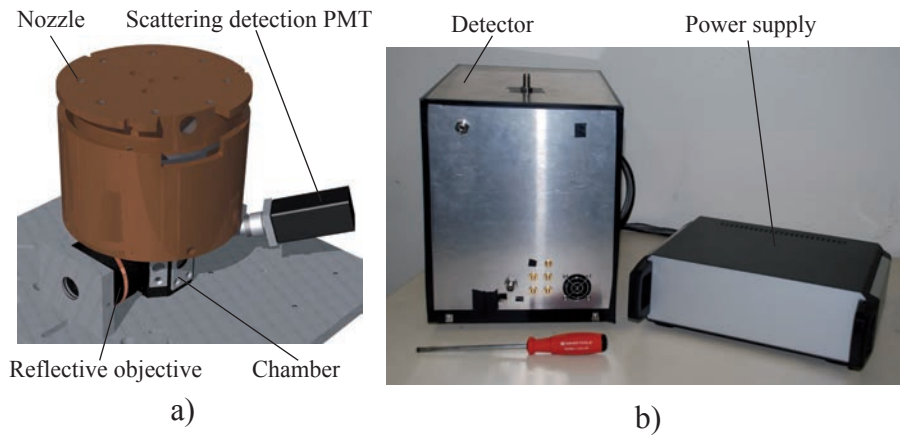
Figure 1.21: Final design: a) CAD drawing of the main parts,
b) Photograph of the aerosol detector.

Figure 1.21 shows a CAD drawing of the main components (a) and a photograph
of the realized detector (b). The device is compact, transportable and robust, it can
be controlled remotely via network and it works stand-alone.

1.8 Aerosol generation

1.8.1 Introduction

The experiments described in the next chapters were done with single aerosol particles on the fly. Thus, a stable generation system was needed to realize them properly. To be able to test different sample particles (biological and non-biological) and also different sizes (from 1 μm to 50 μm), it is necessary to have one or few generation systems to cover all this variety. Many commercial systems are actually available on the market, but unfortunately it is still difficult to find a generator for large particles (more than 20 μm), practical and cost-effective. For these reasons, it was decided to develop a simple generator for the large size range.

1.8.2 Sample microparticles

There were few types of particles used in the experiments described later in this thesis:

- polyethylene microspheres doped with dyes;

- soda lime solid glass microspheres;

- silica microparticles doped with dyes;

- pollens.

The complete list of the commercial non-fluorescent microspheres is given in table 1.8, fluorescent particles - 1.9 and pollens - 1.10.

Table 1.8: Non-fluorescent microspheres

Name	Description	Supplier	Sup. ref. number
Soda lime solid glass micro-spheres	Mean size $4 - 6$ μm, refraction index 1.51	Cospheric	P2011SL
Soda lime solid glass micro-spheres	Mean size $10 - 12$ μm, refraction index 1.51	Cospheric	P2015SL

Table 1.9: Fluorescent microspheres

Name	Description	Supplier	Sup. ref. number
Polyethylene fluorescent micro-spheres	Mean size $20 - 27$ μm, fluorescence : 530 nm (ext. 355 nm)	Cospheric	UVPMS-BG-1.025
Polyethylene fluorescent micro-spheres	Mean size $27 - 32$ μm, fluorescence : 530 nm (ext. 355 nm)	Cospheric	UVPMS-BG-1.025
Polyethylene fluorescent micro-spheres	Mean size $38 - 45$ μm, fluorescence : 530 nm (ext. 355 nm)	Cospheric	UVPMS-BG-1.025
Polyethylene fluorescent micro-spheres	Mean size $53 - 63$ μm, fluorescence : 530 nm (ext. 355 nm)	Cospheric	UVPMS-BG-1.025
Fluoresbrite carboxylate micro-spheres	Mean size 1.75 μm, fluorescence : 400 nm(ext. 355 nm)	Polysciences	Cat. : 17686 - 5
Fluoresbrite carboxylate micro-spheres	Mean size 6 μm, fluorescence : 400 nm(ext. 355 nm)	Polysciences	Cat. : 19102 - 2

Table 1.10: Pollens

Name	Description	Supplier	Sup. ref. number
Paper Mulberry pollen	Mean size $10 - 12$ μm	Polysciences	Cat. : 07670
Ragweed pollen	Mean size $19 - 20$ μm	Polysciences	Cat. : 07673
Pecan pollen	Mean size $45 - 52$ μm	Polysciences	Cat. : 07671
Corn pollen	Mean size $85 - 90$ μm	Polysciences	Cat. : 07664
Sporopollenin	Mean size 100 μm	Polysciences	Cat. : 16867

As it can be seen, the size and the nature of the particles are rather different. Moreover, some microspheres can only be conserved in liquid solution. As consequence, it was impossible to use only one generation system:

- for small microspheres (diameter $d \leq 2$ µm), we opted for an atomizer based generation followed by a drying tube;

- for larger diameters (diameter $d \geq 2$ µm), the generation was done from dry powder by using a magnetic steering rod set-up.

1.8.3 Generation of small size aerosols ($d \leq 2$ µm)

To generate small size aerosols, a commercial available system was used, the Aerosol Generator 3076 from TSI Corp. Its main characteristics are shown in table 1.11.

Table 1.11: Characteristics of generator 3076

Parameter	Value
Cut-off size	2 µm
Flow rate	3 L/min
Maximum particle concentration	10^7 particles/cm^3

The generation system contains three main parts shown in Figure 1.22:

- air drying tube and filters (TSI Filtered Air Supply 3074);

- atomizer TSI Aerosol Generator 3076;

- drying tube for outlet (custom made).

The drying tube for outlet uses silica drying crystals (BASF cat.num. : 54097617)

1.8.4 Generation of large-size aerosols ($d \geq 2$ µm)

This range of sizes includes some non-biological microspheres listed in Tables 1.8 and 1.9, and pollens (Table 1.10). Pollens could not be dissolved in water or in other solution without significantly changing their size and some other important properties (i.e. fluorescence).
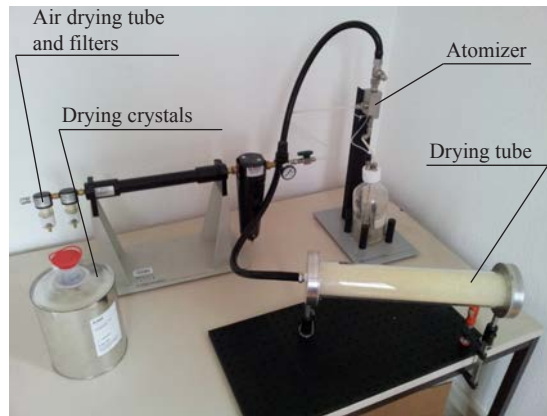
Figure 1.22: Small-size aerosol generator.
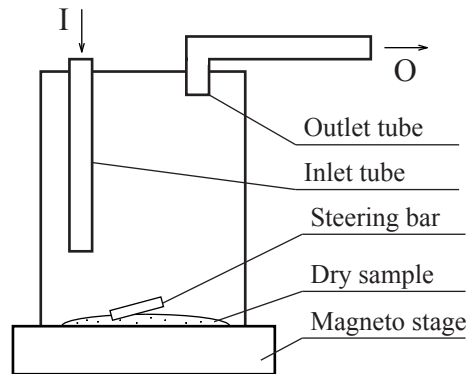
Figure 1.23: Principal scheme of steering rode based generator.

The generator is based on a commercially available reservoir (Alphacool mod. : 15718) originally dedicated to stock cooling liquid in the water cooled systems for microprocessors. It has three ports with standard G1/4" threads on one side and one port on the other side. For the aerosol generation only two ports were used. Figure 1.23 shows a basic scheme of the designed generator and Figure 1.24 presents its actual picture. It is comprised of:

- inlet tube;

- outlet tube;

- steering rode;

- magneto stage.

Sample particles in dry solution are placed on the bottom of the reservoir. Pure air is injected by the inlet tube and outputs by the outlet tube. When steering bar

rotates, it raises deposed particles that acquire initial velocity in the gas flow. Depending on the inlet tube length, rod rotation speed and particle size, the generation process can be more or less efficient.
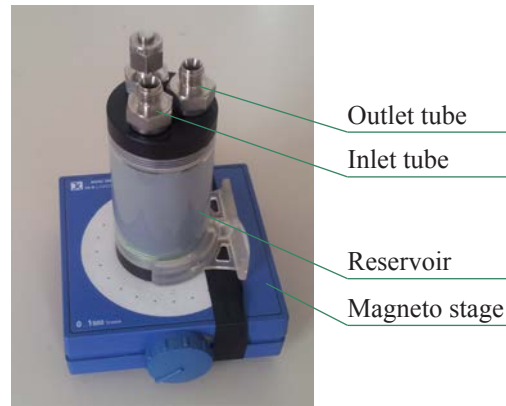
Figure 1.24: Generation system for large-size aerosols.

Figure 1.25 shows the air flow inside the generator and the particle path tracing simulated with Comsol Multiphysics. The particles (water droplets) have an initial velocity of 1 m/s in the horizontal plane to simulate a steering bar. It demonstrates that for this given geometry, the generation process is rather efficient for the particle sizes up to 40 μm. In practice, the generator was able to produce aerosols with the nominal sizes up to 50 μm.
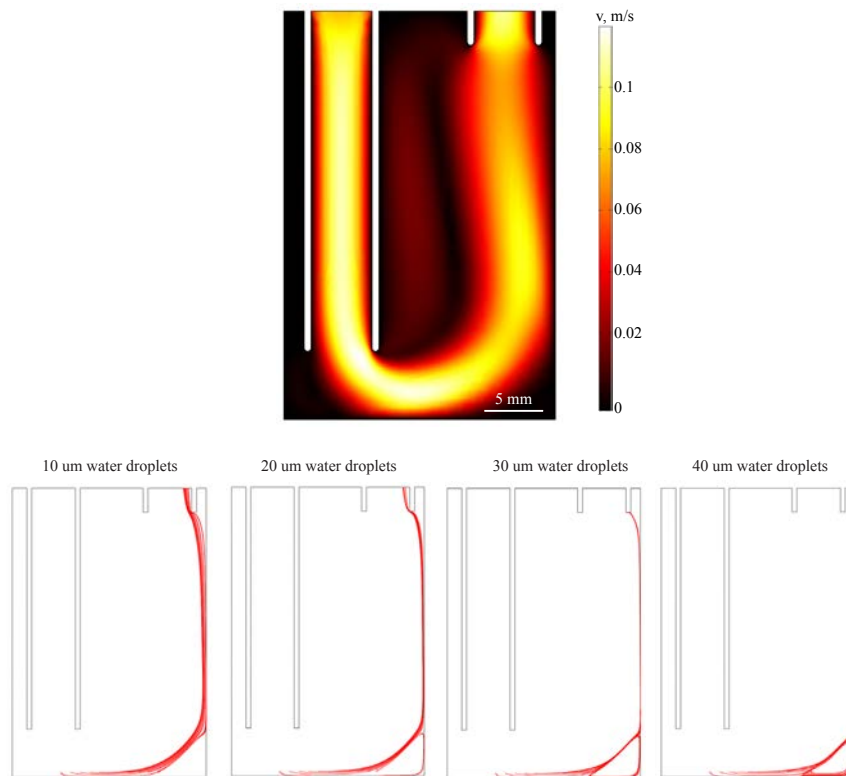
Figure 1.25: Simulation of the internal air flow and path tracing for the water droplets.

Chapter 2

Simulation and component characterizations

2.1 Injection nozzle simulations

To verify that the designed nozzle (see Sect. 1.1) has suitable specifications, the inner air flow was simulated with Comsol Multiphysics, which is a complete finite element solver software dedicated to various fields of physics including flow dynamics. The simulation was done with the initial parameters given in Table 2.1. Figure 2.1 shows the simulation geometry and the applied mesh.

Table 2.1: Initial parameters for the flow simulation : nozzle

Parameter	Value	Remarks
Simulation model	Incompressible Navier-Stocks model	Valid for low speed gas flows and liquids
Type of simulation	Stationary flow	
Main inlet flow	0.5 l/min	
Auxiliary inlet flow	0.5 l/min	
Outlet relative pressure	0 Pa	The outlet is under normal atmospheric pressure
Air density	$1 \mathrm{~kg/m^3}$	Normal conditions
Air dynamic viscosity	$1.8 \cdot 10^{-5} \mathrm{~Pa \cdot s}$	Normal conditions
Boundary conditions	walls (zero velocity)	
Used solver	Direct UMFPack	
Relative solver tolerance	$1 \cdot 10^{-6}$	
Maximum number of iterations	25	
Mesh elements	5652	
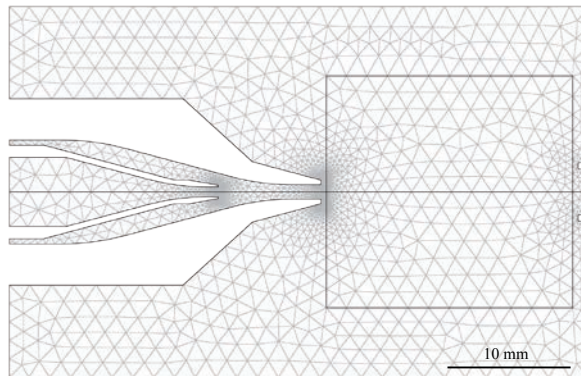
Figure 2.1: Geometry and meshing.

Figure 2.2 represents the resulting air flow of the nozzle. It is given in form of arrows, their length and directions are calculated as:

$$R_i = \sqrt[2]{V_{xi}^2 + V_{yi}^2}; \; \theta_i = atan\left(\frac{V_{yi}}{V_{xi}}\right); \tag{2.1}$$

where R_i - arrow length, m/s;
θ_i - arrow direction angle, °;
V_{xi}, V_{yi} - X and Y components, m/s.
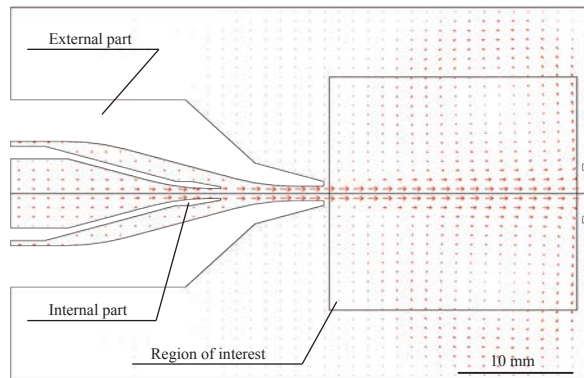
Figure 2.2: Flow simulation of the nozzle outlet.

Another way to present the results is to calculate the amplitude of the velocity field (Fig. 2.3) at each point (node of the mesh).

$$A_i = \sqrt[2]{V_{xi}^2 + V_{yi}^2}; \tag{2.2}$$

where A_i - amplitude at given node i, m/s;
V_{xi}, V_{yi} - X and Y components, m/s.
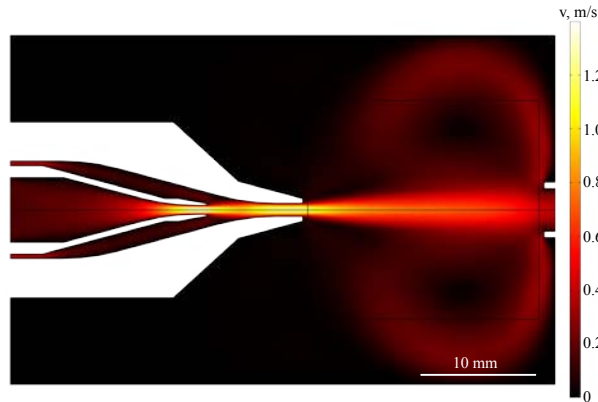
Figure 2.3: Nozzle velocity field.

Given the velocity field, it is possible to calculate single particle path-lines that will illustrate the behaviour of randomly injected particles in the air stream. There are two basic models for this:

- massless particles;

- particles with mass.

The first approach (Fig. 2.4) can be used for the small particles (less than 10 μm). The particles in this case have negligible inertia, thus they follow the stream lines of the flux. To obtain path tracing, Comsol Multiphysics relies on solution of the following equation:

$$\frac{d\overrightarrow{x}}{dt} = \overrightarrow{V};$$

(2.3)

where x - coordinate vector, m;
        V - velocity vector, m/s.

The second approach takes into account the mass of individual particles. It is general and can be used for all sizes and masses of particles. Sect. 1.2.4 explains the physical basis of this method. The path-lines are calculated by solving the following differential equation based on the Richardson-Kahn force expression [71]:

$$\frac{d\overrightarrow{x}}{dt}m_p = \frac{\pi}{4}d^2\rho\left|\overrightarrow{V_i} - \overrightarrow{V_{ip}}\right|^2 \cdot \left(1.84R_{ep}^{-0.31} + 0.293R_{ep}^{0.06}\right)^{3.45};$$

(2.4)

where d - particle diameter, m;
        V_i - flow velocity, m/s;
        V_{ip} - particle velocity, m/s;
        R_{ep} - particle Reynolds number, unitless.
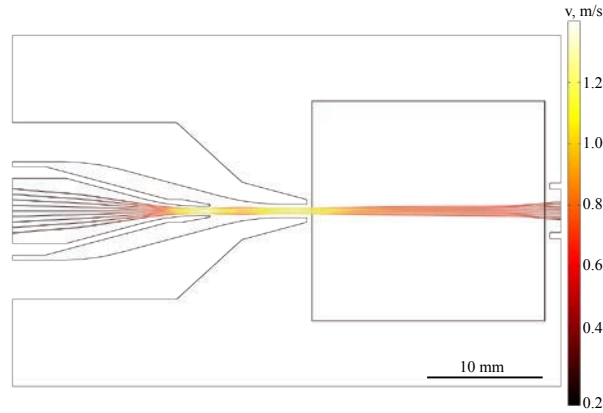
Figure 2.4: Particle path tracing, massless model.

The particle Reynolds number is calculated as following:

$$R_{ep} = \left(\left| \overrightarrow{V_i} - \overrightarrow{V_{ip}} \right|^2 d\rho \right) / \eta \qquad (2.5)$$

where η is their dynamic viscosity.

Comsol Multiphysics can calculate the path-lines using two input parameters: particle mass m_p and particle radius r_p. Simulations (Fig. 2.5) were performed for four typical sizes : 10 µm, 20 µm, 30 µm, 40 µm using for the mass that of a water droplet of equivalent size. The calculations demonstrated that, for the size range used, the particle path line transversal distribution is very low (less than 0.5 mm) at the outlet of the nozzle. According to simulations, the designed nozzle is therefore well suited for the aerosol experiments.

2.2   Injection nozzle test

To confirm the simulations and validate the design, a test was made on water droplets. A standard home vapour generator was used to produce droplets within a size range $1 - 100$ µm. For this measurement, a CCD camera 0.8 MP PL-B953 from Pixelink with a 10x, long working distance lens were employed to monitor the flow at the output of the nozzle. To visualize the stream of water droplets, a CW diode laser focused in the vertical plane was employed. The laser beam formed a thin light sheet crossed by the flow. The light scattering intensity is proportional to the density of droplets in the beam. As a consequence, only the part of the beam crossed by a high number of particles is visible for the camera.

The calibration of the measurement was done with a 0.5 mm metal wire placed into the laser beam through the nozzle. By counting the number of pixels of its
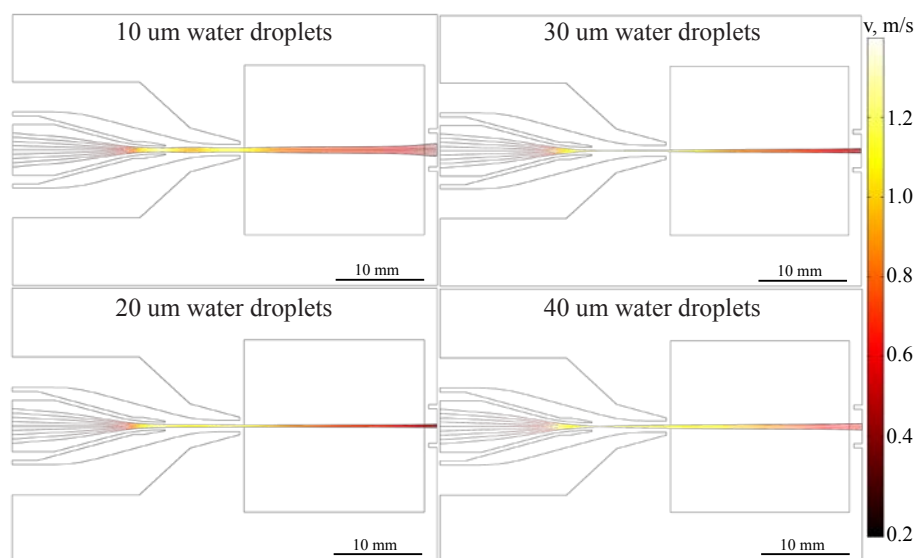
Figure 2.5: Particle path tracing, particle with mass model.

image, the ratio between object and image size was calculated. The precision of the method which is limited by the resolution of the camera and quality of the imaging optics, was estimated to be better than $100\ \mu m$. The size of the vapour stream was determined by Gaussian fitting the image slices at different heights. Figure 2.6a reports photographs of the stream, and Figure 2.6b shows the retrieved stream size. This test ensured us of the very good performance of the designed nozzle for generating a thin laminar flow right after the outlet.

2.3 CW lasers

The beam profile of each laser (Fig. 2.7) was measured with an optical arrangement made of a couple of spherical and cylindrical lenses. The results are shown in Figure 2.8. For these measurements a beam profiler LBP-3-USB-A from Newport was employed. The detector was placed at the position corresponding to the flow of particles. The experimental beam profile is optimal for the aerosol experiments as it is thin in vertical plane (important for coincidence detection) and enlarged in horizontal plane (not sensitive to different trajectories of the particles).

2.4 Scattering simulations

With the detection geometry, we estimated the radiant flux in the solid angle of the detector, scattered from different size particles. To do this, a numerical simulation based on the Mie scattering theory was done in Matlab. Annexe 6 details
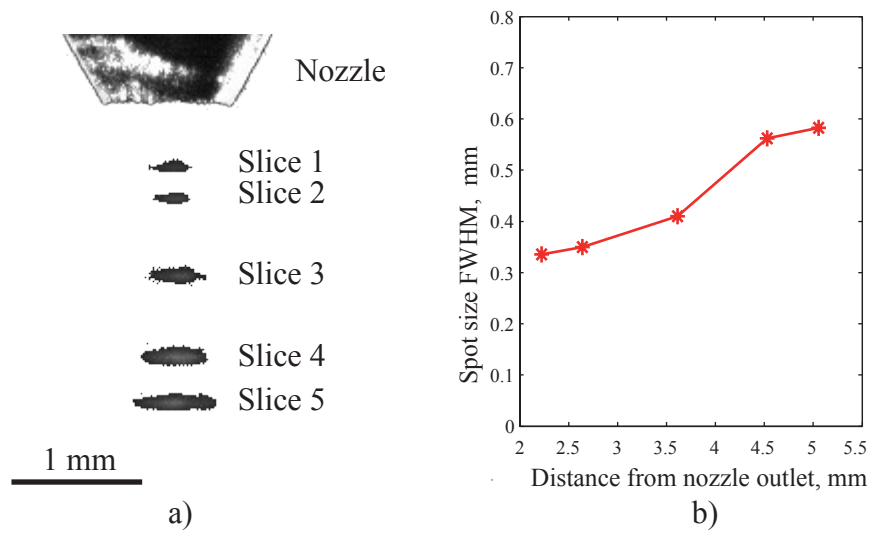
Figure 2.6: Nozzle test on water droplets. a) Photograph of the different slices of the droplet stream. The background is subtracted. b) Spot size dependence on distance from the outlet.
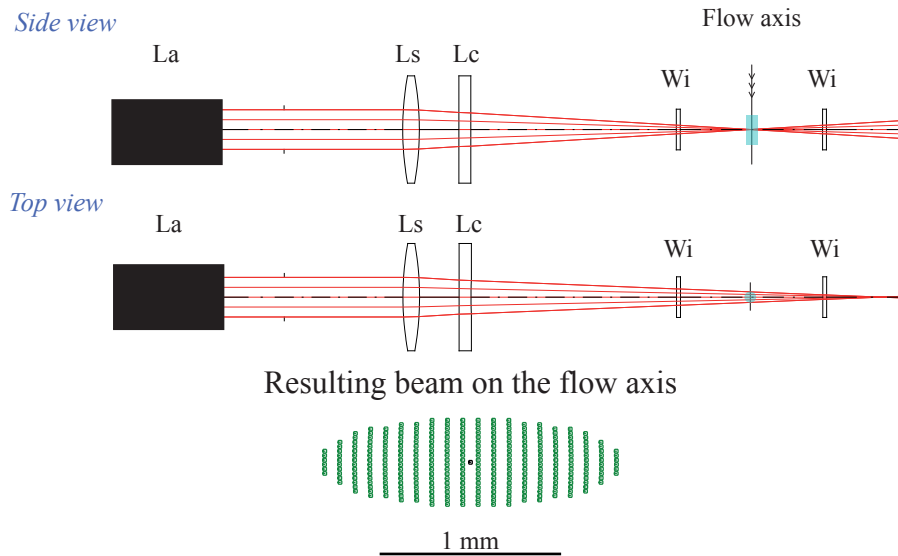
Figure 2.7: CW laser focusing : La - CW laser; Ls - spherical lens; Lc - cylindrical lens; Wi - optical window. Laser beam tracing made in Code V, vertical dimensions / horizontal dimensions 10 : 1.

the physical basis of the theory. The functions library developed by Dr. Christian Mätzler from Bern University, freely available on the Web, was used for this
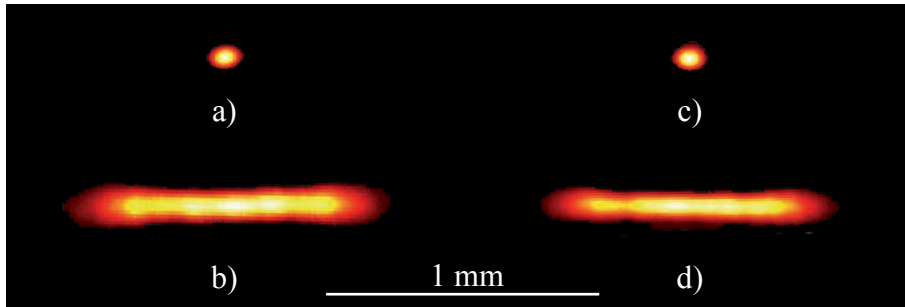
Figure 2.8: CW laser spots : a) 658 nm laser spot with the spherical lens only; b) 658 nm laser spot with the spherical and cylindrical lenses; c) 780 nm laser spot with the spherical lens only; b) 780 nm nm laser spot with the spherical and cylindrical lenses.

simulation.

The starting point is the definition of the radiant flux received by the detector:

$$\mathrm{d}F = I_{sca}(\mathrm{d}\Omega)R^2\mathrm{d}\Omega \tag{2.6}$$

where $I_{sca}(\mathrm{d}\Omega)$ - scattering intensity, $\mathrm{W/m}^2$;

$\mathrm{d}\Omega$ - element of the solid angle seen by the detector, sr;

R - distance between the source (aerosol in the laser beam) and the detector, m.
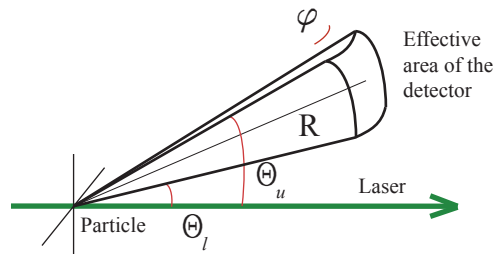
Figure 2.9: Detector field of view.

The solid angle of the detector's field of view (Fig. 2.9) is defined as follows:

$$\Omega = \int_{\phi_l}^{\phi_u} \int_{\Theta_l}^{\Theta_u} sin(\Theta) \, \mathrm{d}\Theta \, \mathrm{d}\phi \tag{2.7}$$

where Θ_l and Θ_u - integration limits defined from $\Theta_c \pm atan\left(\frac{D}{2R}\right) = 19 \pm 2.9°$ with D = 8 mm detector diameter and R = 80 mm detector-particle distance , °;

Θ_c - central angle, °;

ϕ_l and ϕ_u - integration limits, $\pm atan\left(\frac{D}{2R}\right) = \pm 2.9°$.

The integration of the eq. 2.7 gives :

$$\Omega = 0.1\pi \cdot (cos(\Theta_l) - cos(\Theta_u)) \tag{2.8}$$

At the same time, the scattering intensity I_{sca} can be written in terms of incident intensity I_{inc} :

$$I_{sca}(\Theta_i) = I_{inc}\frac{(|S_1(\Theta_i)|^2 + |S_2(\Theta_i)|^2)}{2R^2 \cdot k^2} \tag{2.9}$$

where $S_1(\Theta_i)$ and $S_2(\Theta_i)$ - scattering amplitudes, n.a.;
k - wave number equal $\frac{2\pi}{\lambda}$, $1/\text{m}$.

We integrated this expression numerically for $\Theta \in [\Theta_l; \Theta_u]$. The initial parameters for the simulation are given in Table 2.2.

Table 2.2: Scattering simulations: initial parameters

Parameter	Value
Laser wavelengths λ	658 nm, 780 nm
Distance to the detector R	0.1 m
Detector effective area	$\varnothing 8 \cdot 10^{-3}$ m
Incident laser power, P	1 mW
Laser beam size at the focus, L x W	$3 \cdot 10^{-5}$ m x $1 \cdot 10^{-3}$ m
Refraction index of the particles, m	$1.5 + i \cdot 0$
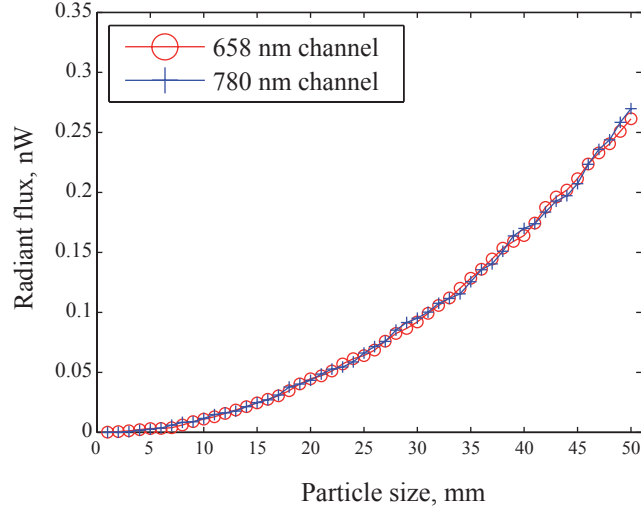
Figure 2.10: Simulation of the scattering power into the solid angle of view of the detector for 658 nm laser (red line) and for 780 nm laser (blue line).

Using these values, one can calculate the scattering amplitudes S_1, S_2, and estimate the radiant flux corresponding to both wavelengths. The results of the simulation are shown in Figure 2.10. It illustrates that for the large particles (more than 5 µm) the dependence on the particle size is almost quadratic. To cover a large range of particle sizes, one needs a detection system that has a dynamical range proportional to the second power of the particle size. However, this problem can successfully solved by adjusting the gain settings of the employed detectors, PMTs for the case of this PhD work.

2.5 Flash lamp characterisation

2.5.1 PAX-10

The filter based on a diffraction grating was built on a transmission grating with groove density 300 lines/mm (see Sect. 1.4.1). The collimated lamp beam passes through the grating and gets diffracted according to:

$$sin(\alpha) + sin(\beta) = nG\lambda \qquad (2.10)$$

where α - incident angle, [°];
            β - output angle, [°];
            n - order of diffraction, [N/A];
            G - groove density, [lines/m];
            λ - wavelength, [m].

Figure 2.11a shows in details the filtering mechanism based on diffraction grating. The incoming collimated light from the lamp crosses the grating and diffracts. The zeroth (black tracing), first and second orders are illustrated. After the diffraction grating, the beam is collected by a spherical lens of 50 mm of focal length. A 1 mm wide slit is installed in the focal plane of the lens in a way that only wavelengths comprised between $250 - 300$ nm pass through. The zeroth and second orders of diffraction are stopped by the slit. Figure 2.11b represents the whole light path. It demonstrate an efficient spectral filtering and does not affect sensibly the beam collimation.

The last stage consists of one or more high performance hard coated multilayer short-pass filters. They are useful to remove residual spectral noise. To build this stage, two filters FF01-300/SP-25 from Semrock Inc. were employed. The results of the spectral filtering with and without diffraction grating are given in Figure 2.12. Using of the diffraction grating permits to have sharp cut-off on the longer wavelength side. The attenuation in this case is also better than using the filter set only. The measurements were done with a fibre spectrometer (USB4000 from Ocean Optics).
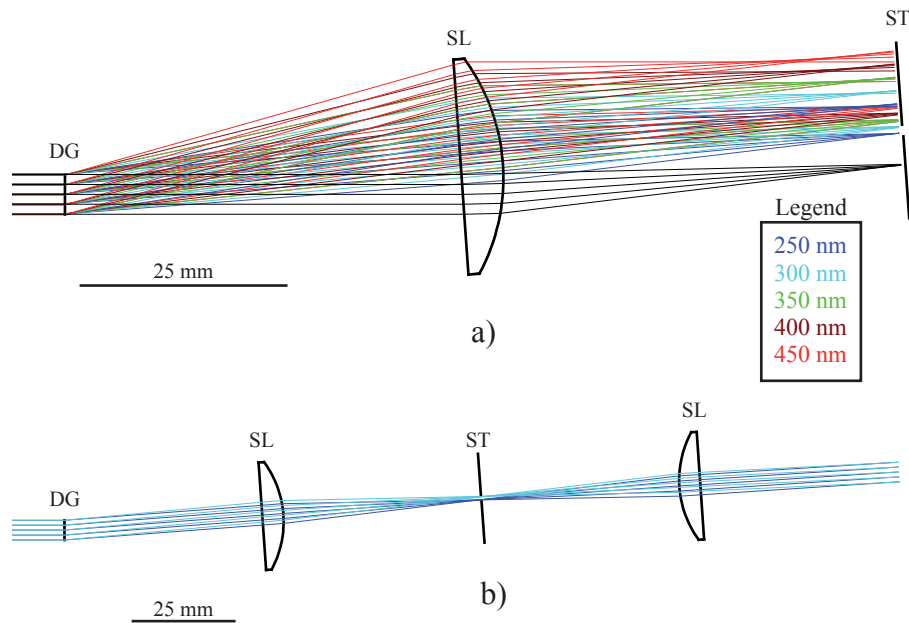
Figure 2.11: Filtering with a diffraction grating: DG - diffraction grating; SL - spherical lens; ST - blocking slit.
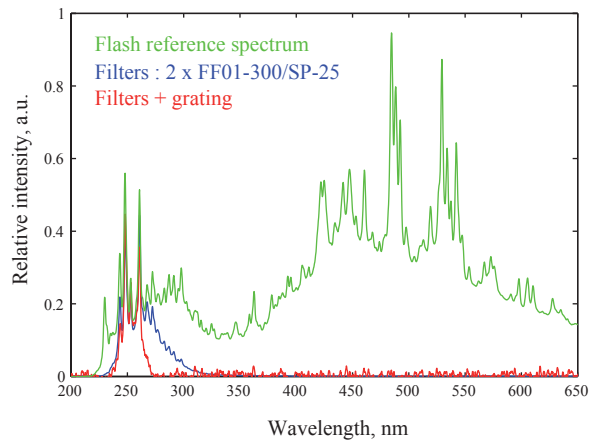
Figure 2.12: Result of application of different filtering techniques: reference spectrum (green line); double filter FF01-300/SP-25 (blue line); double filter FF01-300/SP-25 plus diffraction grating filtering (blue line).

At the end, the design with a spherical lens collection and filtering with diffraction grating were chosen. It also included two FF01 filters. The transmission of different stages in terms of energy loss was then measured and results are given in Table 2.3. It reports measured values of optical energy at the different stages of

the filtering. These measurements were done at 40 Hz repetition rate with portable power meter 407A-2 from Newport Corp. and pyroelectric joulemeter (J3S-10 from Coherent Corp).

Table 2.3: Power throughput for the filter assembly with PAX-10 lamp

Pulse energy	Measurement conditions
3 mJ	PAX-10 output
9 μJ	with two FF01 filters
100 nJ	with two FF01 filters and diffraction grating

This output energy is not sufficient to excite a detectable fluorescence from a single particle [59], so another filtering design and UV light source had to be considered.

2.5.2 FX-4401

The filtering of this Xe lamp was done by combining a narrow bandwidth 266 nm YAG mirrors with FF01 filters. This approach was chosen because this lamp version delivers such a high output power that damage threshold of the transmission diffraction grating was achieved. The resulting spectra for the FX-4401 flash lamp are shown in Figure 2.13. A sharp cut-off could be obtained with YAG mirrors and filters, as in the case of diffraction grating filtering with PAX-10 lamp.
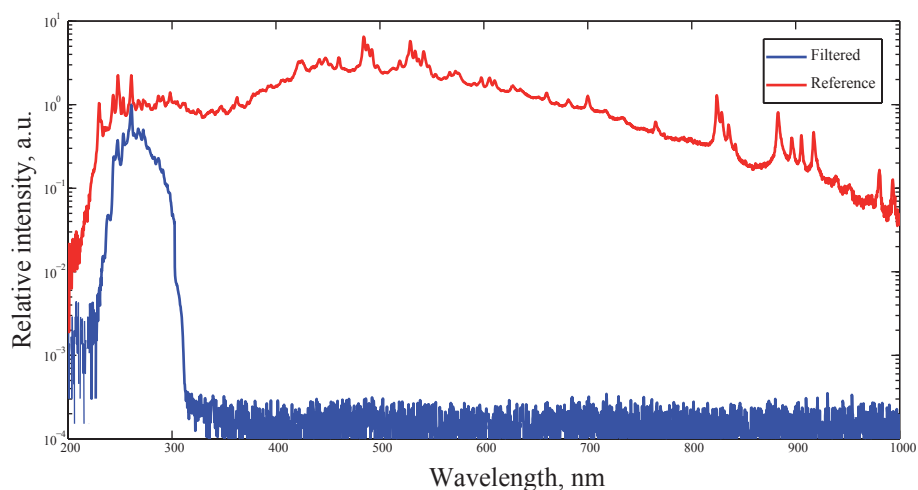
Figure 2.13: Measurement chamber.

The output power measurement for the spectral band $250 - 300\,\mathrm{nm}$, which is presented in Table 2.4, confirmed the efficiency of the filtering schemes based on the narrow band laser mirrors. The measurements were done at $40\,\mathrm{Hz}$ repetition rate with portable power meter 407A-2 from Newport Corp. and pyroelectric joulemeter J3S-10 from Coherent Corp.

Table 2.4: Power throughput for the filter assembly with FX-4401 lamp

Pulse energy	Measurement conditions
$50\,\mathrm{mJ}$	FX-4401 output
$15\,\mathrm{\mu J}$	with four Y4-1025-45 mirrors and two FF01-300SP-25 filters

2.6   Femtosecond laser output stability

An external, on-demand, triggered mode is necessary for using standard CPA designs (see Annexe 8). As a consequence, a test measurement was necessary to determine output power stability and to estimate the maximum excitation yield that can be expected in the experiment. The measurement was done with a standard unbiased photodiode placed into the attenuated output beam. The attenuation is selected to have high signal-to-noise ratio and avoid diode saturation. Figure 2.14 shows the results for a $1\,\mathrm{kHz}$ average pulse repetition rate. In the external triggered mode, the output fluctuations are very significant. Only one pulse out of five would have 80% or more of maximum output energy, which is even more dramatic because multiphoton fluorescence will depend on the second or the third power of the laser intensity. The pump laser needs at least $500\,\mathrm{\mu s}$ after each shot to be ready to shoot again (see Annexe 1.4.2). On the other side, to maintain a mean repetition rate of $1\,\mathrm{kHz}$, the pump will in all cases shoot again after $1\,\mathrm{ms}$. Taking into account the reduced duty cycle, one can expect 1/10 yield or less for multi-photon fluorescence excitation.

To increase the duty cycle and the yield, a test was made at $500\,\mathrm{Hz}$ mean repetition rate. But, as Figure 2.15 shows, the output intensity decreases and most of the outgoing pulses have weak peak power. The real reason of such behaviour has not been discovered even after discussions with experts at Coherent Inc. So keeping repetition rate close to the nominal value of the laser was preferred for the experiments.
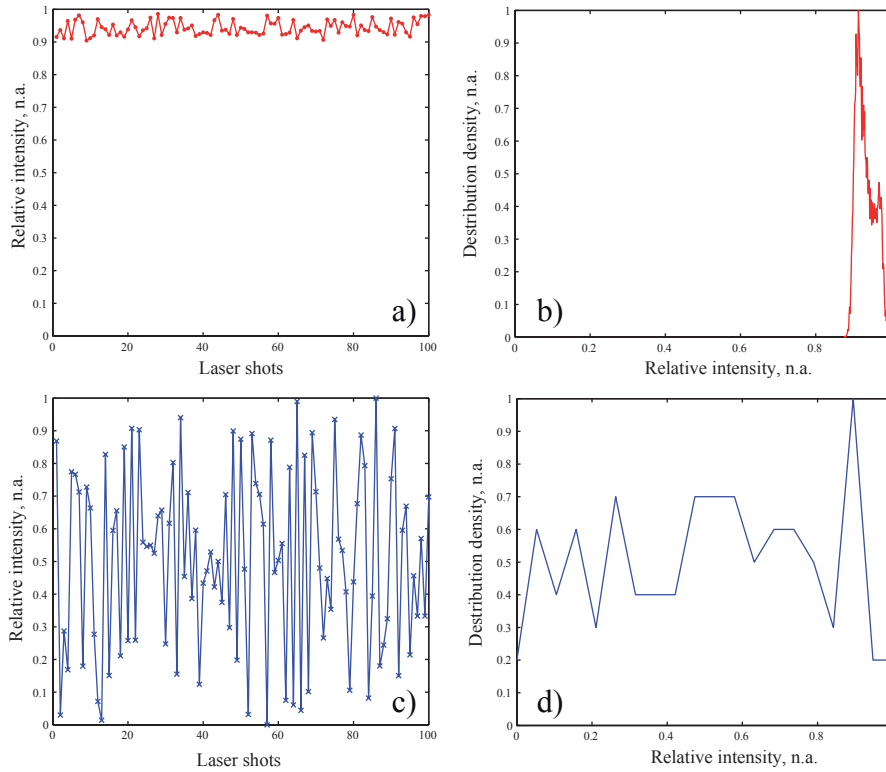
Figure 2.14: Stability measurements on the femtosecond laser output, mean frequency 1 kHz: a) 100 shots in continuous mode; b) Intensity distribution in continuous mode; c) 100 shots in external triggered mode; d) Intensity distribution in external triggered mode.

2.7 Spectrometer simulations

2.7.1 Influence of the focusing lens on spectral resolution

The characteristics of the focusing lens can easily degrade the spectrometer resolution, as demonstrated in Figure 2.16a. Indeed, if one employs a plano-convex lens in such design, the aberrations due to the focal plane curvature are strongly expressed on the edges of the image. It is a common problem for short focus spherical lenses. Moreover, chromatic aberration will also contribute to the image quality degradation. Figure 2.16b shows how the simulated wavelengths fill the detector pixels.

One way to minimize these aberrations without using any custom-made components like aspherical lenses, is to replace the plano-convex lens by a bi-convex lens with the same focal length. The result is presented in Figure 2.17a. The im-
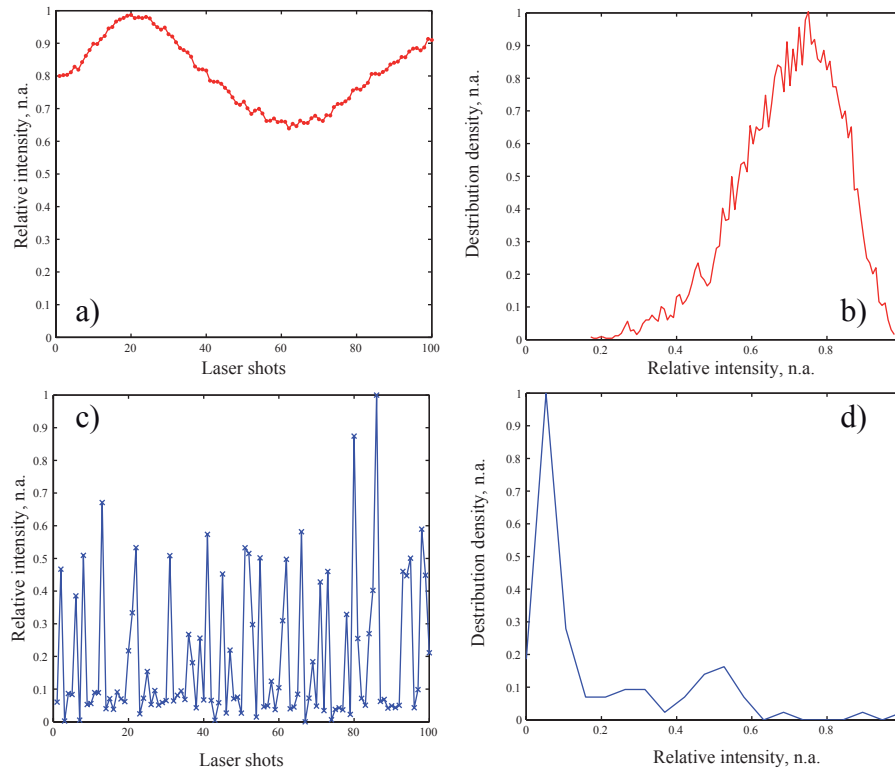
Figure 2.15: Stability measurements on the femtosecond laser output, mean frequency 500 Hz: a) 100 shots in continuous mode; b) Intensity distribution in continuous mode; c) 100 shots in external triggered mode; d) Intensity distribution in external triggered mode.

age quality is significantly improved on the edges but still the extreme wavelengths cover at least two pixels, decreasing the spectral resolution.

2.7.2 Spectral filtering

An additional design was needed to eliminate the residual spectral noise in the $300 - 600$ nm detection band and also to eliminate excitation wavelengths shorter than 300 nm as they can generate fluorescence in the optical components. Moreover, scattering of the exciting UV light can saturate the detector or degrade the signal-to-noise ratio. So a set of filters should by added directly at the output of the objective. It was also mentioned in previous sections that the flash lamp light can enter the measurement chamber from the side or by the fluorescence collecting element. As consequence, a dichroic mirror should be installed in the light path to separate UV light and fluorescence. After tests on different commercially available filters and mirrors, a dichroic FF310-Di01 and filter FF01-300LP from Semrock
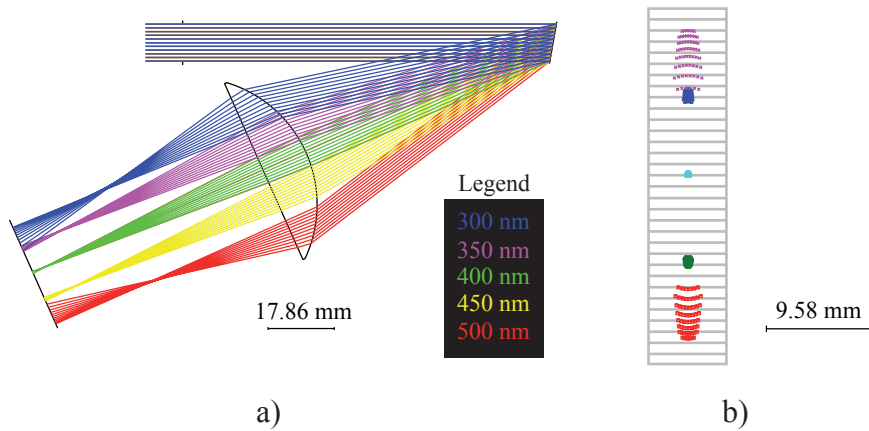
Figure 2.16: Spectrometer design with a plano-convex lens : a) ray tracing for different wavelengths; b) spectrum dispersion in the detector's plane. Simulated with Code V software.
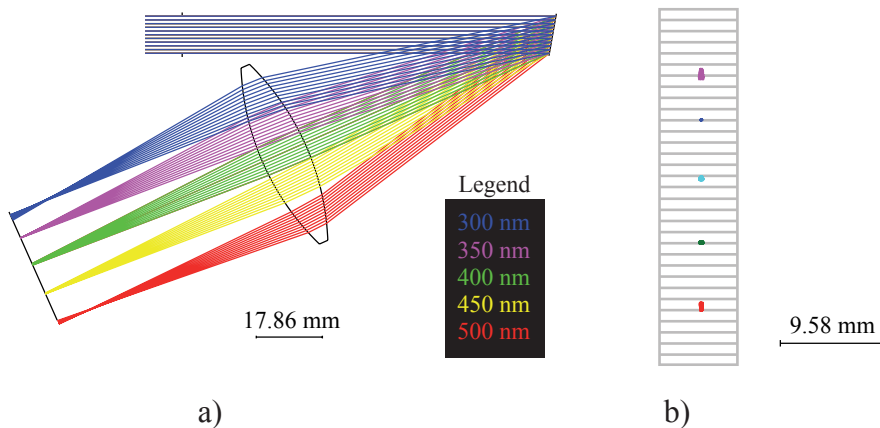
Figure 2.17: Spectrometer design with a bi-convex lens : a) ray tracing for different wavelengths; b) spectrum dispersion in the detector's plane. Simulated with Code V software.

Corp. were chosen. The respective transmission curves and radiant sensitivity of the detector H7260-03 are shown in Figure 2.18.

The combination of the mentioned components permits to achieve a very high attenuation in the $200 - 300$ nm range (> 60 dB or OD6). The low sensitivity of the detector for wavelengths larger than 650 nm and the spatial separation of the wavelengths by diffraction eliminate any need to filter light coming from the two CW lasers (at 658 nm and at 780 nm).
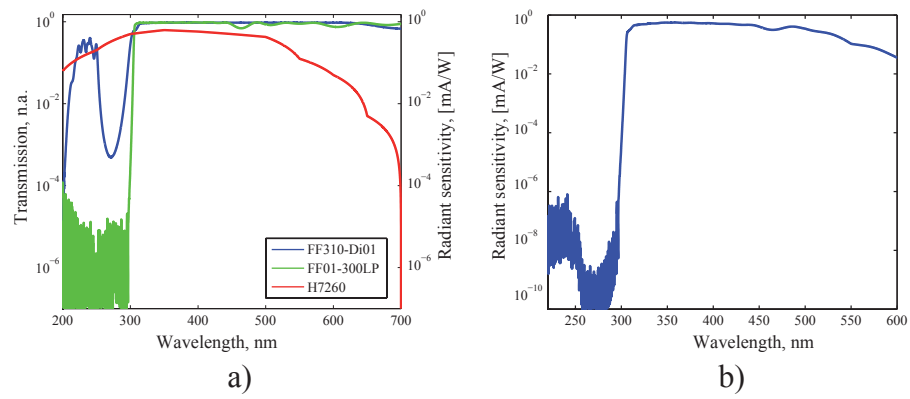
Figure 2.18: a) Transmission curves for dichroic mirror FF310-Di01 (blue), filter FF01-300LP (green). Radiant sensitivity of H7260-03 (red). b) Product of filter transmission and radiant sensitivity.

Chapter 3

Results and discussion

3.1 Scattering detection of non-fluorescent particles

3.1.1 Introduction

Optical counters and optical sizers are very common types of aerosol detectors [72, 73]. The approach is based on Mie theory and employs the property of light scattering by objects with size comparable to the wavelength of incident light. Scattering pattern analysis allows measuring size, shape and complex refractive index of aerosol particles [74, 75, 15, 76]. Since many decades, this technique was often coupled with other measurements on aerosols. The most related to this work is a simultaneous fluorescence and elastic scattering detection [77, 57, 17].

The experiment presented in this section was dedicated to evaluate the capability of the system described in Chapter 1 of detecting single particles and estimating their size. Moreover, an additional measurement of the time of flight through the CW laser beams was performed thank to a rapid acquisition sampling of the scattering signals. The signal duration obtained from it can provide a direct access to the particle velocity in the flow. On the other hand, even if the exact value of the velocity can not be obtained, this measurement can be used as an additional degree of discrimination of aerosol particles.

The experiment was done on the solid lime microspheres P2011SL (mean size 6 µm), P2015SL, (mean size 10 µm), and polystyrene UVPMS-BG-1.025 (mean size 23 µm and 30 µm) described in Section 1.8. Only scattering light measurements were performed in this experiment as not all microspheres were doped with a fluorescent dye. This preliminary test has also played an important role because it permitted qualifying the dynamic range and sensitivity of the scattering detection unit.

3.1.2   Experimental procedure and event statistics

During this experiment four types of aerosol were generated by the large particle size generator (see Sect. 1.8). To exclude pollution from other particles in the chamber, the system was purged with clean air for at least 10 min at every sample change.

Only detection events with simultaneous scattering detection of both lasers were retained for data analysis. The yield of these validated events was calculated as:

$$E_{sc} = \frac{N_{cnd}}{N_{658} + N_{780}} 100\%; \tag{3.1}$$

where N_{658}, N_{780} - total number of detection events on the 658 nm and
            780 nm channels;
            N_{cnd} - number of coincidences.

The yield varied from 10 to 50 %, depending on the size of the particles. It was observed that for larger size particles, the yield was higher.

In these measurements, the gains of both scattering detection PMTs were adjusted so that any particle from a given sample crossing the CW laser spot does not saturate the corresponding PMT. The signals from both PMTs are sampled at 2.5 MSPS (Megasample per second) rate and a detection event is validated if the PMT output signal exceeds a threshold level for more than 0.5 μs. This level is adjusted in real-time by the electronics we developed and calculated from 65000 test points measured each second. These points provide a very accurate value of the background. The threshold for an event detection was established at 105-110 % of the mean background voltage level. In practice, if the mean voltage over 65000 acquired points is 100 mV, then the threshold is set at $105 - 110$ mV.

The raw data for 658 nm are reported in Figure 3.1. The raw data from the 780 nm detection channel were essentially the same. The event statistics of this measurement is given in Table 3.1.

Table 3.1: Scattering detection of polystyrene microspheres

Parameter	6 μm	10 μm	23 μm	30 μm
Total number of events	243	257	56	108
Number of retained events	185	207	46	70
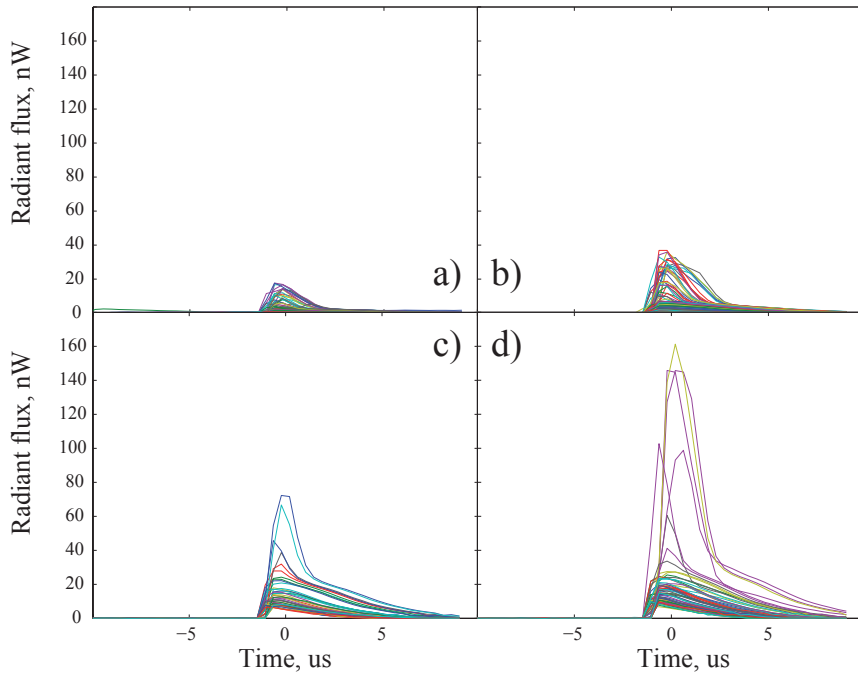
Figure 3.1: Raw data, scattering signals from 658 nm CW laser: a) 6 μm polystyrene spheres; b) 10 μm polystyrene spheres; c) 23 μm polystyrene spheres; d) 30 μm polystyrene spheres.

3.1.3 Data analysis

As one can see from Figure 3.1, the scattering signal varies significantly even within a single sample type. This variability, due to the horizontal flow distribution and inhomogeneous light intensity in the laser spot, strongly complicates the size estimation based on the scattering intensity. To overcome this limitation we first calculated the mean value of peak scattering for both wavelengths over the ensemble of particles from the same type. Then we also evaluated the centres of mass as the distributions of intensity appeared to be non-symmetrical with respect to the mean value of the peak intensity distribution. Figures 3.2 shows the mean scattering signal curves (a) and (b), and the centres of mass for 658 nm (c) and 780 nm (d), respectively. The distribution overlap between the different types of samples is clearly observed, but the centres of mass and the mean values are not identical.

The data can also be represented as histograms, which show the number of events falling into the integration interval of the radiant flux $\Delta F = \frac{F_{max} - F_{min}}{50}$. The interval size was chosen to provide the best data representation. Figure 3.3 gives histogram of scattering signals at 658 nm (a) and at 780 nm (b).
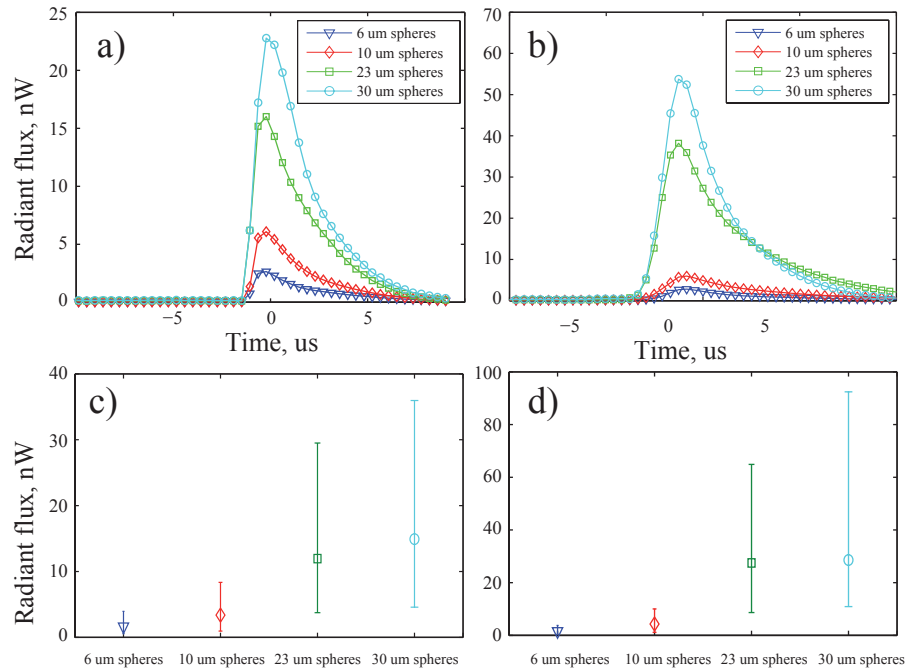
Figure 3.2: a) Mean scattering signals from 658 nm CW laser; c) centres of mass for 658 nm; b) mean scattering signals from 780 nm CW laser; d) centres of mass for 780 nm. Error bars reports interval with 50% of events within it.
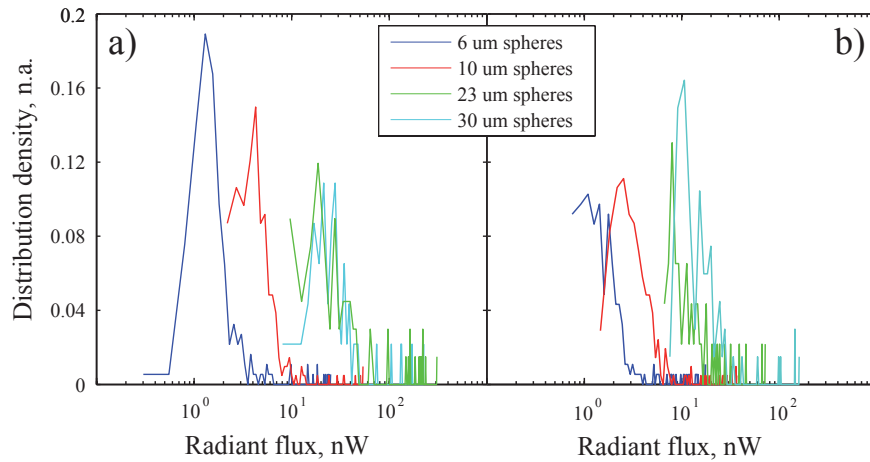
Figure 3.3: Histograms of the radiant flux: a) scattering signal at 658 nm channel; b) scattering signal at 780 nm channel.

The time of flight through the laser beam was also evaluated. The plots (Fig. 3.2a,b) were normalized by their respective maxima. The result, presented in Figure 3.4, demonstrates that no significant difference exists in the signal duration
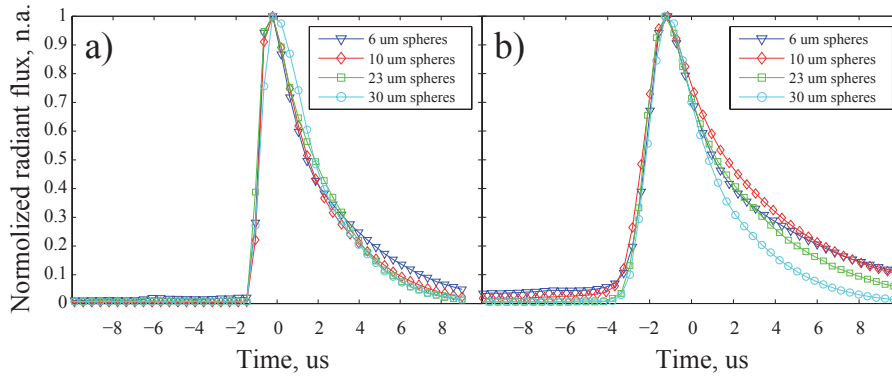
Figure 3.4: Normalized radiant flux: a) scattering signals from 658 nm CW laser; b) scattering signals from 780 nm CW laser.

among the different sample types. Moreover, the signal duration appeared to be very short (rise time $0.6 - 1.2\ \mu s$ and falling time $2 - 2.5\ \mu s$) as compared to the expected value (around $30 - 40\ \mu s$) with a know beam sizes (measured $28\ \mu m$ and $41\ \mu m$ at 658 nm and 780 nm, respectively) and the predicted particle velocity (around 1 m/s, see Sect. 2.1). The signal shape was also highly asymmetrical.
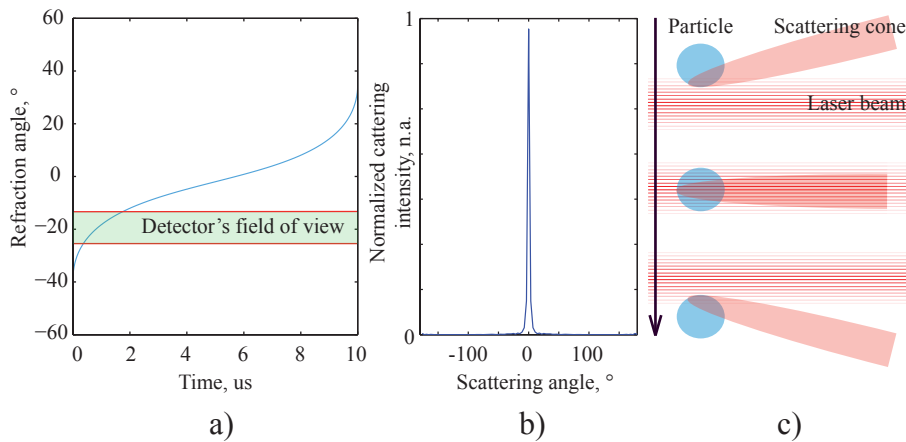
Figure 3.5: Simulation of the particle passage through the laser beam. Particle diameter $10\ \mu m$, beam diameter $10\ \mu m$, particle velocity 1 m/s: a) double refraction angle as function of time, b) Mie scattering profile, c) particle passage through the beam.

To explain this effect, a closer look is needed at the scattering process [78]. All sample particles were much larger than the wavelengths of the CW lasers. In this case, the scattering is mostly governed by the geometrical refraction and reflection

(see Annexe 6). Figure 3.5c illustrates an example of particle passage (diameter 10 μm) through a laser beam (diameter 10 μm) at 1 m/s. When a particle enters the beam, a fraction of the laser light is refracted by the air-particle interface and after by the particle-air interface. Mie theory predicts that light scattering intensity will have an angular distribution (Fig. 3.5b) around the incidence axis defined by the double refraction angle (Fig. 3.5a).

This effect results in that the scattering detector captures only a very short pulse corresponding to the moment when the double refraction angle is equal to the angle between the detector's axis and the laser axis. The non-linearity of the double refraction angle as a function of time explains the asymmetry of the detected signals. Moreover, the scattering cone will narrow down with particle size increasing according to Mie theory. This will lead to shorter rising and falling edges of the scattering signal and this can be observed especially for the 780 nm detection channel (Fig. 3.4b).

According to this explanation, to evaluate the particle velocity one should not use the longitudinal beam size but a much smaller value corresponding to a part of the beam where the refraction axis points to the detector's field of view. Figure 3.4 indicates also that the size of this active scattering zone is not the same for both CW laser beam as the pulse duration differs strongly among all particles. At this stage, the particle velocity can only be estimated from Figure 3.5a and by expanding this simulation to the measured beam sizes.

Figure 3.5a indicates that the time of flight seen by the detector should be around 1.3 μs for a 10 μm laser beam and at 1 m/s particle velocity. This implies that the 658 nm detection channel should capture 3.7 μs pulse duration if the particle velocity is around 1 m/s. The 780 nm detection channel has a larger beam and the expected time of flight would be 5.3 μs. Comparing with the experimental results (Fig. 3.4) indicates that, if this approximate explanation holds, the particle velocity should be around 1 m/s, which fits well the simulated values (see Sect. 2.1).

3.1.4   Discussion

The experiment described in this section demonstrated the capability of the device to detect aerosols by coincidence between two scattering signals. A detailed analysis of these signals shows that for each particle type with its given characteristic size, a distribution of signal amplitudes is obtained. Unfortunately, large signal fluctuations are observed within the ensemble of particle of the same type. There is a dual origin of these fluctuations:

- the distribution of particle sizes;

- the distribution of laser spot intensity or, which is equivalent, particle position in the spot.

Both of these aspects contribute to the observed fluctuations in the signals. From this point of view, the proposed measurement method is not well suited for extracting information from a single particle event. Each aerosol particle crosses the CW laser intersection in an arbitrary point and scatters an amount of light power proportional to the local incident power. So, even if all particles had exactly the same size, the detected signals would have large distributions. However, one can partially overcome this limitation by calculating the mean value or the centre of mass, which were almost identical for each type of particles.

On the other hand, the intensity in the laser beam profiles is not homogeneous as they are spatially shaped by the doublet of the spherical and cylindrical lenses and an iris. Section 1.3 presented the experimental beam profiles and the reasons for spatial shaping.

Despite all these factors, the evaluation of the mean scattering signal and the centres of mass for the same particle type provides access to the particle size on a statistical point of view. These values are proportional to the second power of particle size as expected from Mie theory and calculated in Section 1.3.

One might think at two possible solutions to enable single aerosol particle size measurement:

- enlarge CW laser beams to obtain close-to-constant intensity profiles;

- partially increase the measurement accuracy by calibrating it with a large variety of monodispersed microparticles.

From the technical point of view, the first solution appears to be the simplest, but enlarging the laser beams will strongly increase the number of detected false events (for the spectroscopy measurement that follows) because the coincidence rate originated from several particles will increase. On the other hand, the number of flashes per second (see Sect. 1.4.1) and the field of view of the fluorescence collecting objective (see Sect. 1.5) are limited. Having higher number of coincidence events even from single particles that are outside of the spectrometer's field of view will decrease the total detection yield and the system performance.

The second solution with monodisperse microspheres will only partially solve the problem and the particle flow distribution will still be an issue. So calibration does not seem a viable solution as well.

Finally, the results in Figure 3.4 demonstrated that the time of flight could provide some new information on the scattering process in our experiment. The explanation (Fig. 3.5) of a very short signal duration at both scattering detection

channels was found by evaluating the scattering in details. It appeared that as our detectors had a relatively small field of view, they were sensitive to the scattering pattern rotation during the passage through the beam. This effect is generally ignored in optical counters and sizers because they mainly use large solid angle parabolic reflectors.

Governed by the double refraction, the direction of scattering emission changes during the particle passage and the detectors capture only a short peak when this direction coincides with the detectors. The non-linear behaviour of the double refraction angle (Fig. 3.5a) create the asymmetric responses on the detectors (Fig. 3.4). The detected signal durations indicate that the active scattering zone seen by the detectors is much smaller than the CW laser beams. Moreover, the particle velocity could be estimated from these results and based on the double refraction simulation (Fig. 3.5a). The retrieved value around $1 \mathrm{~m/s}$, agrees well the simulated velocity (see Sect. 2.1).

Further developments based on this hypothesis implies that the detected signal duration is affected by the particle size and shape. This is direct consequence of Mie scattering theory on non spherical particles [79]. The angular distribution of scattering intensity is modified by the size and the shape, thus, it changes the signal duration. It was indeed observed in this experiment on the perfectly spherical particles that the signal duration varies with the particle size (Fig. 3.4). Given a higher temporal resolution, one can imagine obtaining even more precise estimation on the particle size and shape, and extracting a new degree of discrimination from it.

3.2 Spectrally resolved detection of single pollens with a Xenon flash lamp

3.2.1 Introduction

The experiment described in this section was designed to demonstrate that the excitation with a flash lamp and the detection of spectrally resolved fluorescence coupled with scattering signals allow discriminating between different species of pollens (*Morus, Ambrosia, Carya pecan*). These three pollens were chosen because they had been already studied by a few research groups [80, 81, 61] and their fluorescence spectra were measured, yielding a reference to validate our data. Our approach with the flash lamp is of high interest especially for potential practical applications of the device. It also illustrates the potential and sensitivity of the method based on a cost-effective flash lamp excitation, used here for the spectrally resolved fluorescence of single aerosols.

We demonstrate that this approach allows higher discrimination of the pollen samples than spectrally non-resolved methods [19, 42, 81]. It also permits to have

a compact and transportable aerosol detector perfectly suited for in-field spectro-
scopic experiments, which can be an important issue for atmospheric and allergy
studies. In this respect, it is important to point out that the pollen samples are
mostly commercially available in a dried and cleaned form that can affect their
morphology and their allergicity compared to their natural wet form. The devel-
oped detector will let investigate the spectroscopic properties of the natural sample.

3.2.2   Spectroscopy of fluorophores

Pollen grains are complex biological particles containing a large variety of fluo-
rophores [82], including:

- flavins;

- nicotinamide adenine dinucleotide (NADH);

- aromatic amino-acids (Tyrosine, Tryptophan).
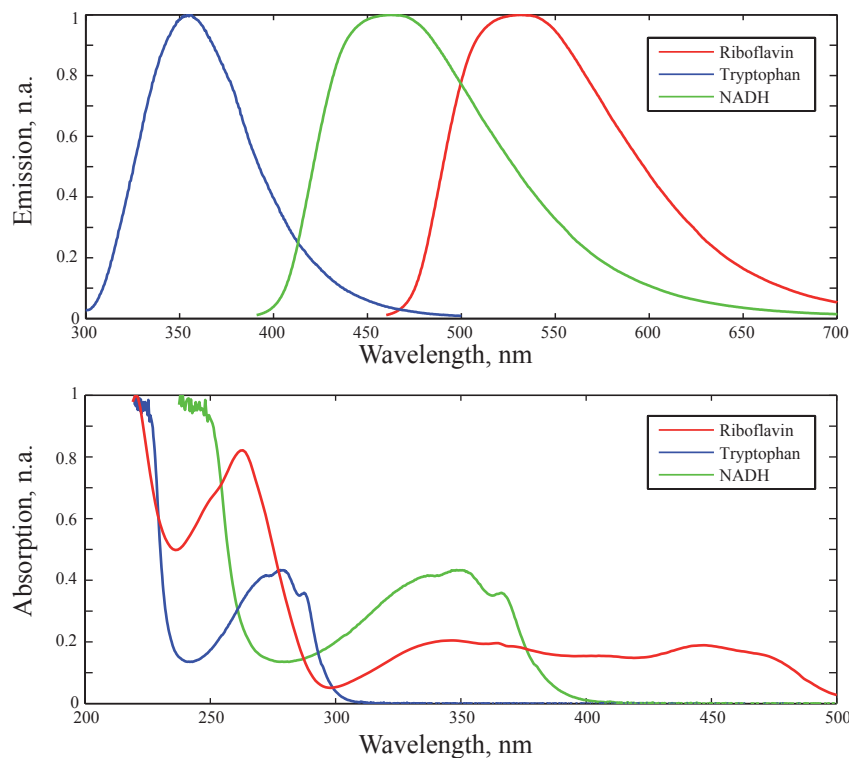
Figure 3.6: Example of the fluorophore emission and absorption
spectra in bioaerosols: riboflavin, NADH, tryptophan.

Figure 3.6 shows the typical absorption and emission spectra of these three fluorophore groups. Their absorption spectra overlap in the UV region $200 - 300$ nm, but differ for longer wavelengths. The emission spectra are well separated. In the case of Xe flash lamp- or UV laser-excitation at 266 nm, all of them will contribute to the total emitted fluorescence signal. For the femtosecond IR laser excitation, their contribution will vary as a function of the multi-photon absorption cross-sections (2 photon, and 3 photon mainly) and the laser intensity.

3.2.3   Experimental procedure

The purchased pollens were in dry form (see Sect. 1.8). They were put in suspension by the large particle generator (see Sect. 1.8). Between each sample type, the whole system was purged with clean dry air to avoid any contamination. For each detection event, which is initiated by coincidence of both scattering detection channels, the device triggers the Xenon lamp and sends the following data to the host computer:

- 64 intensity data points of scattering trace at 658 nm;

- 64 intensity data points of scattering trace at 780 nm;

- 32 intensity data points of fluorescence spectrum in the $295 - 570$ nm range;

- PMTs gain values and system time (with ms resolution).

An example of received data is given in Figure 3.7, which shows the output acquired for several sequential events.
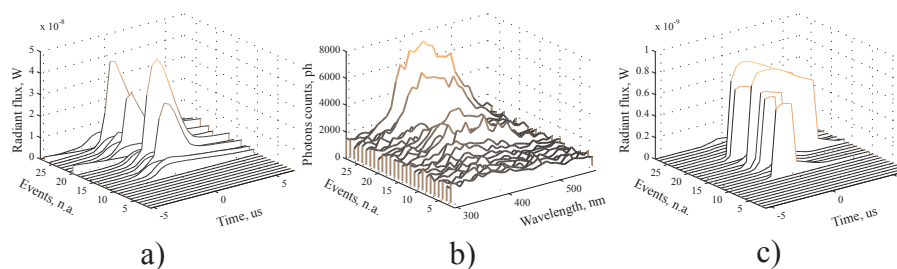
Figure 3.7: Example of raw data arrival a) 658 nm scattering channel; b) fluorescence spectra; c) 780 nm scattering channel.

Table 3.2 represents the event statistics of these measurements. A detection event is validated if it has both scattering traces non-saturated and fluorescence spectrum which is significantly above noise level. Valid spectra were selected by searching local maxima in a given spectral range. This range was defined from measurements with high signal levels and applied to the rest of the datasets.

Table 3.2: Pollen detection statistics

Parameter	*Mocus*	*Ambrosia*	*Carya pecan*
Total number of events	383	216	71
Number of retained events	237	294	30

3.2.4   Data analysis of scattered light measurements
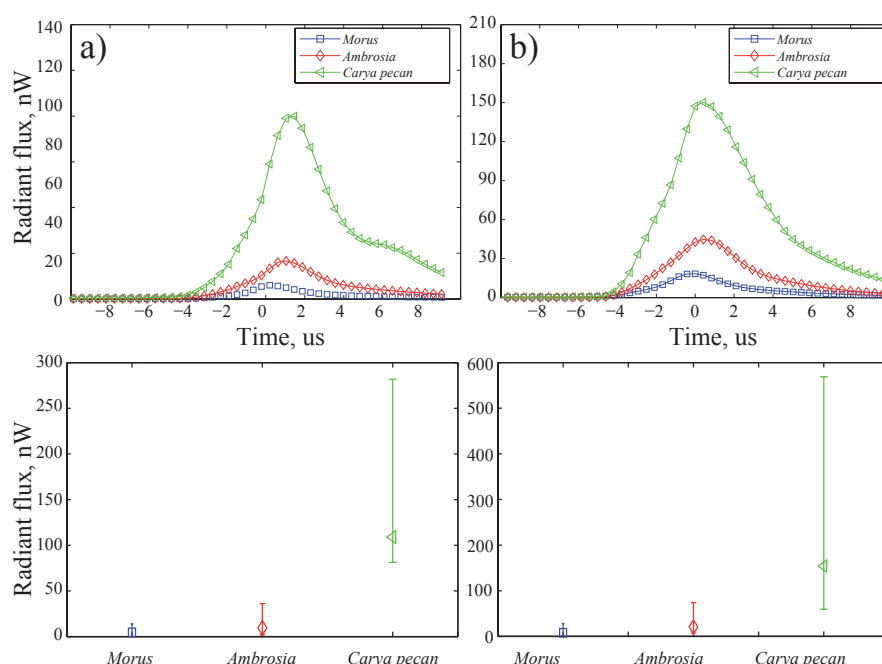
Figure 3.8: a) Mean scattering signals from $658\,\mathrm{nm}$ CW laser;
c) centres of mass for $658\,\mathrm{nm}$; b) mean scattering signals
from $780\,\mathrm{nm}$ CW laser; d) centres of mass for $780\,\mathrm{nm}$.
Error bars reports interval with 50% of events within it.

Like for the experiment with non-fluorescent particles, the amplitudes of scattering signals vary significantly and no direct size estimation can be performed without an additional statistical analysis. At the same time, the fluorescence response appears to be slightly different in the peak position and significantly higher in amplitude for *Morus* pollen. The data analysis starts with the evaluation of mean peak intensities and centres of mass of scattering signals. Figure 3.8a,b show the mean scattering signals for the three tested pollen grains at two laser wavelengths. Figure 3.8c, and (d) report the distribution centres of mass; the errorbars show the

intervals with 50% of evens within it.
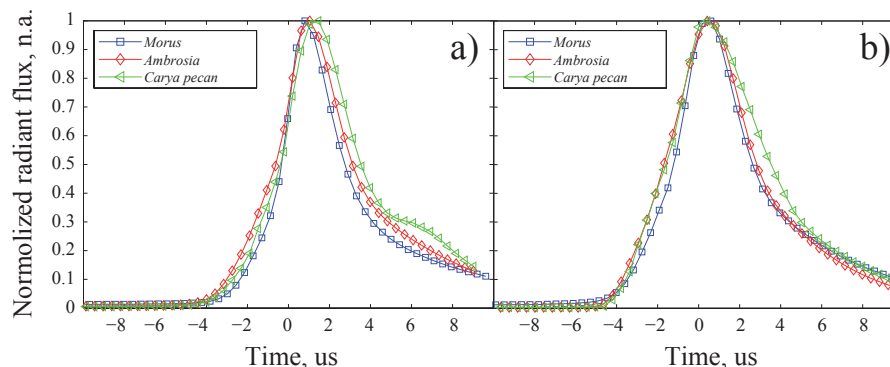
Figure 3.9: Normalized radiant flux: a) scattering signals from 658 nm CW laser; b) scattering signals from 780 nm CW laser

.

The signal duration was also evaluated to verify if any additional degree of discrimination can be extracted. Each scattering signal was normalized by its maxima and three curves of mean values were obtained (Fig. 3.9). The curves in panel (a) plots the show normalized scattering signal at 658 nm and those in panel (b) at 780 nm.

A similar behaviour as in the miscrospheres experiment (see Sect. 3.1) was observed. The signal duration was shorter than that one would expect from the CW laser beam longitudinal dimension. The scattering signals appeared to be very similar among the sample pollens. A small difference in the duration and shape was however observed, especially for the *Carya pecan*.

3.2.5 Comparison of scattering signals with non-fluorescent particles

We treated the scattering data obtained for pollens with the same statistical analysis applied to the non-fluorescent particles (see Sect. 3.1). First at all, we evaluated the signal distribution to verify if it presents the same tendency of increasing with particle size (Fig. 3.10a,b). These graphs indicate that, in general, the scattering distribution follows the mean sample size, however, for the 658 nm scattering channel, the signal for non-fluorescent microspheres appears to be weaker in general.

Another parameter to compare is signal duration. A remarkable difference was observed between the pollen samples and the microspheres: the pulse duration was
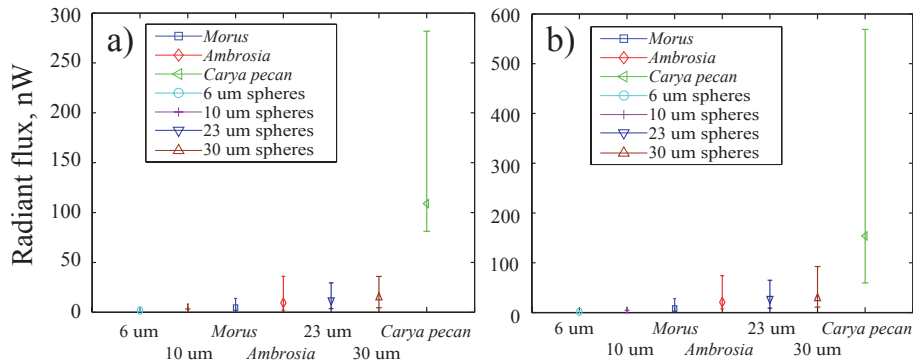
Figure 3.10: a) centres of masses as function of different samples
at 658 nm; b) centres of masses as function of different samples at 780 nm. Error bars reports interval with
50% of events within it.
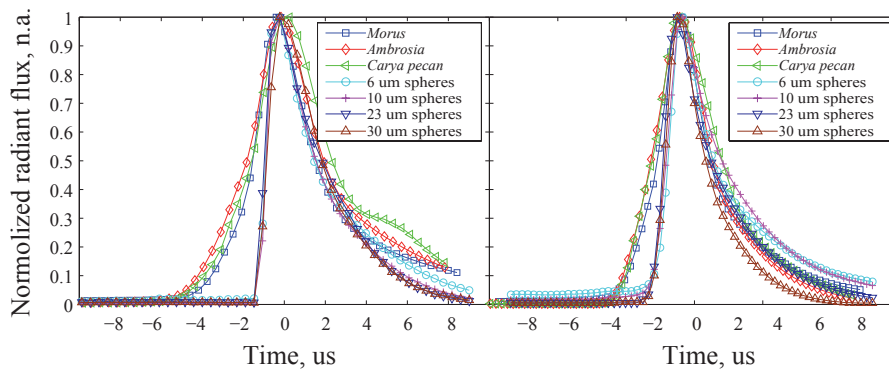
Figure 3.11: Normalized radiant flux: a) scattering signals from
658 nm CW laser; b) scattering signals from 780 nm
CW laser

shorter in the case of all microsphere samples as compared to the pollens. According to the explanation from Section 3.1, the signal duration is mostly defined by the variation of the double refraction angle while particles cross the laser beam. However, the particle surface quality and its shape affect the angular distribution of the scattering intensity, leading to a longer pulse duration and more symmetrical shape [83, 84, 76].

We did not perform any flow dynamics simulations on non-spherical particles, but from Section 2.1 it comes out that all spherical particle of comparable (to pollens) sizes have almost the same velocity at the nozzle outlet. If we now suppose that it is also the case for the pollen samples, the difference in pulse duration is entirely due to the different scattering patterns.

3.2.6   Data analysis for fluorescence detection

The first step in analysing spectral data is to experimentally determine the background noise level and subtract it from the acquired spectra. Unlike scattering, the background noise is mainly due to the insufficient filtering of the excitation lamp. It was determined before measuring each sample and computed as the mean signal over ten background spectra. The background-corrected version of fluorescence spectra of the three pollens are given in Figure 3.12.
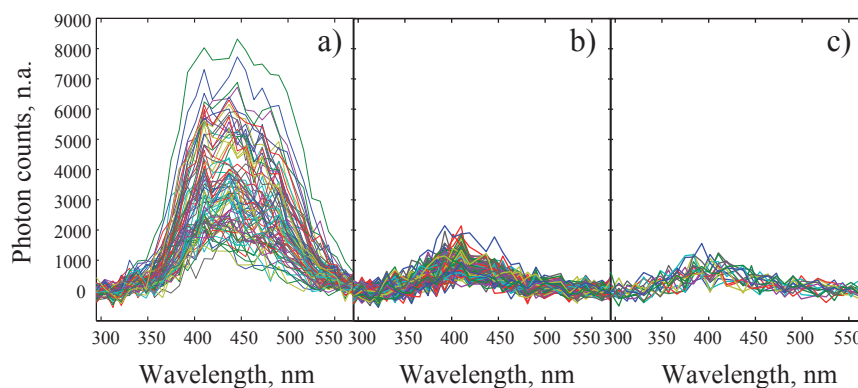
Figure 3.12: Corrected fluorescence spectra for three pollen species:
a) *Morus*; b) *Ambrosia*; c) *Carya pecan*

To determine the peak wavelength of the three ensembles of spectra associated to the different pollens, it is necessary to normalize their mean value. Figure 3.13 represents the best fits for the three species with the following analytical expression: $S(\lambda) = a\lambda e^{-\frac{(\lambda+b)^2}{2c^2}}$ where a, b, c are free parameters. Such analytical expression was chosen empirically because it accounts for the asymmetric tail of the curves at longer wavelengths yielding smaller standard quadratic deviation σ than simple Gaussian.

It can be seen that the peak wavelength (solid vertical lines) varies from pollen type to pollen type, and this opens, in principle, the way of discriminating among these samples by comparing their fluorescence responses. The spectral shift of about $6-7$ nm between *Carya Pecan* and *Ambrosia* is not significant since it is less than spectral resolution. The *Morus* sample yielded a fluorescence maximum $40-45$ nm away from the two other samples. Thus, a simple comparison between fluorescence spectra permits a reliable discrimination of one of the samples with respect to the others. Further statistical analysis is needed to distinguish between *Carya Pecan* and *Ambrosia* pollen grains.
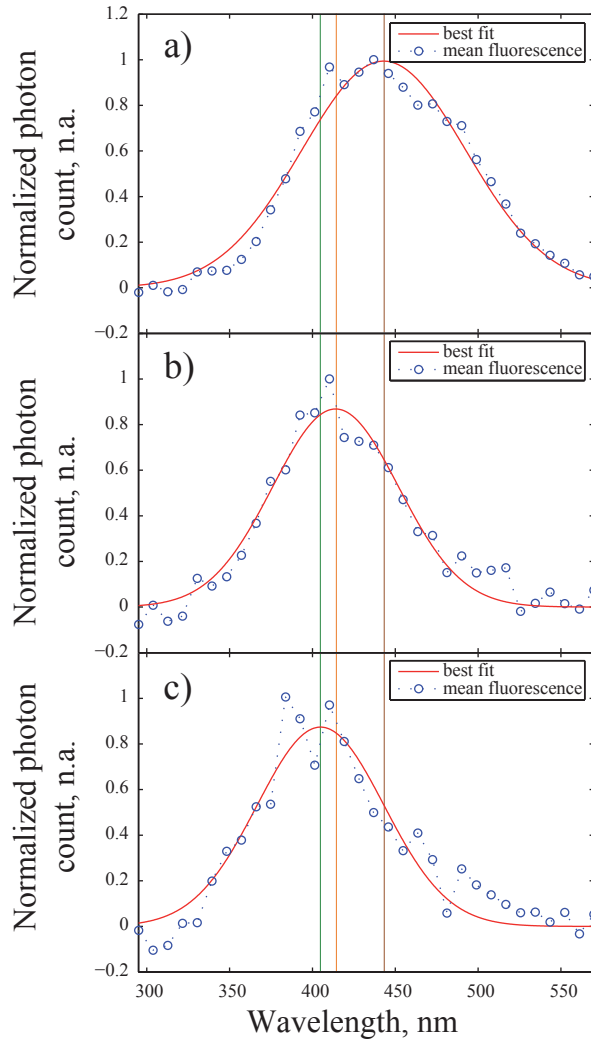
Figure 3.13: Fluorescence spectra for three pollen species: a) *Morus*; b) *Ambrosia*; c) *Carya pecan*. The fitting expression is $S(\lambda) = a\lambda e^{-\frac{(\lambda+b)^2}{2c^2}}$.

3.2.7 Principal component analysis

Principal component analysis (PCA) is a powerful mathematical tool generally employed to reduce the number of degrees of freedom in datasets [85]. This method treats each initial degree of freedom (in the case of this experiment each pixel of the 32-channel PMT) as an independent variable and defines a rectangular matrix containing these variables as colons and their different values as rows. Each dataset is normalized, so any proportional change from one dataset to another is disregarded. The input matrix is then used to calculate cross-correlation coeffi-

cients among all its elements resulting in a cross-correlation (or covariance) matrix. This matrix projects the whole dataset into a new space formed by its eigenvectors (also called principal components). The eigenvalues corresponding to these vectors reflect the relative importance of each dimension on the data covariance.

Figure 3.14 represents raw data projections on the first and second principal components obtained from the fluorescence spectra of the three pollens. It demonstrates that all data points are subdivided in groups and a clear difference can be made between *Morus* and the other two pollens. It is also interesting to notice that the second principal component does not bring any additional information (discrimination degree) as compared to the first principal component. As a consequence, only the first component is considered for the further analysis.
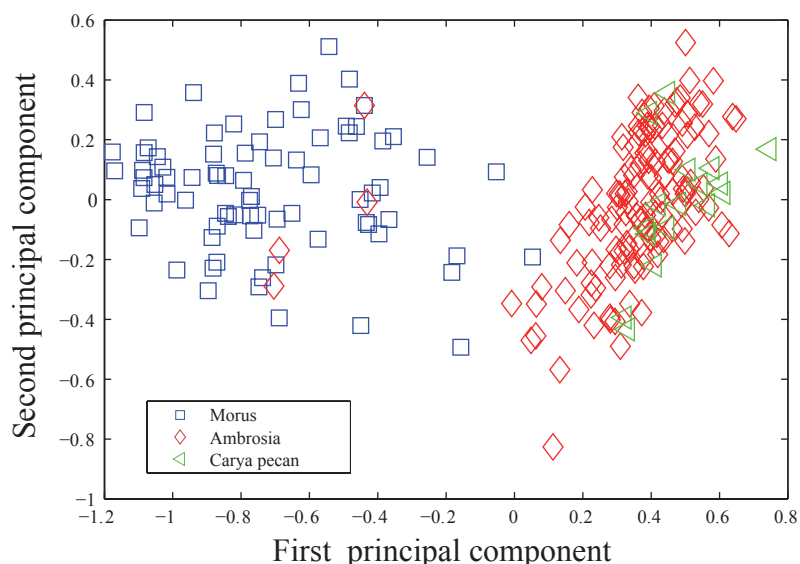
Figure 3.14: Spectral data representation in 2D space of the first two principal components.

If now one combines the first principal component and the scattering signal peak intensities, higher discrimination between different types of pollens can be achieved. This result is reported in Figure 3.15. A good separation between *Morus* and the other pollens is again observed.

More than that, an additional independent variable can be included into PCA. This new degree of freedom is the ratio between the scattering intensity maxima and the total photon counts in the mean fluorescence spectrum of a given sample. The result of this analysis is given in Figure 3.16. It is remarkable now that the distributions for all three samples are well separated. Only a few events overlap the distribution of other samples.
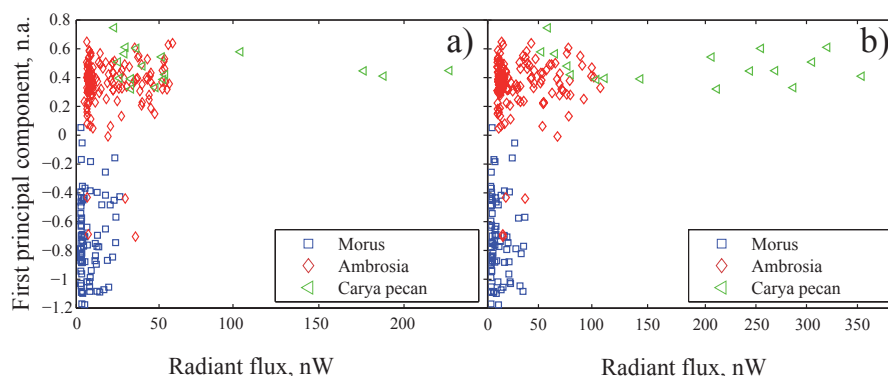
Figure 3.15: Data representation in 2D space of the first principal component versus scattering intensity: a) 658 nm; a) 780 nm.
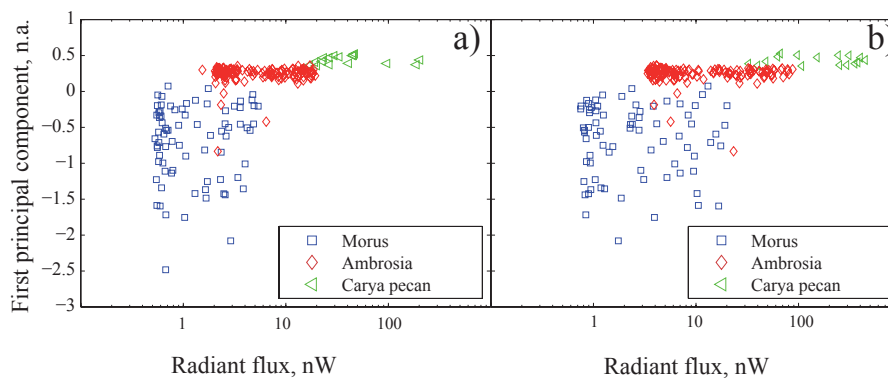
Figure 3.16: Data plus fluorescence on scattering ratio representation in 2D space of the first principal component versus scattering intensity: a) 658 nm; a) 780 nm.

Based on these statistics and supposing that the distributions over both axis are Gaussian, one can calculate the respective probabilities of detection for each pollen sample. It permits now to predict the pollen species for any detected particle with a known probability. The contour plot in Figure 3.17 indicates the regions corresponding to 66%, 95% and 99% of probability that a detected event lies within a given ensemble. If a particle is detected outside the three distributions, it will not belong to any of them with >99% probability.

3.2.8 Discussion

A detailed analysis of the scattering traces showed that their amplitudes had a large dynamical distribution and that it was impossible to estimate the particle size from a single detection event, as it was also the case in the experiment on non-fluorescent aerosols. However, it was also shown that with many accumu-
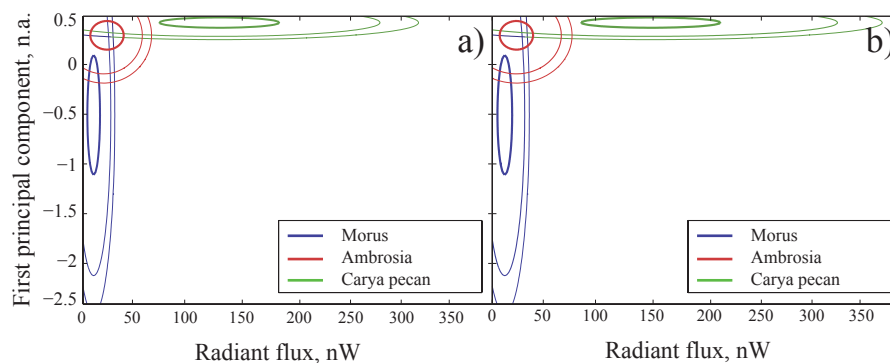
Figure 3.17: 2D probability distribution for three pollen species: blue - *Morus*; red - *Ambrosia*; green - *Carya pecan*. The circles contour zones with 66%, 95% and 99% of probability (1σ, 2σ, 3σ).

lated measurements, one is able to calculate a mean value of peak scattered radiant power, and these values were significantly different for each pollen species. Indeed, the scattering signals follow well the nominal particle size. In addition to this, direct comparison with results for the non-fluorescent particles demonstrated that the general tendency was respected and that bigger aerosols have higher scattering signal.

This especially can be seen from Figure 3.10 reporting the mean peak intensities and centres of masses for pollens and microspheres. Arranged by increasing size order, scattering signals augment also but in a non-linear way. This fact is in perfect agreement with Mie theory, which predicts a quadratic dependence for large microscopic particles. It is also confirmed by the scattering simulations in Section 2.4.

Another important aspect observed in the scattering measurements was related to the signal duration, which appeared to be slightly different among the different pollen species (Fig. 3.9) indicating that, according to Section 3.1, the particle size and shape contributes to the observed signal duration. It was also interesting to notice that, when compared to microspheres (Fig. 3.11), the pollen samples had a longer signal duration regardless the particle size.

This fact was explained by the difference in shape and surface quality between microspheres and pollens samples. Next chapter will present multi-photon microscopy images of the pollen samples in which the shape and surface roughness can be directly observed (Fig. 3.18). The time resolved acquisition of the scattering signals appears to be a potential addition degree of particle identification.

However, we only demonstrated here a qualitative difference and did not use this parameter for further particle discrimination.

The analysis of spectral data revealed that all pollen samples had a significant fluorescence response when exposed to UV light. The resolved fluorescence spectra of single pollens excited by the Xe flash lamp were detected on the fly and in real-time. This represents an important technical advancement in view of an eventual device commercialization.

The first look on the fluorescence spectra raw data (Fig.3.12) reveals that *Morus* has different peak wavelength emission than the other two species. *Morus* pollen has also the smallest size among the tested species but it showed the highest emission intensity. This property can be investigated in the future on single trapped pollens or by means of fluorescence microscopy, but even without knowing the exact source of this difference in fluorescence emission, it can be used as an additional degree of discrimination.

The statistical analysis of the detected spectra showed that for each ensemble of samples, they all are centred on slightly different wavelengths. In particular, this shift is clearly seen in Figure 3.13, which also shows the best fitting curves. Once again, *Morus* pollen showed higher difference in the central wavelength than *Ambrosia* and *Carya pecan*. This can be a direct consequence of different fluorophore molecules concentrations because each of them contributes with its particular fluorescence signature to the whole signal. It should be underlined here that measuring the fluorescence signal resolved over 32 channels permitted to see this small differences in central wavelength, which will not be the case for commercially available devices or research set-ups [42, 18, 86] that employ one or two channels to detect the fluorescence.

To increase the discrimination power of the detector, PCA was applied. Figure 3.14 showed the data for the three pollen species projected into the 2D space of the first and second principal components. It is evident that once again *Morus* data formed a well identifiable group separated from the other samples, which are overlapped completely. The PCA method allows to reduce the number of degrees of freedom, in this case number of pixel in the spectrometer, without loosing precious information on fluorescence spectra. It also permits the definition of a new space based on eigenvector of the covariance matrix, and every new detected event can then be projected into this space and give the probability of belonging to a specific pollen species. In this sense, PCA appears to be a powerful statistical tool for the future experiments on a larger number of species where the overlaps will probably be more significant among all the samples.

Coupling the PCA analysis with the scattering maxima (Fig. 3.15) decreases the overlap between the *Ambrosia* and *Carya pecan* data distribution. However, on the graphs corresponding to the two scattering wavelengths, there are still some outliers. Adding to the PCA analysis an additional degree of freedom by taking into account the emitted fluorescence divided by the scattering maxima, allows to further increase the separation among the distributions. This procedure was reported in Figure 3.16. It is important to notice that zones of 66% probability (Fig. 3.17) are not overlapped so relatively high accuracy was achieved in this experiment.

This experiment confirms that given the scattering intensities and spectrally resolved fluorescence, treated by the PCA analysis, allows satisfactory discrimination among the three selected pollen species [87]. The exposed method demonstrated that a cost-effective and reliable excitation source like a Xe flash can be employed instead of a UV pulsed laser. As a consequence, the developed system shows the advantages of the other spectrally resolved detectors [61, 45] and it is transportable and ready for in-field measurements like the other lamp based detectors [18, 19].

3.3 Individual aerosol discrimination by multi-photon excited fluorescence

3.3.1 Introduction

The previous experiment on pollens has shown that species can be discriminated one from another by simultaneous detection of scattered light and linear fluorescence signals. Despite the fact that the results were rather successful, it is evident that some new techniques with higher discrimination power are needed. The experiment described [32] in this section is intended to investigate whether non-linear multi-photon excited fluorescence (MPEF) can bring new means for identification. Moreover, recent developments in ultra-short laser science employing non-linear interactions [34, 88] with molecular dynamics permit the discrimination between structurally and spectroscopically quasi-identical biomolecules. On the other hand, simple pump-probe approach appears to be very efficient in identification biological and non-biological aerosols [89]. Some other methods like coherent anti-Stokes Raman scattering (CARS) have also demonstrated to be very powerful and make use of non-linear interaction with light [90]. These successful demonstrations supported the idea to coupling the developed aerosol detector with an amplified femtosecond laser system. The synchronization and stability aspect were already described (see Sect. 2.6) and showed that the yield of such experiment for the moment is limited due to major laser intensity fluctuations.

3.3.2 Microscopy study of samples

The pollen grains were first imaged by two-photon microscopy (Nikon A1R-MP) using a femtosecond laser as excitation at 700 nm. The laser peak intensity in the focus is of the order of 10^{12} W/cm^2. The excited multi-photon fluorescence was detected in backward direction and resolved in four spectral bands.

In Figure 3.18, each image is composed of four colors (blue, green, orange, red) representing four detection channels: UV (390 nm , FWHM 12 nm); Blue (485 nm, FWHM 20 nm); Green (531 nm, FWHM 40 nm), and Red (600 nm, FWHM 70 nm). Three-dimensional images are re-constructed from z-stack images taken with 1 μm step. They clearly demonstrate the presence of a two-photon fluorescence response from all the samples. However, these pictures can not provide any information on a potential contribution of the three-photon excitation, because the detection channels are all centred on wavelengths longer than the second harmonic of the excitation laser. Thus, all detected fluorescence can be attributed exclusively to two-photon excitation.
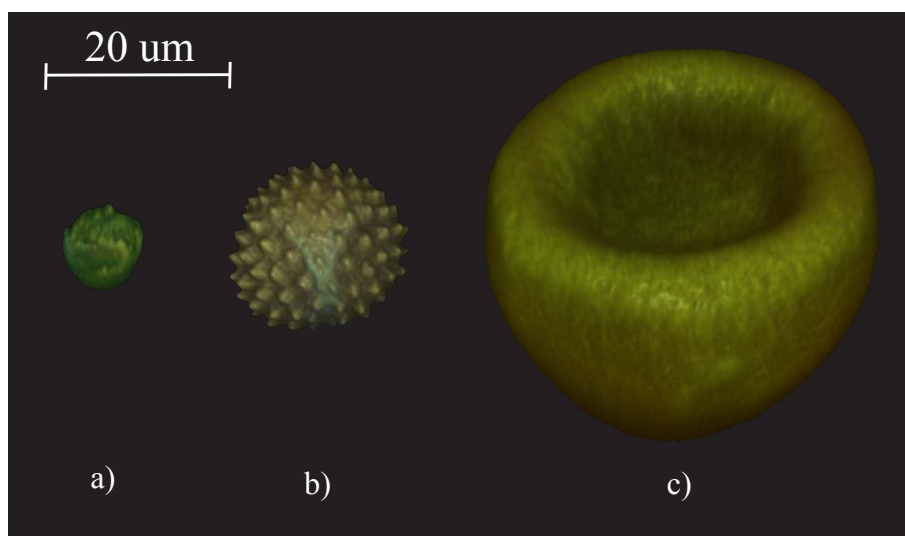
Figure 3.18: Multi-photon microscopy images: a) *Morus*, b) *Ambrosia*, c) *Carya pecan* The color intensities were adjusted quantitative comparison.

To verify if three-photon absorption from amino-acids contributes also to the fluorescence signal, some additional changes were made on the detection channels. The laser wavelength was set at 800 nm. The UV detection filter was replaced by one centred at 360 nm, FWHM 12 nm. All detection channels were adjusted to have the same gain and sensitivity. Finally, a sample of reference microspheres FB345 was imaged as they fluoresce at 345 nm. The results of this experiment are

reported in Figure 3.19. The insets show the superposition of all detection channels while the main images present the UV channel only. It can be clearly seen that the FB345 microspheres have important emission in the UV region and that they are excited by three-photon. At the same time, only the *Ambrosia* pollen exhibits very weak but detectable emission in this region. It can thus be concluded at this stage that this pollen will probably have a fluorescence spectrum shifted towards shorter wavelengths as compared to the other pollens if excited with similar laser intensities. The contribution of three-photon absorption will certainly increase with the laser peak power as this process is proportional to the third power of laser intensity.

According to the short overview of the fluorephore molecules contained in the pollens (see Sect. 3.2), the results of these measurements indicate that the *Ambrosia* pollen has a slightly higher contribution of the amino-acids to the fluorescence signal than the other sample pollens. This can be direct a consequence of the different relative concentration of these molecules as compared to the NADH and flavins.
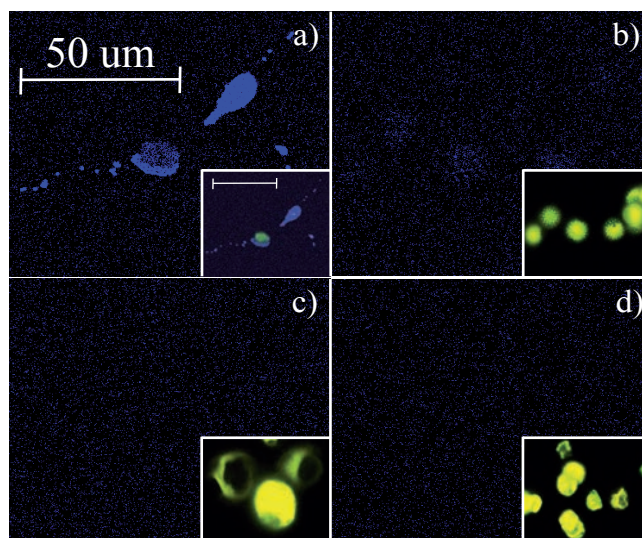
Figure 3.19: Microscopy images, UV channel versus all superposed channels: a) FB345 microspheres, b) *Morus*, c) *Ambrosia*, d) *Carya pecan*.

3.3.3 Experimental

The experiment consisted in sampling air containing the aerosol samples, scattering detection and excitation and collection of the non-linear fluorescence. Four types of particles were used: three pollens (*Morus*, *Ambrosia* and *Carya Pecan*) and the reference particles FluoresceBright FB345 from Polysciences Inc. They

were used in aggregated form as the size of a single microsphere ($1~\mu m$) was out of our detection range. To generate the aggregates, the microspheres were solved in ethanol and then dried on metal surface. The aerosols were afterwards generated by the large particle generator (see Sect. 1.8). For the reasons of low yield due to the femtosecond laser stability in the external triggering mode (see Sect. 2.6), the scattering detection PMTs were set on very high gain to have as maximum coincidence events as possible. A direct consequence of this is that most of the scattering traces were saturated and could not be used for the data analysis. So the experiment was particularly focused on fluorescence detection and its behaviour when excited by two- or three- infra-red photons. In this work, the chirped pulse amplified system delivered single pulses of $60 - 100~\mathrm{fs}$ duration and $1~\mathrm{mJ}$ energy (see Annexe 8). In the focal spot, the laser beam peak intensity reached $10^{13}~\mathrm{W/cm^2}$.

3.3.4 Results

Figure 3.20 shows the multi-photon excited fluorescence spectra of different pollens and FB345 (red) together with the fluorescence background level (blue). The dashed lines indicate the 95% confidence interval ($\pm 2\sigma$).
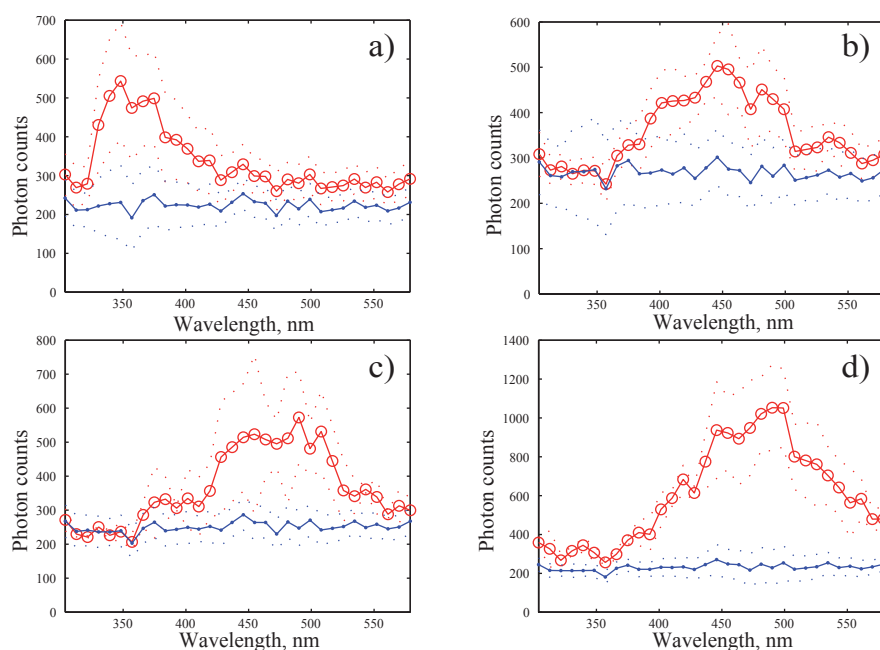
Figure 3.20: Single-shot MPEF spectra of individual aerosol particles. a) Simulants of bacteria aggregates (FB345); b) *Ambrosia* pollen; c) *Carya Pecan* Pollen; and d) *Morus* pollen. The dashed lines represent the 96% confidence interval ($\pm 2\sigma$) calculated from a series of individual detection events.

Table 3.3 reports on the total number of detected events among which only less than 10% gave significant spectral signals and were retained for analysis. The wavelength corresponding to the emission peak is also reported, determined from the position pixel that detected maximum intensity. Thus, this estimation is accurate within ± 8 nm. The photon count was obtained from the mean value at peak emission wavelength, and its standard deviation resulted from the same statistics.

Table 3.3: Detection statistics

Sample	Scattering events	Emission peak, nm	Photon count for peak wavelength	Standard deviation
FB345	1248	350	543	75
Morus	1285	490	1052	110
Ambrosia	712	445	503	35
Carya Pecan	400	490	572	61

The vertical axis of Figure 3.20 is given in photon counts, which is estimated from the measured electric charges on each channel of the 32 PMT array. These values are not corrected by the optical response of filters, grating, optical windows and objective, and also differences in optical response from pixel to pixel.

3.3.5   Discussion

The measured data clearly demonstrated the detection capability of MPEF for pollen samples and FB345 particles. Comparing with the previously presented Microscopy images illustrates similar tendency in the spectra behaviour. While FB345 exhibits only 3PEF as its fluorescence spectra is almost completely in shorter wavelengths than 400 nm, the pollens demonstrate a superposition of 2PEF and 3PEF because the spectra slightly cross 400 nm. It becomes evident that photons in the range of $350 - 400$ nm mostly resulted from 3PEF. These photons were observed for all three samples, however, like in case of Microscopy images, the *Ambrosia* spectrum is more shifted in the UV region. The two other pollens exhibit a broad maximum around 480 nm, similar to the characteristic emission of NADH [91].

Direct comparison with recent works on dual-wavelength excitation [31, 44] are in agreement with the obtained results. It was indeed observed in that experiments that when excited at 354 nm pollen spectra are red-shifted (especially *Ambrosia*) with respect to 266 nm excitation. It appears thus that our spectra are a composite of the spectra observed with dual excitation schemes, i.e. a combination of 2PEF and 3PEF in pollens.

A significant improvement of our set-up in terms of sensitivity would be the excitation of the particles through the same objective as for the fluorescence collection, like in epi-microscopy. MPEF from individual aerosol particles is indeed strongly enhanced in the backward direction [92, 93] (up to a factor 10 for 3PEF). The important anti-Stokes shift between the 790 nm excitation and MPEF would allow efficient rejection at the dichroic beamsplitter.

The presented work provided unique occasion to make 1PEF and MPEF experiments on the same device and with the same detection conditions. Figure 3.21 represents the superposition of the linear and non-linear fluorescence spectra for each pollen sample. It was observed that each sample exhibits a red-shift in its MPEF spectrum when excited at 800 nm.

It can be understood from the excitation mechanism and the absorption curves of bio-fluorophores presented in Section 3.2. Flavins have an important absorption around 400 nm while NADH and amino-acids have their absorption bands at shorter wavelengths. At the same time, 2PEF absorption cross sections are much higher than 3PEF [91]. So, the flavins contribute significantly to the fluorescence signal for low laser intensities, and as the intensity increases, NADH and amino-acids will shift the fluorescence spectra to shorter wavelengths as 3PEF implies a third-power dependent on the intensity.

Another interesting fact is that, according to the best fitting curves, the shift between 1PEF and MPEF spectra was not equal from one species to another. It was observed that this shift increases with decreasing of the particle size. Of course, given only three pollen species, it is difficult to draw conclusions. However, a supposition can be made that the red-shift between MPEF and 1PEF increases because of the light absorption inside the pollen grains. But it is also possible that there is an important difference in the fluorophore distribution inside the pollens that makes the red-shift changing.

Finally, *Ambrosia* and *Carya Pecan* pollens had almost identical 1PEF spectra and only applying of PCA post-treatment allowed discrimination between them. In the case of MPEF, these species are clearly separated in spectra as their emissions are not centred on the same wavelengths. If one performs sequentially 1PEF and MPEF measurement on the same pollen grain on the fly, it can be expected that a complete discrimination by fluorescence can be achieved.

Linear and non-linear spectroscopy on single aerosol particles presented in this part of the manuscript, demonstrated some limitations in the discrimination power. MPEF and 1PEF cannot be reliable criteria of particle identification without being complemented by the scattering measurement, which could not provide (in our case) an accurate estimation of the individual particle size. More sophisticated
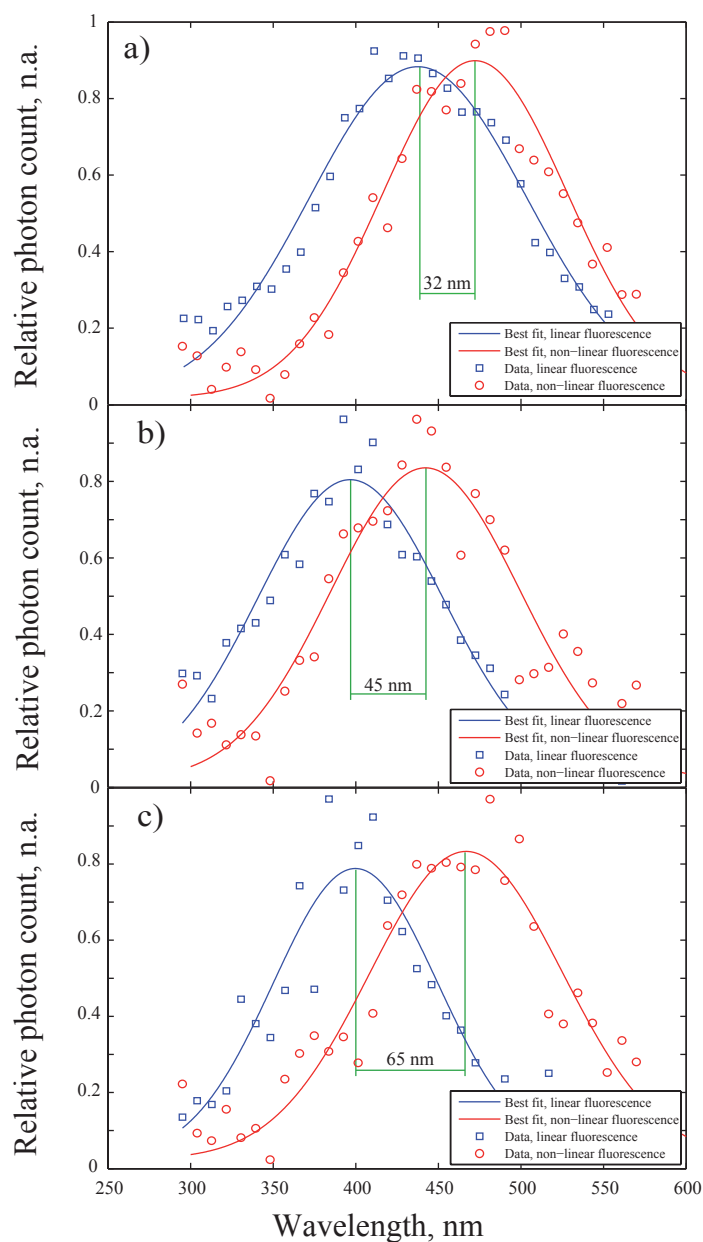
Figure 3.21: Superpostion of 1PEF and MPEF spectra: a) *Morus*;
b) *Ambrosia*; c) *Carya Pecan*.

and complex methods, like pump-probe [89] and Optimal Dynamic Discrimination (ODD) [33, 34, 35], should be involved to increase the discrimination power of the UV spectroscopy, but this needs optical devices capable of manipulating the spectral phase and amplitude of ultrashort UV pulses. That is why we performed a development of such a device described in the next part of the manuscript.

Part II

Broad bandwidth laser pulse shaping

4.1 Introduction

During the last decade, numerous applications of coherent control on molecules have been reported, either based on close-loop [94] or open-loop [28] schemes. One of the long-term ambitions is to efficiently control the dynamics of biologically relevant molecules via phase-sensitive schemes. Some first promising results have already appeared [28, 95, 96, 33, 97].

The core optical technology to apply coherent control scheme is temporal shaping of femtosecond pulses [98, 99]. So far, one of the principal limitation of this approach has been the fact that most of the absorption bands of biomolecules lie in the UV, a spectral region hardly accessible by transmissive devices, like liquid crystals shapers. Some alternative techniques have arisen: as indirect shaping [100], or based on the recent technological advances in transmissive spatial modulators [101, 102, 103, 104]. Shaping devices can be classified in following subgroups [99]:

- fixed phase and amplitude masks;

- liquid crystal light modulators [104];

- movable and deformable mirrors [103, 38, 105, 106];

- holographic masks [107];

- acousto-optic and electro-optic devices [98, 108].

The following chapter describes a new technology based micro-mechanical electric systems (MEMS) developed in collaboration with École Polytechnique Fédérale de Lausanne (EPFL) dedicated to the temporal pulse shaping. This reflective approach permits to overcome limitations of bandwidth, generally associated to the transmissive devices. The first essays of MEMS devices for the pulse shaping in the IR, VIS, UV and XUV region will be reported.

4.2 Micro-mirror electrical systems

4.2.1 1D micro-mirror array for light shaping

A 1D micro-mirror array dedicated to pulse shaping was especially developed in collaboration EPFL/STI/IMT-NE/SAMLAB [38]. This device is an electrostatic device (Fig. 4.22) composed of an array of independent mirrors. This PhD work will describe experiments that were performed with two different geometries:

- 160 μm wide x 1 mm long, 3 μm gaps tilt-piston mirrors, 1D array of 100 mirrors;

- 120 μm wide x 1 mm long, 3 μm gaps piston-only mirrors, 1D array of 100 mirrors.

Each mirror in the array (Fig. 4.22) is composed by the:

a) X-shape springs (only for tilt-piston mirrors);

b) triangular height adapter;

c) tilt actuator (only for tilt-piston mirrors);

d) piston actuator;

e) micro-mirror;

f) main bar.

The extreme points of X-shaped springs are fixed to the chip substrate. When a voltage is applied to the tilt or/and piston actuators, an electrostatic force appears and moves or/and tilts the mirror. This force is balanced by the torque force of the springs, so the mirror maintains a stable position while voltage is applied. The response time is defined by the spring elasticity and actuator efficiency. For the proposed design, it was calculated from numerical simulations to be less than 1 ms.
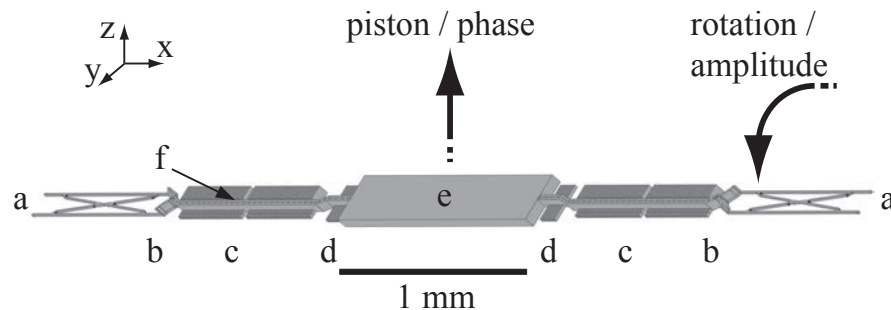
Figure 4.22: Geometry of a single mirror element: X-shaped springs (a), triangular height adapter (b), tilt (c) and piston (d) actuators, and high aspect-ratio mirror (e), main bar (f).

Figure 4.23a shows a scanning electron microscope (SEM) picture of of tilt-only mirror array with wirebond connections. These connections provide high voltages to the actuators on each single mirror. Figure 4.23b is a white light interferometry picture showing a parabolic mask applied on the whole array. The maximum stroke in this example is about 1 μm that corresponds to a phase shift of 10π at 400 nm wavelength. It can also be seen from the example that some mirrors are missing

or stuck on the bottom. This is due to short circuits or incomplete release of these mirrors during the lithography manufacturing process.
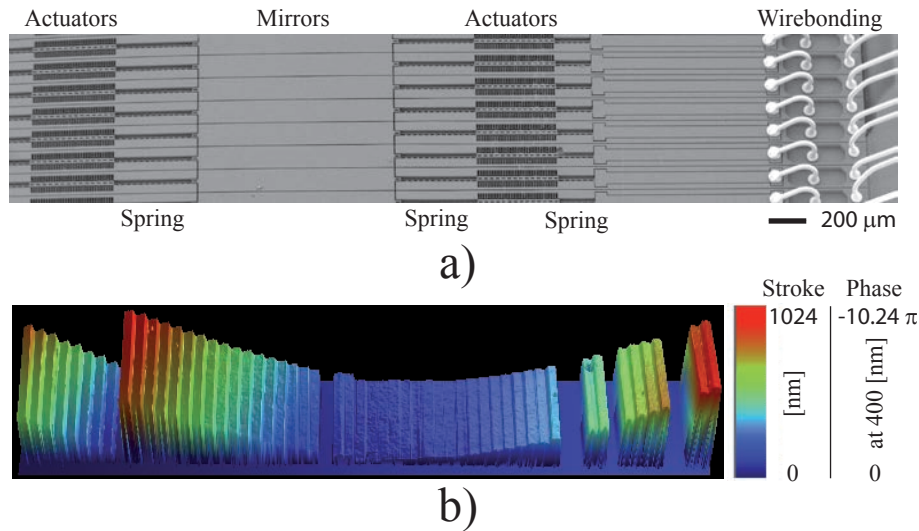
Figure 4.23: a) Scanning electron microscope (SEM) image of the mirror array; b) White-light interferometry image of a set of actuated mirrors in a parabolic configuration.

Figure 4.24 shows an example of independent actuation of single tilt-piston mirrors. It can be seen that mirror 99 is on the bottom level, mirrors 97, 95, 94 have a stroke displacement, mirrors 98, 96 are titled, and mirror 100 is tilted and shifted simultaneously.
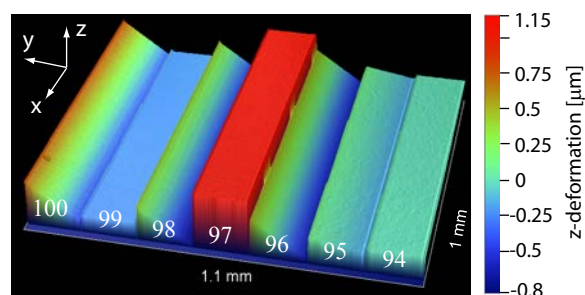
Figure 4.24: Selective actuation of a tilt-piston device.

The developed devices (tilt-piston and piston-only) were coated with a thin Al layer. They have very high surface quality, less than $20\,\mathrm{nm}$ peak-to-valley distance that corresponds to $\lambda/20$ at $400\,\mathrm{nm}$ wavelength. The maximum tested stroke was

about 3 μm. The flatness of the whole array (deviation in Z-direction between single mirrors) is about 1 μm and can be compensated by individual mirror actuation.

4.2.2 Electrical driver for micro-mirror array

A dedicated driving electronics (Fig. 4.25) was designed to supply high voltages on the actuators of each individual mirror. The system is controlled by a FPGA chip Spartan-6 LX16 from Xilinx Corp., which receives user commands via USB 2.0 port based on FT2232H chip from FTDI Corp. The commands are interpreted and the necessary signal sequences are generated and sent to 8 digital-to-analogue converters (DAC) AD5535 from Analog Devices. These integrated circuits (IC) convert input data into voltage with 14-bit resolution and 200 V of maximum output. Each DAC has 32 high voltage outputs, so 8 ICs can address 256 channels. The MEMS tilt-piston mirrors need two independent high voltages per mirror that leads to a total of 200 channels.

| USB interface FT2232H | FPGA Spartan 6 LX16 | 8 x DAC AD5535 | Socket with MEMS device |
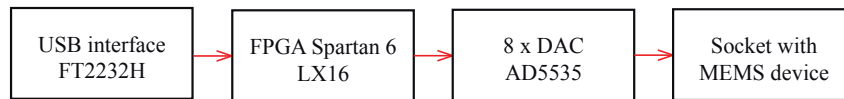
Figure 4.25: Schematics of the driving electronics architecture.

Two different versions were designed: the first one (Fig. 4.26) dedicated to standard applications at atmospheric pressure; the second one (Fig. 4.27) suited for working in vacuum (down to 10^-6 mBar) environment.

The experiments in IR and VIS regions described in the following text were done with the first version of the driver. For the XUV experiments described in chap.8, the same driver but with wire-to-wire vacuum feed-through connections was used. The vacuum compatible version will be realized in the future.

4.3 Temporal pulse shaping in UV-VIS and IR

4.3.1 Background concepts

The ultrashort laser temporal pulse shaping is the process of generation of arbitrary time and/or frequency shapes from laser pulses. It can be described within Linear Response theory using a Fourier formalism. If we consider the electric field of the input pulse in the frequency space, $E_{in}(\omega)$, the result of its passage through the pulse shaper, $E_{out}(\omega)$, is given by:

$$E_{out}(\omega) = E_{in}(\omega)H(\omega) \tag{4.2}$$
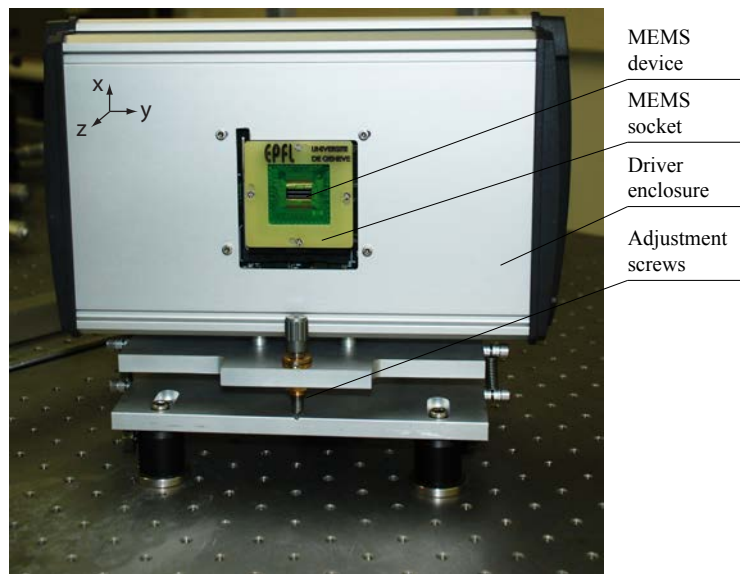
Figure 4.26: Driving electronics installed in the opto-mechanical support: basic version.
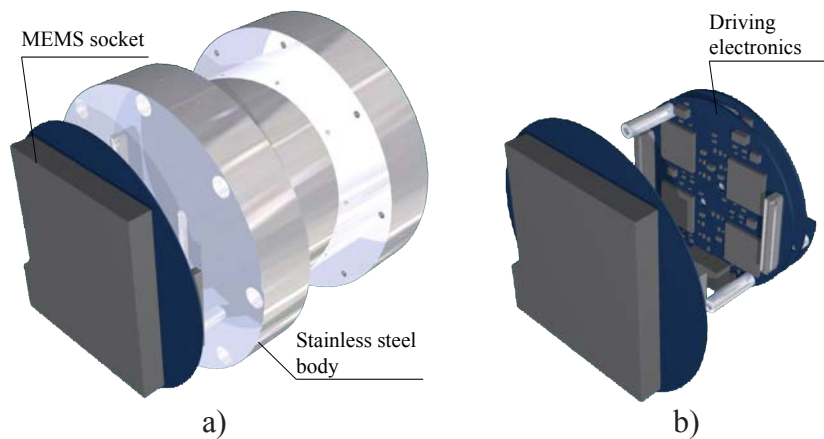
Figure 4.27: Driving electronics, vacuum version: a) view from outside; b) view from inside.

$H(\omega) = R(\omega)e^{i\Psi(\omega)}$ is the transfer function of the pulse shaping device, n.a.

This expression shows that laser pulse amplitude and phase can be modified independently in Fourier space by the $R(\omega)$ and $\Psi(\omega)$ response functions, respectively. Depending on application, the pulse shaper will need to modify only the phase, the amplitude or both.

4.3.2 Reflective shaper geometry

As sketched in Figure 4.28a, the different spectral components within the input pulse bandwidth, are first angularly dispersed by a diffraction grating. A cylindrical lens at the focal distance f from the grating is then used for collimating the diffracted beam and focusing each spectral component onto the Fourier plane, which corresponds to the position of the reflective MEMS surface. When the mirrors are not actuated, the set-up acts as a zero-dispersion 4-f compressor: the back reflected spectral components recombined after the second passage on the grating, interfere to produce an output pulse spectrally and temporally identical to the input one. When the shaper mirrors are offset from the Fourier plane (Fig. 4.28b), an arbitrary phase-pattern (Ψ) is imposed on the output beam through the relation $\Delta\Psi = \frac{4\pi}{\lambda}\Delta Z$, while the initial spectral amplitude is preserved. For instance, a parabolic phase function induces a temporal chirp on the outgoing beam. If some mirrors are tilted by a fixed angle around an axis perpendicular to the dispersion plane (Fig. 4.28c), two separate parallel beams emerge from the set-up: one made up by the spectral components associated to the deflected (D) mirrors, and one by the complementary ones, reflected by the undeflected (U) mirror elements. Phase modulations can be independently added to these two beams by simultaneously translating and tilting the mirrors (Fig. 4.28d).

The relationship between the geometrical pattern on the mirror array mask and the phase function $\Psi(\omega)$ is given by:

$$\frac{d\Psi(\omega)}{d\omega} = \frac{4\pi}{\lambda} \cdot \frac{dZ(\omega)}{d\omega} \tag{4.3}$$

where $\Psi(\omega)$ is the spectral component phase, rad;

          Z is the pixel coordinate relative to the initial position (flat mask), m.

The phase function is usually expressed in terms of its Taylor series:

$$\Psi(\omega) = \frac{4\pi}{\lambda} \cdot (a_0 + a_1\omega + a_2\omega^2 + ...) \tag{4.4}$$

The output electric field is calculated by inverse Fourier transform:

$$E(t) = \frac{1}{2\pi} \int_{-\infty}^{+\infty} E_{in}(\omega)e^{i\Psi(\omega)}e^{-i\omega t}d\omega \tag{4.5}$$

Evaluating this expression [109] indicates that a linear phase displacement induces a time delay, a parabolic phase function leads to the temporal chirp. The effect of the chirp can be calculated as:

$$\tau^2 = \tau_0^2 + \left[\frac{d^2\phi(\omega)}{d\omega^2}\right]^2 \omega^2 \tag{4.6}$$
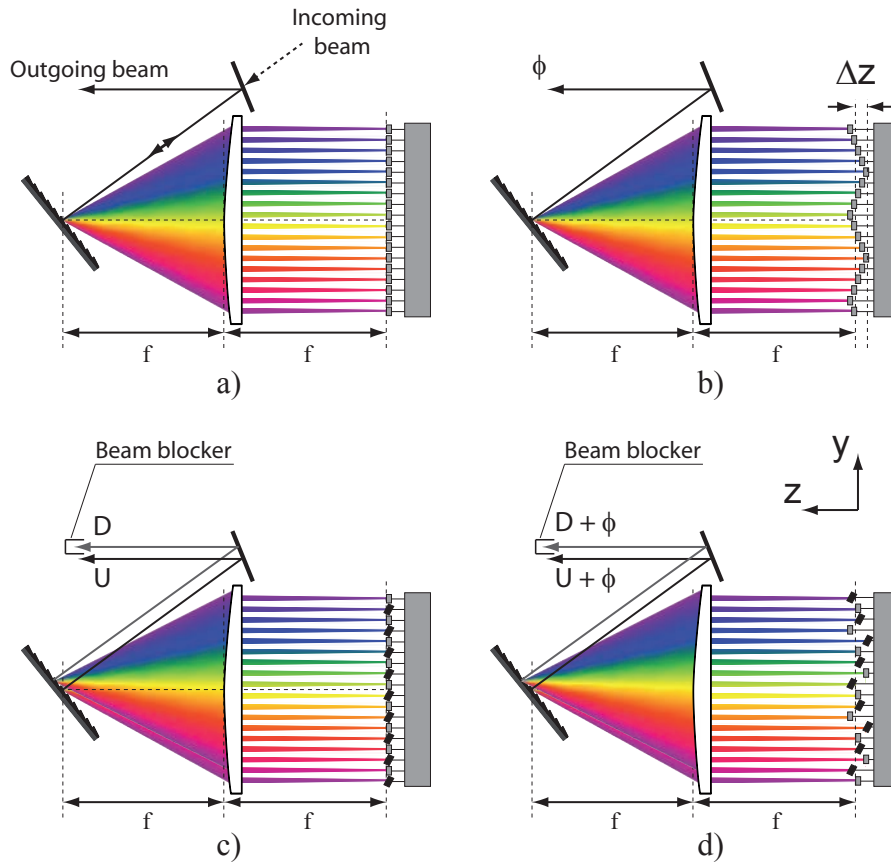
Figure 4.28: 2F geometry shaper with movable mirror array: a) flat phase mask, no amplitude modification; b) arbitrary phase mask, no amplitude modification; c) flat phase mask, with amplitude modification; d) arbitrary phase mask, with amplitude modification.

where τ^2 is the square of pulse duration for chirped pulse, s;

τ_0^2 is the square of pulse duration for unchirped pulse, s;

$\frac{d^2\phi(\omega)}{d\omega^2} = \frac{8\pi a_2}{\lambda}$ is the chirp coefficient resulted from Taylor expansion of the phase of the output electric field $\phi(\omega)$ around central laser wavelength ω_l, s^2.

4.3.3 Experimental

To demonstrate the capabilities of the MEMS based 1D mirror arrays developed during this PhD work, a dedicated experimental set-up was prepared (Fig. 4.29). A femtosecond laser oscillator FemtoSource Synergy-20 from Femtolasers Co. was employed for the experiments with pulses at $800\,\mathrm{nm}$ and $400\,\mathrm{nm}$. This laser delivers $18\,\mathrm{fs}$ pulses at $80\,\mathrm{MHz}$ repetition rate with $58\,\mathrm{nm}$ bandwidth (FWHM). The

output beam was split 50/50 just after the laser.
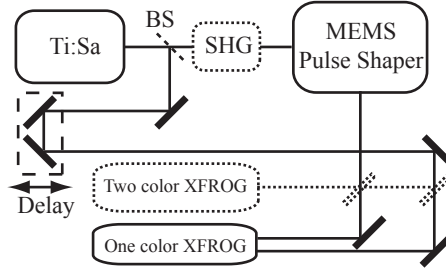
Figure 4.29: Experimental.

For the experiment at 800 nm, the first beam passed through the shaper. The dispersion element, in this case diffraction grating (groove density 600 lines/mm), was chosen so that the dimension of the spectrum in the Fourier plane fits well the MEMS device when used with a cylindrical lens (f $= 150$ mm). The dispersion, focusing and MEMS orientation was aligned in the horizontal plane. However, an additional cylindrical focusing lens can also be installed if the laser beam size is higher than transversal dimension of the MEMS mirrors. For this experiment, a f $= 60$ mm lens was employed. One could also use one spherical focusing lens instead of two cylindrical, but this makes the alignment harder. For the experiment at 400 nm, the first beam is doubled in frequency with a 500 µm thick BBO crystal before been injected into the shaper. A 1200 lines/mm diffraction grating is then used to disperse the spectral components.

The shaped and delayed beams are then recombined and the result is analysed. The spatial characterization of the shaped beam is realized by a Newport LBP-1 profiler. The spectra at 400 nm are acquired by an in-line CCD array (Thorlabs LC1-USB) placed at the imaging output port of a spectrometer (Princeton Instruments, Acton, SP2300i). Cross FROG (XFROG) traces [110, 111] are realized by frequency mixing the shaped 400 nm pulses with a portion of the fundamental 800 nm laser output in a 100-µm-thick BBO. The sum frequency signal at 266 nm is detected by a photomultiplier placed at the slit output of the spectrometer as a function of the relative time-delay between the 400 and 800 nm pulses, realized by varying the 800 nm optical path by means of a high-resolution linear translation stage (Physik Instrumente, M-505).

4.3.4 Results

4.3.5 Tilt-only chip tests

MEMS 1D mirror array is a pixelized (discrete) reflective device. Depending on the fill factor, the wavefront quality can be drastically affected by diffraction

due to mirror gaps. So it was logical to measure wafefront degradation after one pass through the MEMS shaper before evaluating its phase and amplitude shaping capacities. Figure 4.30 demonstrate laser spot measured with the beam profiler after the shaper set-up. Three different pictures (log scale) show the beam profile: a) after the shaper set-up with an Al mirror instead of MEMS device; b) with the MEMS device and the flat phase mask (all pixel had the same stroke); c) with the MEMS device and an arbitrary phase mask. These results demonstrated that no significant beam quality degradation was observed.
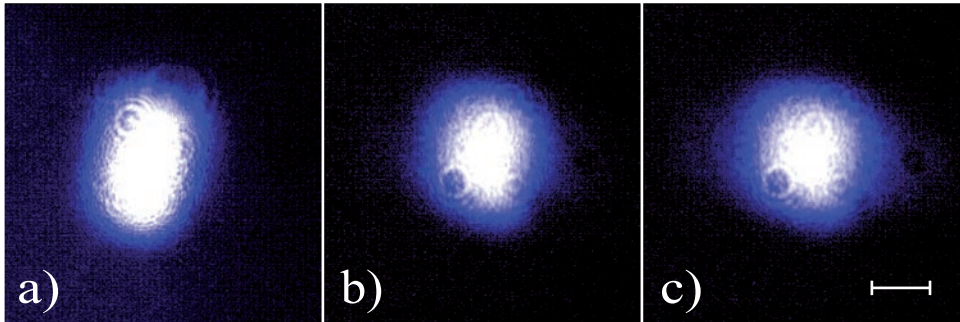
Figure 4.30: Laser beam profiles after one pass through the shaper set-up: a) with a Al mirror instead of MEMS device; b) with MEMS device and flat phase mask; c) with MEMS device and arbitrary phase mask.

Figure 4.31a shows the result of imposing a linear phase function ($a_1 \neq 0$ in Eq. 4.4) on the MEMS array resulting in a temporal delay. It is also remarkable from Figure 4.31b that there is no significant phase-amplitude coupling as the output spectrum remains unchanged while the phase is modified. The shaping was done at 800 nm wavelength, the time profiles and spectra were retrieved one-color XFROG measurements.

Figure 4.32 illustrates the effect of a quadratic phase mask $a_2 \neq 0$ at 400 nm central wavelength. Such a mask results in instant frequency variation of electric field in the time domain, a pulse chirp. Positive (or up-chirped) pulses (Fig. 4.32c), having instant frequency increasing through the temporal pulse profile, and negative (down-chirped) pulses (Fig.4.32a) were successfully obtained from initial Fourier transform limited reference (Fig.4.32b). Integrating the XFROG data over wavelengths provides the temporal profile (Fig.4.32d), and over time gives the pulse spectrum (Fig.4.32e) that remains unchanged as expected.

4.3.6   Piston-tilt chip tests

The same experimental set-up was employed for the tests of the second generation of MEMS devices. The chip is able to execute independently tilt and piston
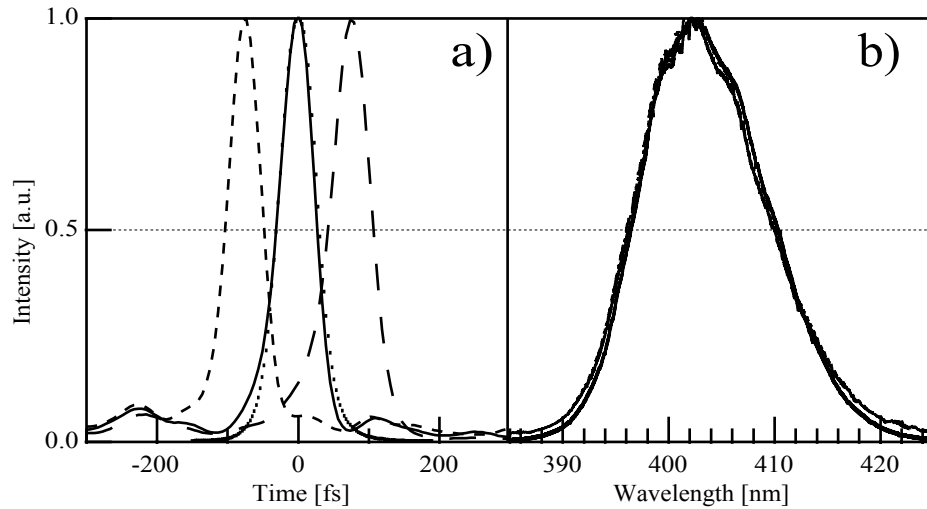
Figure 4.31: Inducing positive or negative time delay to all spectral components: a) time shift of ± 75 fs; b) doubled frequency pulse spectrum with positive, negative or without delay.

movement of each single mirror. Due to a limited fabrication yield, only a fraction of 22 consecutive working mirrors was obtained and used for the optical experiments. The tests were performed at 400 nm central wavelength and the two-color XFROG was used for time-wavelength trace extraction.

The first experiment was led to demonstrate binary amplitude shaping capabilities. As it was mentioned before, each single mirror is able to rotate around its axis and tilt the output direction of the corresponding spectral component. The result is that a part of the beam can be deflected and spatially distinguished at the shaper output. Placing a fibre spectrometer at the deflected and undeflected optical paths after the shaper allows direct observation of amplitude shaping in Figure 4.33 (red arrows indicate positions of non-working mirrors and their effect on output spectra).

Tilting every second mirror generates a periodic amplitude mask that results in pulse splitting and appearance of replica. The experimental measured XFROG traces for deflected spectral components are given in Figure 4.34c for the two different amplitude masks (Fig. 4.34a,b).

The next experiment demonstrates an unique capability of tilt-piston device of modifying simultaneously phase and amplitude of the laser pulses. Figure 4.35a demonstrates the interference between two spectral components with phase shift $\Delta\Phi = 0$ (solid line) and $\Delta\Phi = \pi$ (dashed line). The spectral separation between
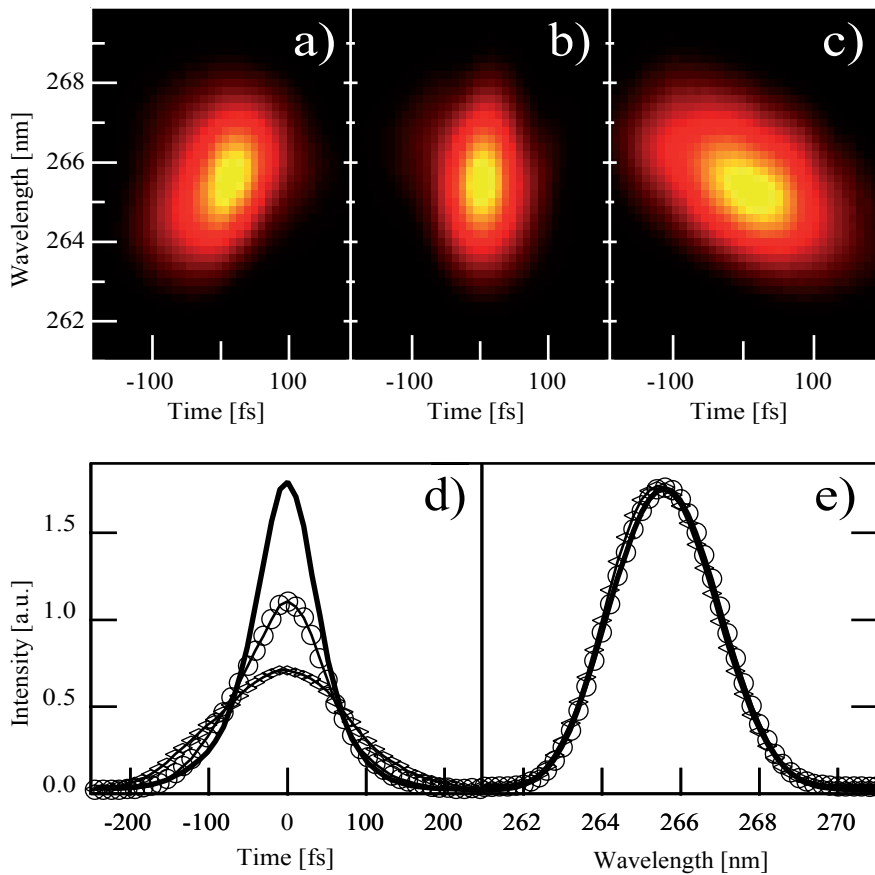
Figure 4.32: Demonstration of pulse chip generation capabilities: a) negative chirp; b) unchirped reference pulse; c) positive chirp; d) cross-correlation time profiles; e) spectra of chirped and unchirped pulses.

these components was about 3.3 nm. All other spectral components were tilted. Figure 4.35b represents the reverse situation where the phase shaping were done on deflected light path.

4.3.7 Discussions

The experiments presented here had as main goal to demonstrate the capabilities of our micro-mirror devices to shape phase and amplitude of femtosecond laser pulses throughout a broad spectral rage. The fact of being reflective brings enormous advantage over other non-reflective temporal shaping devices (liquid crystal array, acousto-optic shapers) because no transmission cut-off and no dispersion is induced by the device. Moreover, the reflectance of Al mirrors is quite high from deep UV to deep IR, and damage threshold of MEMS device is comparable to standard Al macro-mirror [38]. No beam profile degradation due to pixelization was
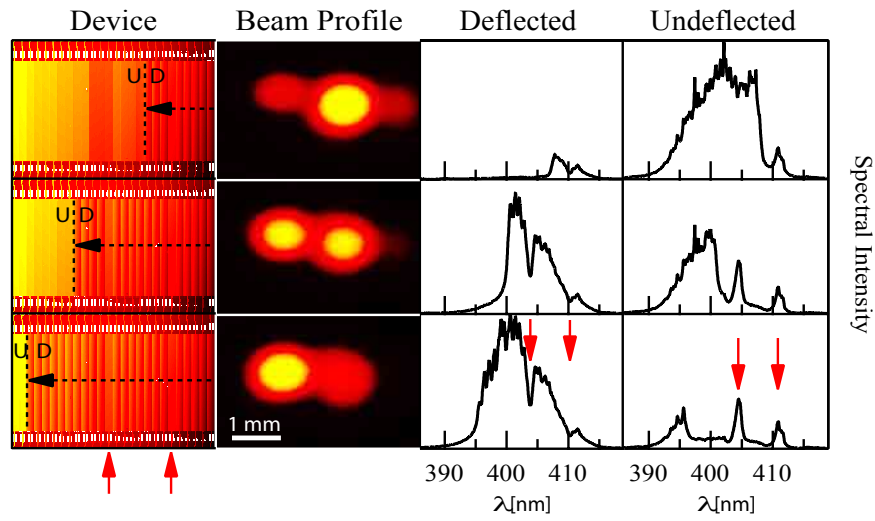
Figure 4.33: Binary amplitude shaping by individual mirror tilting.
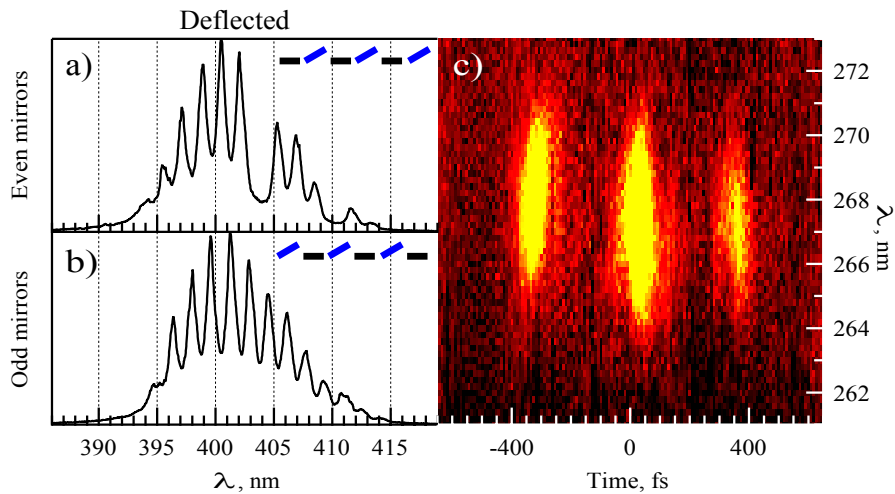
Figure 4.34: Amplitude mask test, one mirror over two is tilted: a) even mirrors tilted; b) odd mirrors tilted; c) resulting XFROG trace for both masks.

observed after MEMS shaper. The total energy throughput of the shaper is mainly limited by the diffraction grating efficiency.

The MEMS device based pulse shaper could induce some very basic modification of spectral components phase like time delay and frequency chirp. The tilt-piston chip could also produce binary amplitude shaping independent from phase shaping. It demonstrates that such MEMS shaper is able to integrate scientific laboratory set-up for different applications like pulse compression, linear and non-
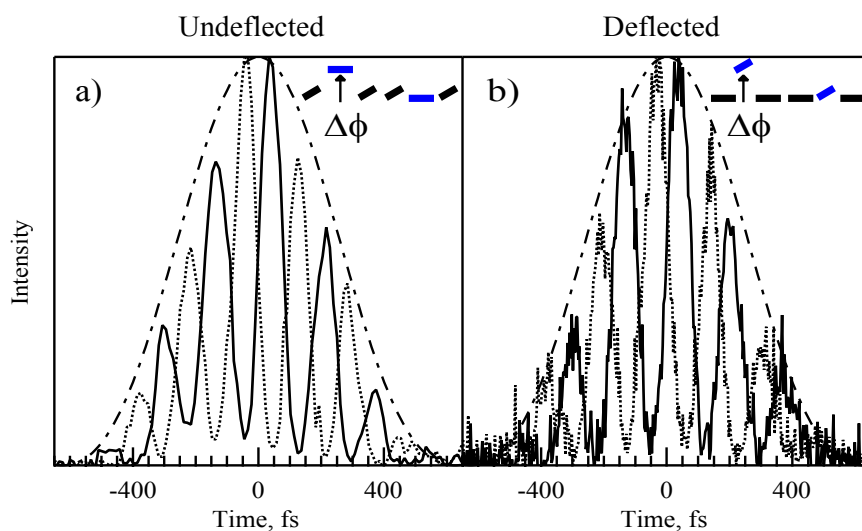
Figure 4.35: Phase-amplitude shaping example, interference between two spectral components: a) on undeflected mirrors, phase shift $\Delta\Phi = 0$ (solid line) and $\Delta\Phi = \pi$ (dashed line); b) on deflected mirrors, phase shift $\Delta\Phi = 0$ (solid line) and $\Delta\Phi = \pi$ (dashed line).

linear dispersion compensation or preparing of pulse trains or particular temporal shapes for coherent control experiments.

4.4 Pulse shaping in XUV region

4.4.1 Introduction

The previous chapters of the manuscript presented our latest advances in aerosol detection based on the light scattering and 1PEF or MPEF detection. On the other hand, we also demonstrated encouraging results in the pulse shaping with our newly developed MEMS shaper in the broad spectrum of wavelengths (from IR to deep UV). So, applying shaping based discrimination techniques, like ODD [33, 34, 35], which is also a research subject in our group, on the single aerosol particle would be a logical continuation of this PhD work. However, due to the femtosecond laser instability in the external trigger mode (see sect. 2.6) and to the low detection yield (see sect. 3.3) these experiments could not be performed up to now. As a consequence, we decided to extend the application field of the MEMS shaper to the extreme UV (XUV) region, downto 40 nm wavelength. These tests were done in collaboration with the group of Prof. H.J. Woerner (ETH Zurich).

The high harmonic generation (HHG) and attosecond pulses [112] and their applications is a rapidly growing research field in the XUV region. It opens new

perspectives in the coherent manipulation of atomic and molecular electrons [113]. However, modifying directly the amplitude and the phase of spectral components of such short pulses constitutes a complex technological challenge. Until now, pulse shaping in the XUV region ($10^{-7} - 10^{-10}$ nm) was performed by indirect methods [114, 115, 116]. Despite these advances, direct shaping would still provide a higher flexibility and control on the XUV attosecond pulses.

This chapter describes the very first steps towards direct XUV temporal shaping with the MEMS technology. In particular, it presents the results of the amplitude shaping of high harmonics (HH) in the XUV. The two main possibilities were explored: a binary amplitude shaping and a linear amplitude shaping. The first method allows complete attenuation of a selected HH while keeping others unaffected, which will directly modify the temporal profile of the XUV pulses. The second approach permits to reduce smoothly the amplitude of a selected HH while keeping other HH unchanged.

These proof-of-principle experiments aim at the evaluation of the potential use of MEMS devices in the far UV for the shaping applications. The demonstration of the direct amplitude shaping capabilities of attosecond pulses will be an important step towards the complete (phase and amplitude) modulation of attosecond pulse waveforms.

4.4.2 Experimental

The classical approach employing a molecular jet (in our case Argon and ethylene C_2H_4) exposed to an intense IR femtosecond pulses in vacuum was used in this experiment (see Sect. 9). Figure 4.36 shows the main components. The experiment, performed in ETHZ, comprises a femtosecond CPA laser ($\Delta\tau = 30$ fs, $E_p = 0.7$ mJ, f = 1 kHz) **LS**, a focusing lens **L1**, a molecular jet of gas **GJ**, an input slit **S1** which defines the size of the input beam, a diffraction grating **G1**, a second slit **S2** which eliminates unshaped harmonics, the MEMS device or flat Al mirror **M1**, a blocking mask **H1**, a micro-channel plate (MCP) screen **D1** and a CCD camera **C1**.

The alignment and Al reflectivity test (Fig. 4.37a) were done with a flat Al mirror (coated with a UV enhanced Al layer). These tests were necessary to determine the shortest reflected HH seen by the detector. As MEMS micro-mirror arrays described in Section 4.2.1 were coated with Al too, this test permitted to estimate the reflectivity of the MEMS 1D mirror array (Fig. 4.37b).

The input IR laser beam had central wavelength at 800 nm, 0.7 mJ energy focused with a f $= 100$ mm spherical lens of the gas jet. The generated HH beam had diameter about 1 mm sized by the input slit **S1**. The diffraction grating is
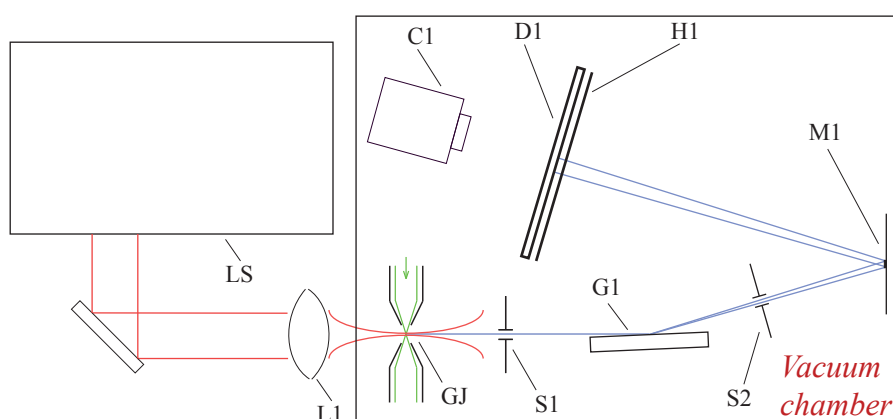
Figure 4.36: Scheme of experiment: **LS** - femtosecond CPA laser, **L1** - focusing lens, **GJ** - molecular jet of argon gas, **S1** - slit, **G1** - concave diffraction grating, **S2** - slit, **M1** - MEMS device or flat Al mirror, **H1** - blocking mask, **D1** - MCP screen, **C1** - CCD camera.
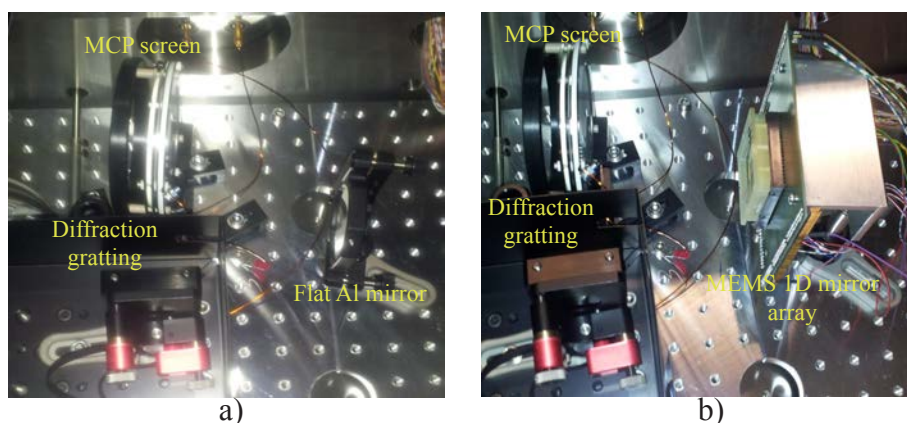
Figure 4.37: Photographs of experiment: a) set-up with a flat Al mirror; b) set-up with the MEMS device.

concave, with 1200 grooves/mm density, $87.5°$ incident angle and 237 mm focal length. The generated harmonics had calculated wavelength and diffraction angles presented in Table 4.4.

1st order diffraction angles are needed to determine the HH order from the image captured on the CCD camera. 2nd order of diffraction will also appear and it is important to take it into account for the image correction.

The MEMS device with tilt/piston architecture was used in this experiment (see Sect. 4.2.1). The maximum achievable tilt angle for each mirror is about $1°$. As it

Table 4.4: HH wavelength and diffraction angles

Harmonic	Wavelength, nm	1st order diffraction angle, °	2nd order diffraction angle, °
1	800	2	-
3	266.7	42	21
5	166	53	37
7	114.3	59	46
9	88.9	63	52
11	72.7	65.7	55.5
13	61.5	67.6	58.3
15	53.3	69.2	60.5
17	47.1	70.4	62.3
19	42.1	71.5	63.8
21	38.1	72.3	65.1
23	34.8	73.5	66.2

was mentioned before, due to technical difficulties, not all mirrors were working. So a region of 24 mirrors with only few dysfunctional pixels was employed for amplitude shaping. The rest of the chip was used as a flat mirror, and the corresponding pixels were not connected. A metallic mask with small periodic openings was placed in front of the MCP screen. It serves to block some HH while others pass through. After reflection from the MEMS device, HH high energy photons strike the MCP screen. The back plate of MCP screen is imaged by a high resolution CCD camera.

4.4.3   Results

The first test was led to investigate the reflectivity of the MEMS 1D array in comparison with an Al mirror. It also permitted to determine the highest harmonic order that can be reflected. Figure 4.38 shows the result of this test. The highest detectable harmonic for both MEMS and Al mirror was $n = 19$ corresponding to 42.1 nm wavelength. The HH spot quality had no visible degradation due to the pixelization. The order of HH was determined by the geometrical position on the MCP screen with given incidence angle of the diffraction grating. The positions of HH on the MCP screen were stable as in the case of the Al mirror reflection.

The binary amplitude shaping was tested on 9th (Fig. 4.39) and 11th (Fig. 4.40) harmonics. Due to the presence of non-working pixels, it was not possible to block completely H9 harmonic. In the case of H11, the attenuation was complete.

The HH spots were spread over few pixels on the MEMS array, which gave the possibility to attenuate a selected harmonic by tilting mirrors one by one. Figure
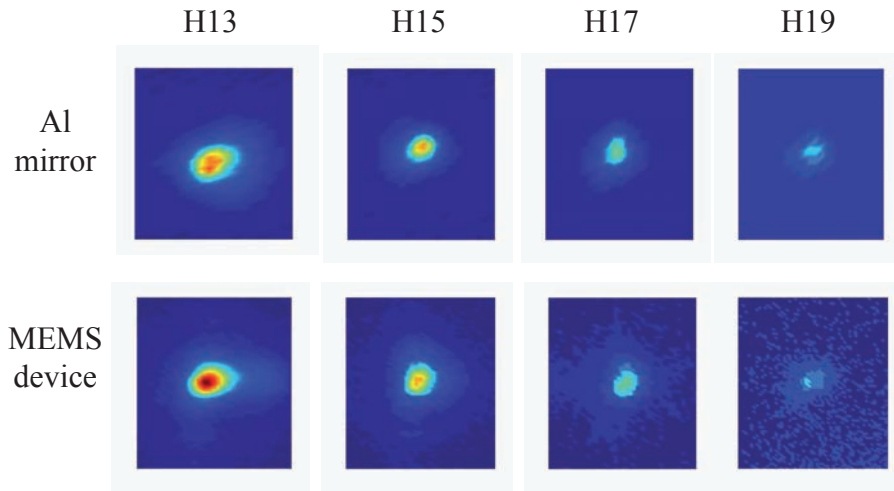
Figure 4.38: Reflectivity comparison test: Al mirror and MEMS device.
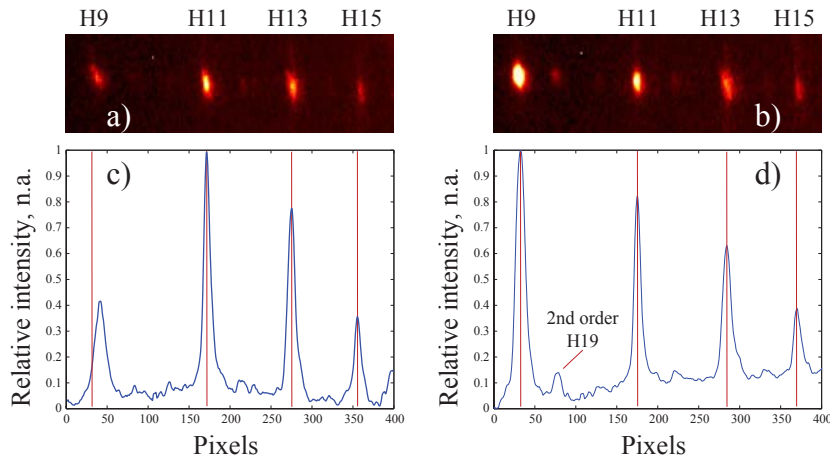
Figure 4.39: Binary amplitude shaping of the 9th harmonic: a),c) no deflection introduced, H9 is blocked by the mask, b),d) around 1° deflection set, H9 reaches the MCP screen.

4.41 illustrates the resulting intensities of H11 when the corresponding pixels are tilted consequently. Once again, non-working mirrors did not permit to obtain a smooth attenuation curve (Fig. 4.41h in blue). With all working mirrors and higher grating dispersion resulting selected harmonic to be reflected by large number of pixels, the attenuation characteristic will tend to a cumulative distribution function if the HH spot has a Gaussian intensity distribution. It is also possible to attenuate the amplitudes of several HH in the same time with a continuous 1D array of working mirrors.
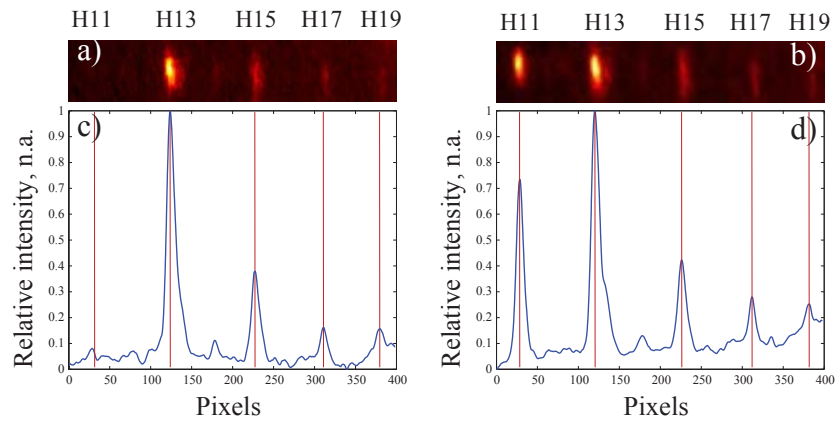
Figure 4.40: Binary amplitude shaping of the 11th harmonic: a),c) no deflection introduced, H11 is blocked by the mask, b),d) around $1°$ deflection set, H11 reaches the MCP screen.

4.4.4 Prospectives

The presented experiment on HH proved that MEMS devices can be used in the XUV and manipulate HH. The next step will be to perform the amplitude shaping in the strict sense of the term, meaning recombine the modulated spectral components together to obtain an attosecond laser pulse train.

To obtain this, we will need to rearrange the set-up in to a folded 4F zero dispersion compressor geometry as it is shown in Figure 4.42. In the XUV obviously, only reflective-only components can be used. One possible solution would to employ a flat grating and a off-axis parabolic reflector. Particular care will have to be brought to the deflecting mirror coating, as HH incidence angle is close to $45°$. Recent multilayer coatings, developed by Munich-Centre for Advanced Photonics (MAP), appear to provide good reflecting even with those large incident angles.

The input and output beams can be separated by a small tilting (few degr.) in the vertical plane. The amplitude shaping can be performed by tilting and blocking of selected HH in the beam stop **BS**. If we suppose that such an arrangement has zero phase dispersion, the effect of the amplitude shaping will be like it is shown in Figure 4.43. (a) represents unmodified attosecond pulse train, (b), (c) and (d) illustrate an example of blocking of one, two or three harmonics, respectively. The left column reports the electric field in time domain and its corresponding spectrum in the frequency domain.

As expected, attenuating more and more harmonics in the pulse spectrum tends to produce a continuous plane wave instead of the train of pulses for the given
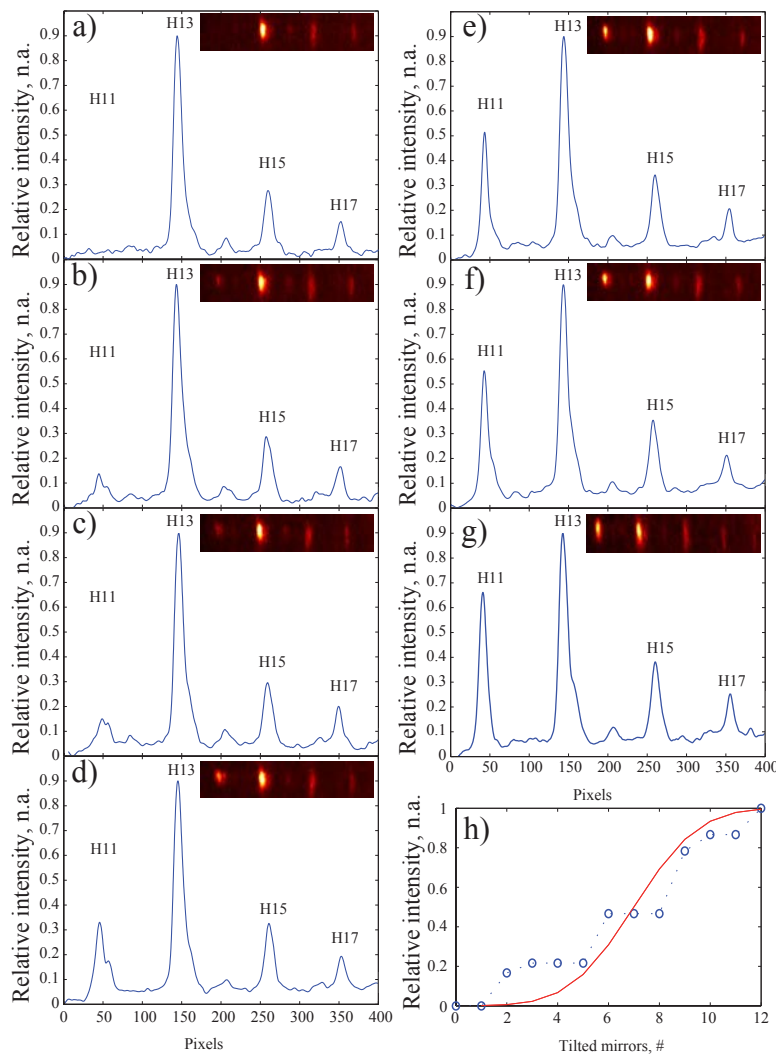
Figure 4.41: Amplitude shaping of 11th harmonic: a) no mirrors tilted, b) 2 mirrors tilted, c) 3-5 mirrors tilted, d) 6-8 mirrors tilted, e) 9 mirrors tilted, f) 10-11 mirrors tilted, g) 12 mirrors tilted, h) resulting H11 relative intensity.

time window. In reality, one can expect that keeping only one HH and blocking all the others in the initial spectrum will produce a laser pulse with Gaussian profile which duration will be limited by the Fourier transform of the spectral bandwidth (FWHM) of this selected harmonic. This property of binary amplitude shaping can be used to generate XUV laser pulses with tuned central wavelength.

The same experimental set-up can also be used for phase pulse shaping. In this case, a stroke MEMS device should be used. The best achievable mirror flatness
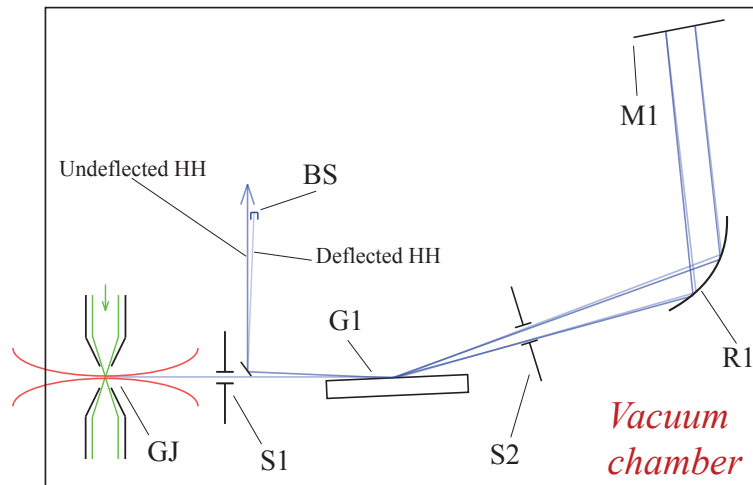
Figure 4.42: Future set-up for the amplitude XUV shaping: **GJ** - molecular jet of argon gas, **S1** - slit, **G1** - plane diffraction grating, **S2** - slit, **R1** - off-axis parabolic reflector, **M1** - MEMS device, **BS** - beam stop.
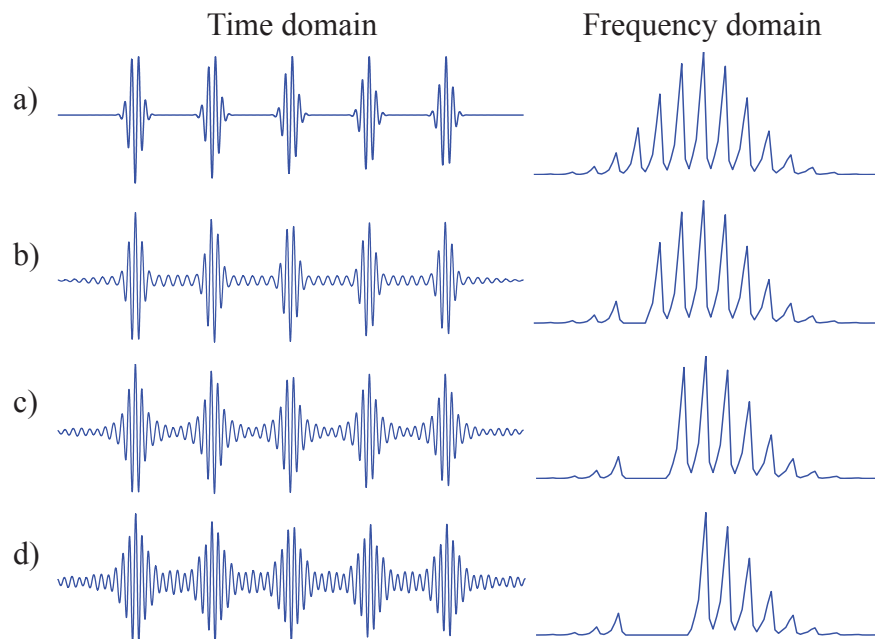
Figure 4.43: Example of of the amplitude shaping on an attosecond pulse train: a) no harmonics blocked, b) one harmonic blocked, c) two harmonics blocked, d) three harmonics blocked.

that we could measure until now was about 10 nm peak-to-valley for a single pixel

(see Sect. 4.2.1). Comparing with the lowest reflected wavelength (40 nm) leads to a $\lambda/4$ single mirror flatness, which is, of course, only suitable for a large phase modulations. However, with the rapidly developing MEMS technology, we expect that phase and amplitude XUV pulse shaping will be performed soon.

4.4.5 Discussion

The experiment on HH amplitude control demonstrated possibility of amplitude shaping. A rearrangement of the optical path into a classical folded 4F reflective shaper configuration would permit true amplitude shaping of HH attosecond pulses. Indeed, if one uses a flat diffraction grating, a focusing parabolic mirror and the MEMS device in the Fourier plane, one can recombine HH in an attosecond pulse train.

The technique of HH generation used in this experiment can produce short trains of attosecond pulses separated by the period of oscillation of the pump laser field. In the Fourier plane it corresponds to narrow lines representing harmonics. Amplitude shaping of HH gives an opportunity to modify temporal profile of the recombined pulse train. This approach presents a radically new way of manipulating XUV pulses dynamically.

As it was mentioned and show in Section 4.3, the MEMS 1D mirror array is also able to make stroke movement, which opens the possibility to act on the spectral components phases. The next step experiments in the XUV shaping will be the phase modulation. This experiment will need a folded 4F zero dispersion compressor arrangement and an additional tool to measure the pulse phase. Coupled with the amplitude shaping, this gives access to a completely new field of research of attosecond scale effects like electron motions in atoms.

Bibliography

[1] H. Burge, "Bioaerosols - prevalence and health-effects in the indoor environment," *J Allergy Clin Immun*, vol. 86, no. 5, pp. 687–701, 1990.

[2] Y. Gilbert and C. Duchaine, "Bioaerosols in industrial environments: a review," *Can J Civil Eng*, vol. 36, no. 12, pp. 1873–1886, 2009.

[3] P. Srikanth, S. Sudharsanam, and R. Steinberg, "Bio-aerosols in indoor environment: Composition, health effects and analysis," *Indian J Med Microbi*, vol. 26, no. 4, pp. 302–312, 2008.

[4] T. F. Eck, B. N. Holben, A. Sinyuk, R. T. Pinker, P. Goloub, H. Chen, B. Chatenet, Z. Li, R. P. Singh, S. N. Tripathi, J. S. Reid, D. M. Giles, O. Dubovik, N. T. O'Neill, A. Smirnov, P. Wang, and X. Xia, "Climatological aspects of the optical properties of fine/coarse mode aerosol mixtures," *J Geophys Res-Atmos*, vol. 115, 2010.

[5] H. Bauer, H. Giebl, R. Hitzenberger, A. Kasper-Giebl, G. Reischl, F. Zibuschka, and H. Puxbaum, "Airborne bacteria as cloud condensation nuclei," *J. Geophys. Res.*, vol. 108, no. D21, p. 4658, 2003.

[6] J. Portnoy and C. Barnes, "The national allergy bureau: Pollen and spore reporting today," *J Allergy Clin Immun*, vol. 114, no. 5, pp. 1235–1238, 2004.

[7] G. J. Burbach, L. M. Heinzerling, C. Rohnelt, K. C. Bergmann, H. Behrendt, and T. Zuberbier, "Ragweed sensitization in europe - GA(2)LEN study suggests increasing prevalence," *Allergy*, vol. 64, no. 4, pp. 664–665, 2009.

[8] H. C. Lane, J. La Montagne, and A. S. Fauci, "Bioterrorism: A clear and present danger," *Nat Med*, vol. 7, no. 12, pp. 1271–1273, 2001.

[9] P. Bossi, D. Garin, A. Guihot, F. Gay, J. Crance, T. Debord, B. Autran, and F. Bricaire, "Biological weapons," *Cellular and Molecular Life Sciences*, vol. 63, no. 19, pp. 2196–2212, 2006.

[10] J. Ho, "Future of biological aerosol detection," *Anal Chim Acta*, vol. 457, no. 1, pp. 125–148, 2002.

[11] P. Belgrader, W. Benett, D. Hadley, J. Richards, P. Stratton, R. Mariella, and F. Milanovich, "Infectious disease - PCR detection of bacteria in seven minutes," *Science*, vol. 284, no. 5413, pp. 449–450, 1999.

[12] T. H. Rider, M. S. Petrovick, F. E. Nargi, J. D. Harper, E. D. Schwoebel, R. H. Mathews, D. J. Blanchard, L. T. Bortolin, A. M. Young, J. Z. Chen, and M. A. Hollis, "A B cell-based sensor for rapid identification of pathogens," *Science*, vol. 301, no. 5630, pp. 213–215, 2003.

[13] C. Hagleitner, A. Hierlemann, D. Lange, A. Kummer, N. Kerness, O. Brand, and H. Baltes, "Smart single-chip gas sensor microsystem," *Nature*, vol. 414, no. 6861, pp. 293–296, 2001.

[14] G. F. Crosta, S. Zomer, Y. L. Pan, and S. Holler, "Classification of single-particle two-dimensional angular optical scattering patterns and heuristic scatterer reconstruction," *Opt Eng*, vol. 42, no. 9, pp. 2689–2701, 2003.

[15] K. B. Aptowicz, R. G. Pinnick, S. C. Hill, Y. L. Pan, and R. K. Chang, "Optical scattering patterns from single urban aerosol particles at Adelphi, Maryland, USA: A classification relating to particle morphologies," *J Geophys Res-Atmos*, vol. 111, no. D12, 2006.

[16] S. C. Hill, R. G. Pinnick, P. Nachman, G. Chen, R. K. Chang, M. W. Mayo, and G. L. Fernandez, "Aerosol-fluorescence spectrum analyzer - real-time measurement of emission-spectra of airborne biological particles," *Appl Optics*, vol. 34, no. 30, pp. 7149–7155, 1995.

[17] P. P. Hairston, J. Ho, and F. R. Quant, "Design of an instrument for real-time detection of bioaerosols using simultaneous measurement of particle aerodynamic size and intrinsic fluorescence," *J Aerosol Sci*, vol. 28, no. 3, pp. 471–482, 1997.

[18] F. L. Reyes, T. H. Jeys, N. R. Newbury, C. A. Primmerman, G. S. Rowe, and A. Sanchez, "Bio-aerosol fluorescence sensor," *Field Anal Chem Tech*, vol. 3, no. 4-5, pp. 240–248, 1999.

[19] P. H. Kaye, E. Hirst, V. Foot, J. M. Clark, and K. Baxter, "A low-cost multi-channel aerosol fluorescence sensor for networked deployment," *P Soc Photo-Opt Ins*, vol. 5617, pp. 388–398, 2004.

[20] R. L. Armstrong, J. B. Mason, and T. Barber, "Detection of atmospheric aerosol flow using a transit-time LIDAR velocimeter," *Appl Optics*, vol. 15, no. 11, pp. 2891–2895, 1976.

[21] B. Stein, M. Delguasta, J. Kolenda, M. Morandi, P. Rairoux, L. Stefanutti, J. P. Wolf, and L. Woste, "Stratospheric aerosol-size distributions from multispectral LIDAR measurements at sodankyla during easoe," *Geophys Res Lett*, vol. 21, no. 13, pp. 1311–1314, 1994.

[22] D. Mondelain, B. Vezin, E. Frejafon, V. Boutou, A. Thomasson, and J. P. Wolf, "Infrared LIDAR with optical parametric oscillator for aerosol detection," *J Phys Iv*, vol. 10, no. P8, pp. 157–159, 2000.

[23] C. R. Prasad, H. S. Lee, I. H. Hwang, M. Nam, S. Mathur, and B. Ranganayakamma, "Portable digital LIDAR - a compact stand-off bioagent aerosol sensor," *Chemical and Biological Sensing Ii*, vol. 4378, pp. 50–59, 2001.

[24] J. Bufton, "Development of the LIDAR controlled-airspace scanner for bio-aerosol detection," *2007 Conference on Lasers and Electro-Optics/Quantum Electronics and Laser Science Conference (Cleo/Qels 2007), Vols 1-5*, pp. 2776–2776, 2007.

[25] A. Achey, J. Bufton, J. Dawson, W. Huang, S. Lee, N. Mehta, and C. Prasad, "An enhanced multi-wavelength ultraviolet biological trigger LIDAR," *P Soc Photo-Opt Ins*, vol. 5617, pp. 87–91, 2004.

[26] F. Immler, D. Engelbart, and O. Schrems, "Fluorescence from atmospheric aerosol detected by a LIDAR indicates biogenic particles in the lowermost stratosphere," *Atmos Chem Phys*, vol. 5, pp. 345–355, 2005.

[27] Y. L. Pan, R. G. Pinnick, S. C. Hill, and R. K. Chang, "Particle-fluorescence spectrometer for real-time single-particle measurements of atmospheric organic carbon and biological aerosol," *Environ. Sci. Technol.*, vol. 43, no. 2, pp. 429–434, 2009.

[28] M. Dantus and V. V. Lozovoy, "Experimental coherent laser control of physicochemical processes," *Chem Rev*, vol. 104, no. 4, pp. 1813–1859, 2004.

[29] T. Brixner, N. H. Damrauer, P. Niklaus, and G. Gerber, "Photoselective adaptive femtosecond quantum control in the liquid phase," *Nature*, vol. 414, no. 6859, pp. 57–60, 2001.

[30] T. Brixner, N. H. Damrauer, B. Kiefer, and G. Gerber, "Liquid-phase adaptive femtosecond quantum control: Removing intrinsic intensity dependencies," *J Chem Phys*, vol. 118, no. 8, pp. 3692–3701, 2003.

[31] V. Sivaprakasam, H. B. Lin, A. L. Huston, and J. D. Eversole, "Spectral characterization of biological aerosol particles using two-wavelength excited laser-induced fluorescence and elastic scattering measurements," *Opt Express*, vol. 19, no. 7, pp. 6191–6208, 2011.

[32] D. Kiselev, L. Bonacina, and J. P. Wolf, "Individual bioaerosol particle discrimination by multi-photon excited fluorescence," *Opt Express*, vol. 19, no. 24, pp. 24516–24521, 2011.

[33] M. Roth, L. Guyon, J. Roslund, V. Boutou, F. Courvoisier, J. P. Wolf, and H. Rabitz, "Quantum control of tightly competitive product channels," *Phys Rev Lett*, vol. 102, no. 25, 2009.

[34] J. Roslund, M. Roth, L. Guyon, V. Boutou, F. Courvoisier, J. P. Wolf, and H. Rabitz, "Resolution of strongly competitive product channels with optimal dynamic discrimination: Application to flavins," *J Chem Phys*, vol. 134, no. 3, 2011.

[35] A. Rondi, L. Bonacina, A. Trisorio, C. Hauri, and J. P. Wolf, "Coherent manipulation of free amino acids fluorescence," *Physical Chemistry Chemical Physics*, 2012.

[36] A. M. Weiner, J. P. Heritage, and E. M. Kirschner, "High-resolution femtosecond pulse shaping," *J Opt Soc Am B*, vol. 5, no. 8, pp. 1563–1572, 1988.

[37] S. M. Weber, J. Extermann, L. Bonacina, W. Noell, D. Kiselev, S. Waldis, N. F. de Rooij, and J. P. Wolf, "Ultraviolet and near-infrared femtosecond temporal pulse shaping with a new high-aspect-ratio one-dimensional micromirror array," *Opt Lett*, vol. 35, no. 18, pp. 3102–3104, 2010.

[38] S. M. Weber, L. Bonacina, W. Noell, D. Kiselev, J. Extermann, F. Jutzi, S. Lani, O. Nenadl, J. P. Wolf, and N. F. de Rooij, "Design, simulation, fabrication, packaging, and characterization of a MEMS-based mirror array for femtosecond pulse-shaping in phase and amplitude," *Rev. Sci. Instrum.*, vol. 82, no. 7, 2011.

[39] J. Extermann, S. M. Weber, D. Kiselev, L. Bonacina, S. Lani, F. Jutzi, W. Noell, N. F. de Rooij, and J. P. Wolf, "Spectral phase, amplitude, and spatial modulation from ultraviolet to infrared with a reflective MEMS pulse shaper," *Opt Express*, vol. 19, no. 8, pp. 7580–7586, 2011.

[40] S. G. Buckley, J. D. Hybl, and G. A. Lithgow, "Laser-induced breakdown spectroscopy detection and classification of biological aerosols," *Appl Spectrosc*, vol. 57, no. 10, pp. 1207–1215, 2003.

[41] A. Boreysho, A. Savin, A. Morozov, M. Konyaev, and K. Konovalov, "Remote detection and recognition of bio-aerosols by laser-induced fluorescense LIDAR - practical implementation and field tests," *Proc Spie*, vol. 6733, 2007.

[42] P. H. Kaye, W. R. Stanley, E. Hirst, E. V. Foot, K. L. Baxter, and S. J. Barrington, "Single particle multichannel bio-aerosol fluorescence sensor," *Opt Express*, vol. 13, no. 10, pp. 3583–3593, 2005.

[43] P. Hairston, "Application of UV LEDs to the design of low cost biological aerosol detectors," *2009 Conference on Lasers and Electro-Optics and Quantum Electronics and Laser Science Conference (Cleo/Qels 2009), Vols 1-5*, pp. 3247–3247, 2009.

[44] Y. L. Pan, S. C. Hill, R. G. Pinnick, J. M. House, R. C. Flagan, and R. K. Chang, "Dual-excitation-wavelength fluorescence spectra and elastic scattering for differentiation of single airborne pollen and fungal particles," *Atmos Environ*, vol. 45, no. 8, pp. 1555–1563, 2011.

[45] S. C. Hill, R. G. Pinnick, S. Niles, Y. L. Pan, S. Holler, R. K. Chang, J. Bottiger, B. T. Chen, C. S. Orr, and G. Feather, "Real-time measurement of fluorescence spectra from single airborne biological particles," *Field Anal Chem Tech*, vol. 3, no. 4-5, pp. 221–239, 1999.

[46] V. Sivaprakasam, A. L. Huston, C. Scotto, and J. D. Eversole, "Multiple UV wavelength excitation and fluorescence of bioaerosols," *Opt Express*, vol. 12, no. 19, pp. 4457–4466, 2004.

[47] E. Bontempi, A. Zacco, D. Benedetti, L. Borgese, P. Colombi, H. Stosnach, G. Finzi, P. Apostoli, P. Buttini, and L. E. Depero, "Total reflection X-ray fluorescence (TXRF) for direct analysis of aerosol particle samples," *Environ Technol*, vol. 31, no. 5, pp. 467–477, 2010.

[48] S. C. Hill, R. G. Pinnick, S. Niles, N. F. Fell, Y. L. Pan, J. Bottiger, B. V. Bronk, S. Holler, and R. K. Chang, "Fluorescence from airborne microparticles: dependence on size, concentration of fluorophores, and illumination intensity," *Appl Optics*, vol. 40, no. 18, pp. 3005–3013, 2001.

[49] M. Baudelet, L. Guyon, J. Yu, J. P. Wolf, T. Amodeo, E. Frejafon, and P. Laloi, "Femtosecond time-resolved laser-induced breakdown spectroscopy for detection and identification of bacteria: A comparison to the nanosecond regime," *J Appl Phys*, vol. 99, no. 8, 2006.

[50] J. Yu, M. Baudelet, M. Bossu, J. Jovelet, J. P. Wolf, T. Amodeo, E. Frejafon, and P. Laloi, "Discrimination of microbiological samples using femtosecond laser-induced breakdown spectroscopy," *Appl Phys Lett*, vol. 89, no. 16, p. 163903, 2006.

[51] M. Gherasimova, J. Han, Y. K. Song, A. V. Nurmikko, Y. L. Pan, and R. K. Chang, "UV LEDs for fluorescence detection of biological particles: from materials to applications - art. no. 61340h," *Light-EMiting Diodes: Research, Manufacturing, and Applications X*, vol. 6134, pp. H1340–H1340, 2006.

[52] R. S. Deng, X. F. Zhang, K. A. Smith, J. Wormhoudt, D. K. Lewis, and A. Freedman, "Focusing particles with diameters of 1 to 10 microns into

beams at atmospheric pressure," *Aerosol Sci. Technol.*, vol. 42, no. 11, pp. 899–915, 2008.

[53] Y.-L. Pan, J. Bowersett, S. C. Hill, R. G. Pinnick, and R. K. Chang, "Nozzles for focusing aerosol particles," tech. rep., 2009.

[54] A. Manninen, M. Putkiranta, J. Saarela, A. Rostedt, T. Sorvajarvi, J. Toivonen, M. Marjamaki, J. Keskinen, and R. Hernberg, "Fluorescence cross sections of bioaerosols and suspended biological agents," *Appl Optics*, vol. 48, no. 22, pp. 4320–4328, 2009.

[55] C. Xu, R. M. Williams, W. Zipfel, and W. W. Webb, "Multiphoton excitation cross-sections of molecular fluorophores," *Bioimaging*, vol. 4, no. 3, pp. 198–207, 1996.

[56] S. H. Huang, A. A. Heikal, and W. W. Webb, "Two-photon fluorescence spectroscopy and microscopy of NAD(P)H and flavoprotein," *Biophys J*, vol. 82, no. 5, pp. 2811–2825, 2002.

[57] J. D. Eversole, C. S. Scotto, M. Spence, and A. J. Campillo, "Continuous bioaerosol monitoring using UV excitation fluorescence," *Optics for the Quality of Life, Pts 1 and 2*, vol. 4829, pp. 532–533, 2003.

[58] P. Macheroux, "UV-visible spectroscopy as a tool to study flavoproteins," *Methods in molecular biology (Clifton, N.J.)*, vol. 131, pp. 1–7, 1999.

[59] Y. L. Pan, P. Cobler, S. Rhodes, A. Potter, T. Chou, S. Holler, R. K. Chang, R. G. Pinnick, and J. P. Wolf, "High-speed, high-sensitivity aerosol fluorescence spectrum detection using a 32-anode photomultiplier tube detector," *Rev. Sci. Instrum.*, vol. 72, no. 3, pp. 1831–1836, 2001.

[60] P. H. Kaye, J. E. Barton, E. Hirst, and J. M. Clark, "Simultaneous light scattering and intrinsic fluorescence measurement for the classification of airborne particles," *Appl Optics*, vol. 39, no. 21, pp. 3738–3745, 2000.

[61] J. D. Eversole, J. J. Hardgrove, W. K. Cary, D. P. Choulas, and M. Seaver, "Continuous, rapid biological aerosol detection with the use of UV fluorescence: Outdoor test results," *Field Anal Chem Tech*, vol. 3, no. 4-5, pp. 249–259, 1999.

[62] Y. L. Pan, S. Holler, R. K. Chang, S. C. Hill, R. G. Pinnick, S. Niles, J. R. Bottiger, and B. V. Bronk, "Real-time detection and characterization of individual flowing airborne biological particles: fluorescence spectra and elastic scattering measurements," *Air Monitoring and Detection of Chemical and Biological Agents Ii*, vol. 3855, pp. 117–125, 1999.

[63] S. Flyckt and C. Marmonier, *Photomultiplier Tubes: Principles and Applications*. 2002.

[64] H. Malmstadt, C. Enke, and S. Crouch, *Electronics and Instrumentation for Scientists*. 1981.

[65] T. Delton, *Basic electronics theory*. 1994.

[66] N. Semiconductor, "Design considerations for a transimpedance amplifier," tech. rep., 2008.

[67] X. Ramus, "Transimpedance considerations for high-speed amplifiers," tech. rep., Texas Instruments, 2009.

[68] R. A. Gayakwad, *Op-Amps and linear integrated Circuits*. 1999.

[69] P. Pong, FPGA *Prototyping by* VHDL *Examples: Xilinx Spartan-3 Version*. 2008.

[70] V. A. Pedroni, *Circuit Design and Simulation with* VHDL. 2010.

[71] J. Richardson and J. Harker, *Chemical engineering*. 2007.

[72] C. Cox and C. Wathes, *Bioaerosol handbook*. 1995.

[73] P. Kulkarni, P. Baron, and K. Willeke, *Aerosol measurement: principles, techniques and applications*. 2011.

[74] P. H. Kaye, E. Hirst, J. M. Clark, and F. Micheli, "Airborne particle-shape and size classification from spatial light-scattering profiles," *J Aerosol Sci*, vol. 23, no. 6, pp. 597–611, 1992.

[75] S. Holler, Y. L. Pan, R. K. Chang, J. R. Bottiger, S. C. Hill, and D. B. Hillis, "Two-dimensional angular optical scattering for the characterization of airborne microparticles," *Opt Lett*, vol. 23, no. 18, pp. 1489–1491, 1998.

[76] M. Surbek, C. Esen, G. Schweiger, and A. Ostendorf, "Pollen characterization and identification by elastically scattered light," *J Biophotonics*, vol. 4, no. 1-2, pp. 49–56, 2011.

[77] Y. L. Pan, J. Hartings, R. G. Pinnick, S. C. Hill, J. Halverson, and R. K. Chang, "Single-particle fluorescence spectrometer for ambient aerosols," *Aerosol Sci. Technol.*, vol. 37, no. 8, pp. 628–639, 2003.

[78] W. Zakowicz, "Scattering of narrow stationary beams and short pulses on spheres," *Epl-Europhys Lett*, vol. 85, no. 4, 2009.

[79] C. Bohren and J. A. Huffman, *Absorption and scattering of light by small particles*. 1998.

[80] Y. L. Pan, S. C. Hill, R. G. Pinnick, H. Huang, J. R. Bottiger, and R. K. Chang, "Fluorescence spectra of atmospheric aerosol particles measured using one or two excitation wavelengths: Comparison of classification schemes employing different emission and scattering results," *Opt Express*, vol. 18, no. 12, pp. 12436–12457, 2010.

[81] A. M. Gabey, W. R. Stanley, M. W. Gallagher, and P. H. Kaye, "The fluorescence properties of aerosol larger than 0.8 mu m in urban and tropical rainforest locations," *Atmos Chem Phys*, vol. 11, no. 11, pp. 5491–5504, 2011.

[82] S. Hill, M. Mayo, and R. Chang, "Fluorescence of bacteria, pollens, and naturally occurring airborne particles: Excitation/emission spectra," tech. rep., 2009.

[83] J. C. Auger, G. E. Fernandes, K. B. Aptowicz, Y. L. Pan, and R. K. Chang, "Influence of surface roughness on the elastic-light scattering patterns of micron-sized aerosol particles," *Appl Phys B-Lasers O*, vol. 99, no. 1-2, pp. 229–234, 2010.

[84] M. Surbek, C. Esen, and G. Schweiger, "Elastic light scattering on single pollen: Scattering in a large space angle," *Aerosol Sci. Technol.*, vol. 43, no. 7, pp. 679–684, 2009.

[85] D. A. Saucy, J. R. Anderson, and P. R. Buseck, "Aerosol-particle characteristics determined by combined cluster and principal component analysis," *J Geophys Res-Atmos*, vol. 96, no. D4, pp. 7407–7414, 1991.

[86] G. A. Luoma, P. P. Cherrier, and L. A. Retfalvi, "Real-time warning of biological-agent attacks with the canadian integrated biochemical agent detection system II (CIBADS II)," *Field Anal Chem Tech*, vol. 3, no. 4-5, pp. 260–273, 1999.

[87] D. J. O'Connor, D. Iacopino, D. A. Healy, D. O'Sullivan, and J. R. Sodeau, "The intrinsic fluorescence spectra of selected pollen and fungal spores," *Atmos Environ*, vol. 45, no. 35, pp. 6451–6458, 2011.

[88] F. Courvoisier, L. Bonacina, V. Boutou, L. Guyon, C. Bonnet, B. Thuillier, J. Extermann, M. Roth, H. Rabitz, and J. P. Wolf, "Identification of biological microparticles using ultrafast depletion spectroscopy," *Faraday Discuss*, vol. 137, pp. 37–49, 2008.

[89] V. Boutou, F. Courvoisier, L. Guyon, M. Roth, H. Rabitz, and J. P. Wolf, "Discriminating bacteria from other atmospheric particles using femtosecond molecular dynamics," *J Photoch Photobio A*, vol. 180, no. 3, pp. 300–306, 2006.

[90] A. Dogariu, A. Goltsov, D. Pestov, A. V. Sokolov, and M. O. Scully, "Real-time detection of bacterial spores using coherent anti-stokes raman spectroscopy," *J Appl Phys*, vol. 103, no. 3, 2008.

[91] W. W. Webb, W. R. Zipfel, R. M. Williams, R. Christie, A. Y. Nikitin, and B. T. Hyman, "Live tissue intrinsic emission microscopy using multiphoton-excited native fluorescence and second harmonic generation," *P Natl Acad Sci USA*, vol. 100, no. 12, pp. 7075–7080, 2003.

[92] S. C. Hill, B. V, J. Yu, S. Ramstein, J. P. Wolf, Y. L. Pan, S. Holler, and R. K. Chang, "Enhanced backward-directed multiphoton-excited fluorescence from dielectric microcavities," *Phys Rev Lett*, vol. 85, no. 1, pp. 54–57, 2000.

[93] C. Favre, V. Boutou, S. C. Hill, W. Zimmer, M. Krenz, H. Lambrecht, J. Yu, R. K. Chang, L. Woeste, and J. P. Wolf, "White-light nanosource with directional emission," *Phys Rev Lett*, vol. 89, no. 3, 2002.

[94] R. S. Judson and H. Rabitz, "Teaching lasers to control molecules," *Phys Rev Lett*, vol. 68, no. 10, pp. 1500–1503, 1992.

[95] J. L. Herek, W. Wohlleben, R. J. Cogdell, D. Zeidler, and M. Motzkus, "Quantum control of energy flow in light harvesting," *Nature*, vol. 417, no. 6888, pp. 533–535, 2002.

[96] V. I. Prokhorenko, A. M. Nagy, S. A. Waschuk, L. S. Brown, R. R. Birge, and R. J. D. Miller, "Coherent control of retinal isomerization in bacteriorhodopsin," *Science*, vol. 313, no. 5791, pp. 1257–1261, 2006.

[97] C. H. Tseng, S. Matsika, and T. C. Weinacht, "Two-dimensional ultrafast fourier transform spectroscopy in the deep ultraviolet," *Opt Express*, vol. 17, no. 21, pp. 18788–18793, 2009.

[98] P. Tournois, "Acousto-optic programmable dispersive filter for adaptive compensation of group delay time dispersion in laser systems," *Opt Commun*, vol. 140, no. 4-6, pp. 245–249, 1997.

[99] A. M. Weiner, "Femtosecond pulse shaping using spatial light modulators," *Rev. Sci. Instrum.*, vol. 71, no. 5, pp. 1929–1960, 2000.

[100] R. Selle, P. Nuernberger, F. Langhojer, F. Dimler, S. Fechner, G. Gerber, and T. Brixner, "Generation of polarization-shaped ultraviolet femtosecond pulses," *Opt Lett*, vol. 33, no. 8, pp. 803–805, 2008.

[101] M. Roth, M. Mehendale, A. Bartelt, and H. Rabitz, "Acousto-optical shaping of ultraviolet femtosecond pulses," *Appl Phys B-Lasers O*, vol. 80, no. 4-5, pp. 441–444, 2005.

[102] B. J. Pearson and T. C. Weinacht, "Shaped ultrafast laser pulses in the deep ultraviolet," *Opt Express*, vol. 15, no. 7, pp. 4385–4388, 2007.

[103] M. Hacker, G. Stobrawa, R. Sauerbrey, T. Buckup, M. Motzkus, M. Wildenhain, and A. Gehner, "Micromirror SLM for femtosecond pulse shaping in the ultraviolet," *Appl Phys B-Lasers O*, vol. 76, no. 6, pp. 711–714, 2003.

[104] T. Tanigawa, Y. Sakakibara, S. B. Fang, T. Sekikawa, and M. Yamashita, "Spatial light modulator of 648 pixels with liquid crystal transparent from ultraviolet to near-infrared and its chirp compensation application," *Opt Lett*, vol. 34, no. 11, pp. 1696–1698, 2009.

[105] T. Pfeifer, U. Weichmann, S. Zipfel, and G. Gerber, "Compression and shaping of a self-phase-modulated laser pulse with a deformable mirror device," *J Mod Optic*, vol. 50, no. 3-4, pp. 705–710, 2003.

[106] S. Bonora, D. Brida, P. Villoresi, and G. Cerullo, "Ultrabroadband pulse shaping with a push-pull deformable mirror," *Opt Express*, vol. 18, no. 22, pp. 23147–23152, 2010.

[107] Y. Ding, R. M. Brubaker, D. D. Nolte, M. R. Melloch, and A. M. Weiner, "Femtosecond pulse shaping by dynamic holograms in photorefractive multiple quantum wells," *Opt Lett*, vol. 22, no. 10, pp. 718–720, 1997.

[108] S. Coudreau, D. Kaplan, and P. Tournois, "Ultraviolet acousto-optic programmable dispersive filter laser pulse shaping in KDP," *Opt Lett*, vol. 31, no. 12, pp. 1899–1901, 2006.

[109] J. Diels and W. Rudolph, *Ultrashort Laser Pulse Phenomena*. 2006.

[110] S. Linden, J. Kuhl, and H. Giessen, "Amplitude and phase characterization of weak blue ultrashort pulses by downconversion," *Opt Lett*, vol. 24, no. 8, pp. 569–571, 1999.

[111] R. Trebino, K. W. DeLong, D. N. Fittinghoff, J. N. Sweetser, M. A. Krumbugel, B. A. Richman, and D. J. Kane, "Measuring ultrashort laser pulses in the time-frequency domain using frequency-resolved optical gating," *Rev. Sci. Instrum.*, vol. 68, no. 9, pp. 3277–3295, 1997.

[112] P. Antoine, A. LHuillier, and M. Lewenstein, "Attosecond pulse trains using high-order harmonics," *Phys Rev Lett*, vol. 77, no. 7, pp. 1234–1237, 1996.

[113] I. V. Schweigert and S. Mukamel, "Double-quantum-coherence attosecond x-ray spectroscopy of spatially separated, spectrally overlapping core-electron transitions," *Phys Rev A*, vol. 78, no. 5, 2008.

[114] R. Bartels, S. Backus, E. Zeek, L. Misoguti, G. Vdovin, I. P. Christov, M. M. Murnane, and H. C. Kapteyn, "Shaped-pulse optimization of coherent emission of high-harmonic soft X-rays," *Nature*, vol. 406, no. 6792, pp. 164–166, 2000.

[115] T. Pfeifer, R. Spitzenpfeil, D. Walter, C. Winterfeldt, F. Dimler, G. Gerber, and C. Spielmann, "Towards optimal control with shaped soft-X-ray light," *Opt Express*, vol. 15, no. 6, pp. 3409–3416, 2007.

[116] A. Willner, F. Tavella, M. Yeung, T. Dzelzainis, C. Kamperidis, M. Bakarezos, D. Adams, M. Schulz, R. Riedel, M. C. Hoffmann, W. Hu, J. Rossbach, M. Drescher, N. A. Papadogiannis, M. Tatarakis, B. Dromey, and M. Zepf, "Coherent control of high harmonic generation via dual-gas multijet arrays," *Phys Rev Lett*, vol. 107, no. 17, 2011.

[117] J. Lakowicz, *Principles of Fluorescence Spectroscopy*. 1999.

[118] M. Lewenstein, P. Balcou, M. Y. Ivanov, A. Lhuillier, and P. B. Corkum, "Theory of high-harmonic generation by low-frequency laser fields," *Phys Rev A*, vol. 49, no. 3, pp. 2117–2132, 1994.

[119] X. F. Li, A. Lhuillier, M. Ferray, L. A. Lompre, and G. Mainfray, "Multiple-harmonic generation in rare-gases at high laser intensity," *Phys Rev A*, vol. 39, no. 11, pp. 5751–5761, 1989.

[120] W. Kornelis, C. P. Hauri, A. Heinrich, E. W. Helbing, M. P. Anscombe, P. Schlup, J. W. G. Tisch, J. Biegert, and U. Keller, "Frequency-sheared, time-delayed extreme-ultraviolet pulses produced by high-harmonic generation in argon," *Opt Lett*, vol. 30, no. 13, pp. 1731–1733, 2005.

Part III

Annexes

Aerosols

5.1 Definitions

The aerosols can be defined as an ensemble of microparticles consisting of finely divided material and suspended in air or other gases [72]. They vary in size, composition, and in the way of interacting with surrounding medium. Considering the large variety of aerosol particles, it is useful to define the *equivalent diameter*. It refers to the diameter of a spherical particle with same specified physical propriety:

- *Volume equivalent diameter*;

- *Aerodynamic equivalent diameter*, refers to the same terminal velocity as a sphere of density 1000 kg/m^3;

- *Mobility equivalent diameter*, refers to a spherical particle with the same inertia and Brownian motion behaviour;

- *Mass equivalent diameter*;

- *Envelope equivalent diameter*, refers to the same surface;

- *Sauter equivalent diameter* refers to the same surface-to-volume ratio.

Two other parameters that characterize aerosol particles and are often used are the particle mass and number concentrations. The *particle number concentration* is calculated as the ratio between number of particles and the volume occupied, $1/m^3$. Similarly, the *particle mass concentration* is defined as the ratio between the particle mass and the volume occupied, kg/m^3. If the aerosol particles are monodisperse, which means they have almost the same volume equivalent diameter, one quantity is easily converted to the other. If aerosol particles are polydisperse that leads to a distribution of number concentration as function of particle size.

All airborne particles can be classified into the two distinct groups: *biological* and *non-biological*. The first group comprises large families of pollens, bacteria, spores, and viruses. The second group includes heavy dust particles (like cement particles or powder), ash, smoke, nanoparticles, smog, and soot. The particle size

ranges from few nanometers to hundreds of micrometers. Figure 5.44 reports distribution of the different kinds of particles presented in the atmosphere.
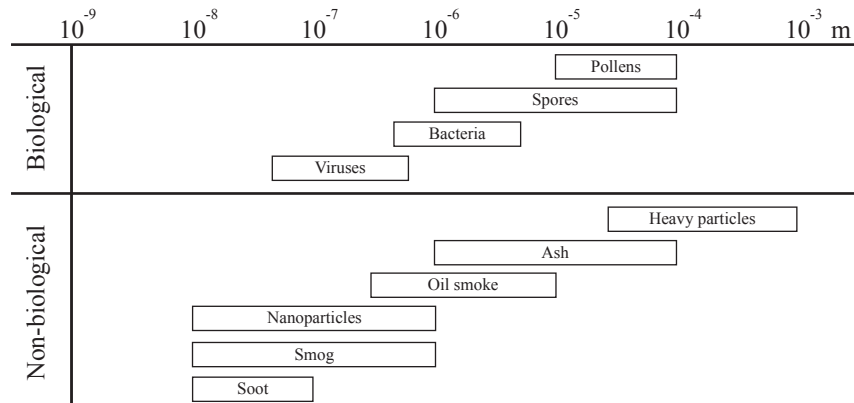
Figure 5.44: Size classification of aerosols

5.2 Pollen grains

This PhD work was mostly focused on airborne pollen detection. The pollen grains are defined as small grains produced by the plants and containing cells capable of producing male gametes. They are complex multicellular structures with a hard coat (sporoderm) protecting the fragile content. There are about 250'000 pollen species but only one out of ten is dispersed by the wind. Most of the pollen grains have close-to-spherical shapes, but they vary a lot in their surface structure. The pollen concentration changes depending on seasons and locations as it relies directly to the plant distribution and their reproduction periods. The pollen grains are well known allergens and affect more than 10 % of the European population. About 100 species are reported to be an important source of pollen allergies (pollinosis).

5.3 Particle motion in gases

This section introduces some basic aspects of aerosol dynamics in gases. The aerodynamic proprieties of airborne particle will serve as a starting point for the flow simulations that will be presented in Section 2.1.

5.3.1 Brownian motion

The Brownian motion is defined as a random motion of particles in a gas induced by collisions with the gas molecules [73] p.23. According to Einstein diffusion

equation, it can be described as following:

$$\frac{d\rho}{dt} = D\frac{d^2\rho}{dx^2}$$

(5.7)

where ρ is density of particles at point x at moment t, kg/m^3;
         D is mass diffusivity m^2/s.

A general solution of this equation can be written as:

$$\rho = \frac{1}{(4\pi Dt)^{\frac{1}{2}}} e^{\frac{x^2}{4Dt}}$$

(5.8)

The mean statistical displacement of a Brownian particle is derived from the solution of this equation and expressed as:

$$\overline{x}^2 = 2Dt$$

(5.9)

5.3.2   Gravitation

As every mass containing object, the aerosol particles experience the gravitational field force that tends to settle them. At the same time the faster they fall down, the larger is the dynamic friction force. For a given particle, the settling velocity is calculated as:

$$v = \frac{\rho g C d^2}{18\eta}$$

(5.10)

where ρ is particle density, kg/m^3;
         g is gravitational acceleration, m/s^{-2};
         η is air viscosity, kg/m s^{-1};
         d is particle diameter, m;
         C is Cunningham slip correction.

5.3.3   Thermal gradients

Another force that contributes to the particle motion in a gas is given by the thermal gradient of the medium:

$$v_T = \frac{0.55\eta}{\rho_g}\nabla T$$

(5.11)

where v_T is particle velocity due to thermal gradient, m/s;
         η gas viscosity, Pa $\cdot$ s;
         ρ_g gas density, kg/m^3;
         ∇T thermal gradient, K.

It can be seen from this expression that the particle velocity is independent on the particle size and should be taken into account for all aerosols.

5.3.4   Laminar and turbulent diffusion

If a particle is contained in a gas flow, it will experience a diffusion force due to the asymmetry of momentum transfer from the surrounding molecules. In *laminar* flow, it is admitted that the small particles (typical diameter less than 10 μm) have almost the same velocity as the flow of gas and follow well the streamlines. At the same time, due to higher inertia and in a presence of curved streamline, the larger particles will not be able to stay in the flow. For the case of curved pipes, these particles will impact and get stuck onto pipe walls:

$$v = \frac{\rho d^2 V^2}{18 \eta R} \tag{5.12}$$

where v is particle velocity in laminar flow, m/s;
ρ particle density, $\mathrm{kg/m}^3$;
d particle diameter, m;
V gas velocity, m/s;
η gas viscosity, $\mathrm{Pa \cdot s}$;
R pipe curvature, m.

For *turbulent* flow conditions, occurring when Reynolds number $R_e = \frac{\rho V D}{\eta} > 3 \cdot 10^3$ (D pipe diameter), it is difficult to derive a general analytical solution for the particle velocity [71]. It can, however, be evaluated empirically by the means of the Khan-Richardson force, expressed as:

$$F = \frac{\pi}{4} d^2 \rho \left(V - v\right)^2 \cdot \left(1.84 R_{ep}^{-0.31} + 0.293 R_{ep}^{0.06}\right)^{3.45}; \tag{5.13}$$

where m_p - particle mass, kg;
d - particle diameter, m;
V - gas velocity, m/s;
v - particle velocity, m/s;
$R_{ep} = \frac{\rho_g v d}{2\eta}$ - particle Reynolds number, unitless.

The expression below shows that this force tends to minimize the difference in velocity between the flow and particles in it. In particular, it demonstrates that particle velocity will be equal to the flow velocity in a straight and infinitely large pipe. In such a case, it is sufficient to calculate local flow velocity, which will give a good estimation of the particle velocity in the same point.

As a consequence, this expression is very useful to calculate particle trajectories in a gas flow once the flow velocity is known at every point. This method is used by Comsol software for the case of particles with given mass.

Chapter 6

Light scattering

The light scattering is one the main physical effects that will be employed in this PhD work to discriminate different airborne particles. Some concepts introduced here will be used in the simulations in Section 2.4.

The light scattering is a complex interaction between incident electromagnetic (EM) waves and objects comparable in size with wavelength [79]. More precisely, this interaction happens on the electronic clouds that start to oscillate in the external EM field and emit radiation in directions different from the indecent waves (Fig. 6.1). In the case of the spherical particles, there are three different approaches to study the scattering effect depending of the particle size:

- particle diameter $D \gg \lambda_{inc}$ - geometrical reflection/refraction;

- particle diameter $D \simeq \lambda_{inc}$ - Mie theory;

- particle diameter $D \ll \lambda_{inc}$ - Rayleigh theory.
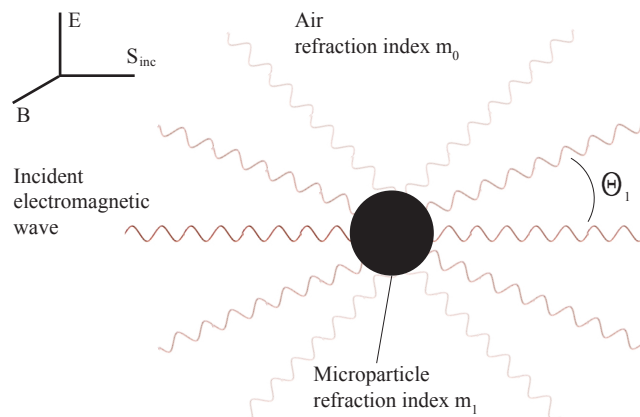
Figure 6.1: Schematic representation of the light scattering

6.1   Geometrical reflection/refraction ($D \gg \lambda_{inc}$)

This is a case where the incident light is partially reflected and refracted from medium interfaces (m_1/m_0 with $m = n - ik$ where n - real part of refractive index; k - imaginary part of refractive index) in many directions. Some part of the energy is also absorbed and dispersed in a non-radiative way inside the particle. Due to symmetry (in the case of the spherical shape), the scattering and absorption from the particles is uniform for the same Θ, which is not more the case for non-spherical particles. The scattering pattern (angular dependence of scattered light intensity) becomes much more complicated, but at the same time it can provide an additional information on the particle shape. In general, finding the corresponding scattering pattern for each geometrical shape is a complex ray tracing problem. For this reason, the common approach is to measure the pattern for some particles with well defined shapes and to investigate the similarities and differences among the collected data[84, 76].

6.2   Mie theory ($D \simeq \lambda_{inc}$)

For particles with sizes comparable or smaller than the wavelength, the total cross section (called also extinction cross section) describes the efficiency that gives amount of incident energy lost on scattering and absorption:

$$F_{ext} = I_{inc}\frac{d\sigma_{ext}}{d\Omega}d\Omega \tag{6.1}$$

where $d\Omega = sin(\Theta)d\Theta d\phi$ is the solid angle, sr;
$\quad\quad\quad$ F_{ext} is the extinction of the radiant flux through the solid angle $d\Omega$, W;
$\quad\quad\quad$ I_{inc} is incident intensity, W/m^2;
$\quad\quad\quad$ σ_{ext} is the total extinction cross section, m^2.

The total extinction cross section is expressed by:

$$\sigma_{ext} = \sigma_{abs} + \sigma_{scat} \tag{6.2}$$

where σ_{abs} is the total absorption cross section, m^2;
$\quad\quad\quad$ σ_{scat} is the total scattering cross section, m^2.

In Mie theory, the differential scattering cross sections for the vertical and horizontal polarisations are defined by the following expressions (case of the spherical particles):

$$\frac{d\sigma_V}{d\Theta} = \frac{\lambda^2}{4\pi^2}S_1(\Theta) \tag{6.3}$$

$$\frac{d\sigma_H}{d\Theta} = \frac{\lambda^2}{4\pi^2}S_2(\Theta) \tag{6.4}$$

where $S_1(\Theta), S_2(\Theta)$ are the angular scattering amplitudes, n.a.

The functions $S_1(\Theta), S_2(\Theta)$ are derived as following:

$$S_1(\Theta) = |\sum_{n=1}^{\infty} \frac{2n+1}{n(n+1)}(a_n\pi_n(cos(\Theta)) + b_n\tau_n(cos(\Theta)))|^2 \qquad (6.5)$$

$$S_2(\Theta) = |\sum_{n=1}^{\infty} \frac{2n+1}{n(n+1)}(a_n\tau_n(cos(\Theta)) + b_n\pi_n(cos(\Theta)))|^2 \qquad (6.6)$$

where a_n, b_n are the parameters defined with Ricatti-Bessel functions, n.a;

π_n, τ_n are the functions expressed in terms of Legendre polynomials, n.a.

The total extinction and scattering cross sections can be then derived as follows [79]:

$$\sigma_{scat} = \frac{\lambda^2}{2\pi} \sum_{n=1}^{\infty} (2n+1)(|a_n|^2 + |b_n|^2) \qquad (6.7)$$

$$\sigma_{ext} = \frac{\lambda^2}{2\pi} \sum_{n=1}^{\infty} (2n+1)Re\{a_n + b_n\} \qquad (6.8)$$

6.3 Rayleigh theory ($D \ll \lambda_{inc}$)

Rayleigh approximation permits to define the differential scattering cross sections for the vertical and horizontal polarizations in a shorter way:

$$\frac{d\sigma_V}{d\Theta} = \frac{\lambda^2\alpha^6}{4\pi^2} \left|\frac{m^2-1}{m^2+1}\right|^2 \qquad (6.9)$$

$$\frac{d\sigma_H}{d\Theta} = cos^2(\Theta)\frac{d\sigma_V}{d\Theta} \qquad (6.10)$$

where λ is the wavelength, m;

α is the size parameter $\alpha = \frac{2\pi D}{\lambda}$ with D - diameter of the particle and λ wavelength.

For the total absorption cross section, the expression is following :

$$\sigma_{abs} = -\frac{\lambda^2\alpha^3}{\pi}Im\left\{\frac{m^2-1}{m^2+1}\right\} \qquad (6.11)$$

Finally, for unpolarized light the extinction cross section can be written as :

$$\sigma_{scat} = \frac{2\lambda^2\alpha^6}{3\pi} \left|\frac{m^2-1}{m^2+1}\right|^2 \qquad (6.12)$$

Chapter 7

Single and multi-photon excited fluorescence

Fluorescence is one of the possible pathways of depopulation of electronic excited states[117]. In general, it occurs upon absorption of a photon with frequency within the absorption band of the molecule. According to Born − Oppenheimer approximation, an electronic transition between excited states or ground and excited states can be seen as an instantaneous process compared with nuclear and molecular motions.

Light induced fluorescence refers to the radiative de-excitation scheme presented in Figure 7.1. The horizontal lines inside each electronic potential indicate molecular vibrational levels. After instantaneous electronic transition (vertical arrow), the molecule is out of equilibrium on the electronic excited state curve, and a non-radiative relaxation will follow (IVR). Fluorescence transition can then occur, bringing the molecule to the ground state.

The energy absorbed by the molecule is always larger than that transformed into the fluorescence photon. The absorption-emission energy difference is called a Stokes shift and plays an important role in the spectroscopy. In fact, it allows to easily distinguish the fluorescence signal from the excitation light by an appropriate filtering.

The fluorescence efficiency is generally quantified by the following formula:

$$N_F = N_A \cdot \Phi_F \tag{7.1}$$

where N_F is number of emitted fluorescence photons, n.a.;

             N_A is number of absorbed photons, n.a.;

             Φ_F is quantum yield of fluorescence, %.
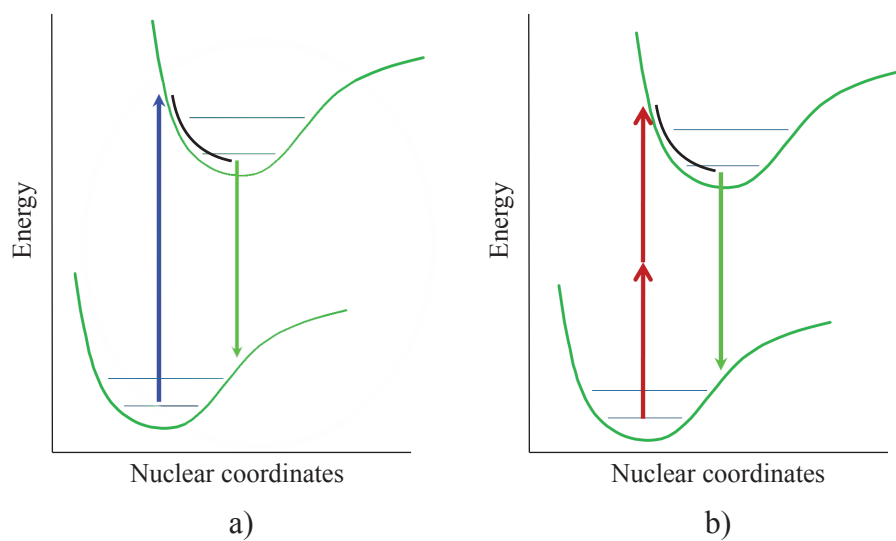
Figure 7.1: a) Linear, one-photon fluorescence; b) non-linear, two-
photon fluorescence

It expresses the efficiency of radiative (fluorescence) relaxation of ensemble of
fluorophore molecules in comparison with non-radiative paths. The quantum yield
depends on the fluorophore nature.

Chapter 8

Chirped pulse amplifier

A chirped pulse amplifier (Fig. 8.1) is a laser system based on the amplification of temporally stretched pulses with large spectrum and contains always three main stages: stretcher, regen cavity, compressor. A femtosecond pulse from an oscillator (80 MHz) enters the grating stretcher block where its spectral components are temporally dispersed. As result, after recombination of the components, the whole pulse becomes about 10^4 times longer than its initial duration.
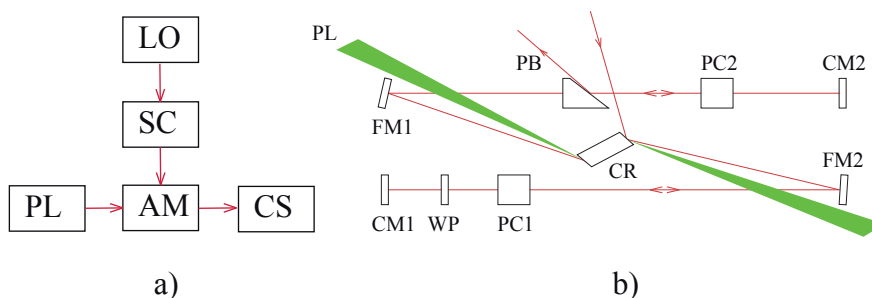
Figure 8.1: a) Chirped pulse amplifier scheme; b) Amplifier cavity: PL - pump laser beam (green); FM1, FM2 - folding mirrors; CM1, CM2 - cavity mirrors; PC1, PC2 - Pockels cells; WP - $\lambda/4$ wave plate; PB - polarizing beam splitter; CR - crystal rod

The injection of a single stretched pulse into the cavity is done by combination of polarization sensitive components: total reflection on crystal rod (CR), double pass in $\lambda/4$ wave plate (WP) and polarizing beam splitter (PB). The retention is controlled by activation of the first Pockels cell (PC1) that rotate polarization to -45°. When the cell is switched off, an incoming pulse obtains in total 90°polarization, makes single trip in the cavity and leaves it. If the Pockels cell (PC1) is synchronized with the seeding oscillator and it is activated right before arrival of a next stretched pulse, then the pulse receives total polarization of 0° (PC1 contracts the

effect of WP). On each pass, the pulse intensity increases by factor 3-4. After around 20 passes the gain becomes saturated and the pulse needs to be extracted. This is done by combination of a polarization beam splitter (PB) and the second Pockels cell (PC2). The switching on of this cell induces in total $90°$ polarization rotation. So the amplified pulse is completely reflected by the beam splitter. During the amplification process, the pulses from the oscillator cannot enter the regen cavity. In general (depending on the pump laser repetition rate) the output of an amplifier is in the $1 - 300$ kHz.

The last stage of amplifier creates the opposite optical path for spectral components than the stretcher block. The resulting pulse is compressed to femtosecond duration, limited by the Fourier transform of its spectral bandwidth. The output peak power can reach 10^3 times the initial value.

Chapter 9

High harmonics generation

The high harmonic generation (HHG) is a result of non-linear light-matter interaction in which an external pulsed electric field is strong enough to make highly oscillate atomic electrons [109]. In particular, the external field (Fig.9.1) should be comparable or higher than the electric field of nucleus seen by electrons. In this case, the resulting Coulomb potential is modified and an electron can cross the barrier by the quantum tunnelling or directly. If the external EM field oscillates fast enough, $10^{14} - 10^{15}$ Hz (corresponds to IR and VIS light), the freed electron can then be brought back to its ion and recombine. The excessive amount of energy is emitted afterwards with a short-wavelength photon:

$$h\nu = U_0 + \frac{e^2 \langle E^2 \rangle}{4m\omega_l^2} \tag{9.1}$$

where U_0 - ionization potential energy, J;
         e - electron charge, C;
         E - laser electric field, V/m;
         m - electron mass, kg;
         w_l - oscillation frequency of the laser electric field, rad/s.

To obtain an efficient HHG, one needs a pulsed and intense laser source capable of delivering more than 10^{15} W/cm^2 of light intensity [118, 112]. This can be achieved by the focusing ultra-short femtosecond laser pulses with a pulse duration less than 50 fs and energies more than few µJ per pulse. A classical HHG scheme [119, 120] is presented in Figure 9.2. An IR femtosecond laser is focused on a molecular jet of noble gas inside a vacuum chamber resulting in a collinear with the pump laser XUV beam.
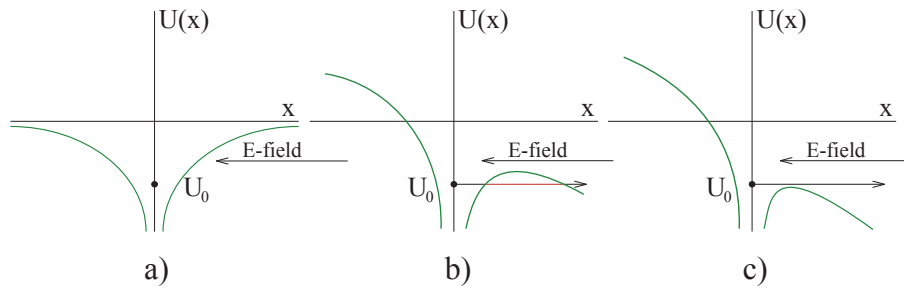
Figure 9.1: Three regimes of light-atom interaction: a) weak external electric field $E << 10^{11}$ V/m; b) moderate external electric field $E \simeq 10^{11}$ V/m; c) strong external electric field $E >> 10^{11}$ V/m.
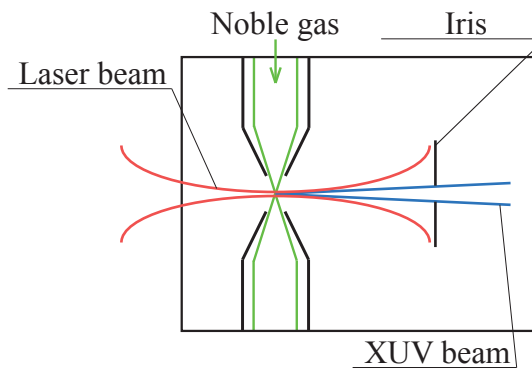
Figure 9.2: HHG scheme.

Curriculum vitae

Denis Kiselev

PERSONAL INFORMATION	*Address* : Rue de la Colline 3 1205 Geneva Switzerland *Date of birth* : 21.04.1982 *Citizenship* : Russian *Status* : single

Mobile: +41.78.641.25.61
Tel.: +41.22.379.48.05
E-mail: Denis.Kiselev@unige.ch
Place of birth : Klimovsk, Russia
Swiss permit B, student

OBJECTIVE

Enlarge spheres of professional and personal interests; develop new skills; collaborate and work together with advanced researchers; be on the leading edge of science and technology to create new devices, technologies and methods focusing on real-time air quality monitoring

RESEARCH INTERESTS

Aerosol science, optical detectors, linear and multi-photon spectroscopy, ultrafast laser pulse shaping, microscopy, laser machining, fast digital electronics, field programmable gate arrays, soft processing, embedded control systems

LANGUAGES

Russian - native;
English, French, Spanish - fluent.
French Language Diploma, Alliance Française, 2005

AWARDS

Venture 2012 finalist,
Start-up : "PLAIR Solutions",
Project : "Pollen Tracker - real-time pollen detector"

EDUCATION

University of Geneva, Switzerland

Ph.D., Applied Physics   **June 2012**

- Thesis Topic: *All-optical methods and devices for real-time aerosol detection*
- Thesis Proposal: *Development of new methods and instruments for real-time aerosol detection, linear and non-linear single aerosol particle spectroscopy, temporal pulse shaping, XUV amplitude shaping of high harmonics, filament induced laser machining, ultrafast laser micro-machining*
- Adviser: Professor Jean-Pierre Wolf
- Area of Study: Optical instrumentation, non-linear spectroscopy, ultrafast laser spectroscopy
- Collaborations:
  MEMS mirror arrays for pulse shaping - **Prof. N. de Rooij** (IMT, **EPF Lausanne**);
  XUV amplitude shaping - **Prof. H.J. Woerner** (**ETH Zurich**);
  Filament induced laser machining - **Prof. L. Woeste** (**University**

of Berlin);
Laser micro-machining - **Mr. R. Bossard** (**Rolex SA**)

M.S., Applied Physics   **September 2007**
- Diploma Topic: *Development of a pulse shaper based on micro-mirror array*
- Adviser: Professor Jean-Pierre Wolf
- Area of Study: Optical instrumentation for fundamental research

B.S., Physics   **June 2006**

Moscow State University "Stankin", Russian Federation

M.S., Methods and instruments of measurement   **June 2004**
- Diploma Topic: *Development of the measurement system of mass flow in the central evacuation pipe of water-water nuclear reactor (WWNR-1000)*
- Adviser: Professor Nikolai N. Markov
- Area of Study: Measurement equipment for test and launching phase of water-water nuclear reactor (WWNR-1000)

B.S., Automatic control   **June 2003**
- Diploma Topic: *Development measurement system of angular speed of central water pump of water-water nuclear reactor (WWNR-1000)*
- Adviser: Professor Nikolai N. Markov
- Area of Study: Measurement equipment for test and launching phase of water-water nuclear reactor (WWNR-1000)

SUBMITTED
JOURNAL
PUBLICATIONS

Kiselev, **D.**, L. Bonacina, J.P. Wolf (2011). "Individual bioaerosol particle discrimination by multi-photon excited fluorescence." Optics Express 19(24): 24516-24521.

Wolf, J. P., A. Rondi, **D. Kiselev**, S. Machado, J. Extermann, S. Weber, L. Bonacina, J. Roslund, M. Roth and H. Rabitz (2011). "Discriminating Biomolecules with Coherent Control Strategies." Chimia 65(5): 346-349.

Weber, S. M., L. Bonacina, W. Noell, **D. Kiselev**, J. Extermann, F. Jutzi, S. Lani, O. Nenadl, J. P. Wolf and N. F. de Rooij (2011). "Design, simulation, fabrication, packaging, and characterization of a MEMS-based mirror array for femtosecond pulse-shaping in phase and amplitude." Review of Scientific Instruments 82(7).

Extermann, J., S. M. Weber, **D. Kiselev**, L. Bonacina, S. Lani, F. Jutzi, W. Noell, N. F. de Rooij and J. P. Wolf (2011). "Spectral phase, amplitude, and spatial modulation from ultraviolet to infrared with a reflective MEMS pulse shaper." Optics Express 19(8): 7580-7586.

Weber, S. M., J. Extermann, L. Bonacina, W. Noell, **D. Kiselev**, S. Waldis, N. F. de Rooij and J. P. Wolf (2010). "Ultraviolet and near-infrared femtosecond temporal pulse shaping with a new high-aspect-ratio one-dimensional micromirror array." Optics Letters 35(18): 3102-3104.

Kiselev, **D.**, L. Woeste and J. P. Wolf (2010). "Filament-induced laser machining (FILM)." Applied Physics B - Lasers and Optics 100(3): 515-520.

Henin, S., Y. Petit, **D. Kiselev**, J. Kasparian and J. P. Wolf (2009). "Contribution of water droplets to charge release by laser filaments in air." Applied Physics Letters 95(9).

Extermann, J., L. Bonacina, F. Courvoisier, **D. Kiselev**, Y. Mugnier, R. Le Dantec, C. Galez and J. P. Wolf (2008). "Nano-FROG: Frequency resolved optical gating by a nanometric object." Optics Express 16(14): 10405-10411.

CONFERENCE PUBLICATIONS

Noell, W., S. Weber, J. Masson, J. Extermann, L. Bonacina, A. Bich, R. Bitterli, H. P. Herzig, **D. Kiselev**, T. Scharf, R. Voelkel, K. J. Weible, J. P. Wolf and N. F. de Rooij (2011). "Shaping Light with MOEMS." Moems and Miniaturized Systems X 7930.

Weber, S. M., W. Noell, S. Lani, F. Jutzi, P. Bruhlmeier, **D. Kiselev**, J. Extermann, L. Bonacina, J. P. Wolf and N. F. de Rooij (2010). "High aspect ratio micromirror array with two degrees of freedom for femtosecond pulse shaping." Moems and Miniaturized Systems Ix 7594.

Weber, S. M., S. Waldis, W. Noell, **D. Kiselev**, J. Extermann, L. Bonacina, J. P. Wolf and N. F. de Rooij (2009). "Linear micromirror array for broadband femtosecond pulse shaping in phase and amplitude." Moems and Miniaturized Systems Viii 7208.

Waldis, S., S. M. Webert, W. Noell, J. Extermann, **D. Kiselev**, L. Bonacina, J. P. Wolf and N. F. de Rooij (2008). "Large linear micromirror array for UV femtosecond laser pulse shaping." 2008 Ieee/Leos International Conference on Optical Mems and Nanophotonics: 39-40.

CONFERENCES AND PhD SCHOOLS

- *Poster presentation* at the Nano and Photonics 2011, Mauterndorf, Austria.

- *Oral and poster presentation* at the Femtomat 2011, Mauterndorf, Austria.

- *Poster presentation* at the Colloque franco-allemand "50 ans a la lumiere du laser", 2011, Berlin, Germany

- *Poster presentation* at the Cofil 2010, Crete, Greece

- *Oral and poster presentation* at the Workshop + WG joint meeting, 2009, Bucharest, Romania

- *Oral and poster presentation* at the Bio-innovation Day 2009, Geneva, Switzerland

- *Summer school*, COST P21, 2008, Capri, Italy

- *Winter school*, Climate Science, 2008, Champex, Switzerland

TEACHING
EXPERIENCE

University of Geneva, Switzerland

- *Teaching Assistant*   **November 2007 to now**

    - Preparing exercises of "General Physics B" for students in Biology and Pharmacy;
    - Giving seminars of "General Physics B" for students in Biology and Pharmacy;
    - Preparing and revising exams of "General Physics B" for students in Biology and Pharmacy;

- *Teaching Assistant*   **November 2010**
  Design and development of LIDAR demonstration system for exhibition "Nuit des Sciences 2010".

- *Teaching Assistant*   **November 2008**
  Design and development of optical tweezers for exhibition "Palais de la Découverte 2008. Prise au Piège".

PROFESSIONAL
EXPERIENCE

- *Technician*   **November 2002 - June 2004**
  Experimental and design organisation OKB "GIDROPRESS", Podolsk, Russia

INFORMATICS
SKILLS

- *Software*
  Adobe Illustrator, Adobe Photoshop, Adobe Premier, Adobe Acrobat, Adobe Flash, Matlab, 3ds Max, Comsol Multiphysics, Altium Designer, OrCAD, AutoCAD, Tina-TI, Inventor, SolidWorks, Code V, LabWindows CVI, Microsoft Office, LaTex, Xilinx ISE, SmartDraw, XMOS

- *Hardware*
  Analogue to digital converters, field programmable gate arrays, audio amplifiers, optical detectors, digital signal processing

HOBBIES   Tennis, mountain ski, table tennis, Latin dances